

ABSTRACT

Title of Document: PERFORMANCE OF A
MICROCHANNEL-THERMOELECTRIC
POWER GENERATOR WITH ALUMINA-
IN-WATER NANOFLUIDS AS
COOLANTS

Herwin Singh Ahuja, Master of Science
2010

Directed By: Professor Bao Yang, Mechanical
Engineering

In the past two decades, the rapid advancement of military aircraft in terms of performance and power consumption in order to accomplish evermore demanding missions has introduced new challenges, namely, having to conserve of non-renewable petroleum, minimize carbon emissions, and accomplish more mission per unit energy. This thesis describes the work done to evaluate the performance of a renewable-energy device termed the microchannel-thermoelectric power generator (MC-TEPG), which uses alumina-in-water nanofluids as coolants, that is intended to replace or supplement current non-renewable power supplies such as battery packs in order to contribute to overcoming the abovementioned challenges. The MC-TEPG recovers waste heat internally generated by motors of military aircraft and converts it to usable electric power via the Seebeck effect. This thesis studies nanofluid flow and heat transfer in the MC-TEPG microchannels, and thermoelectric power generation under varying conditions. Current results show MC-TEPG feasibility and suggest future promise.

PERFORMANCE OF A MICROCHANNEL-THERMOELECTRIC POWER
GENERATOR WITH ALUMINA-IN-WATER NANOFLUIDS AS COOLANTS

By

Herwin Singh Ahuja

Thesis submitted to the Faculty of the Graduate School of the
University of Maryland, College Park, in partial fulfillment
of the requirements for the degree of
Master of Science
2010

Advisory Committee:
Professor Bao Yang, Chair
Professor Tien-Mo Shih
Professor Santiago Solares

Dedication

This work is dedicated to my mother and father, Harinder and Devinder Ahuja, and to my exalted friends, Sai Baba of Shirdi, Jaihind Bahadur Singh, Sushil Mehta and Surinder Luthra. Thanks to all of my loved ones who have supported and encouraged me to complete this endeavor.

Acknowledgements

I would like to thank my advisor Dr. Bao Yang and my NSWC mentor Dr. Thanh Tran for all of their help in conducting this research. I am confident that all I have learned from them will benefit me throughout my professional career. My thanks is also extended to Mr. Scott Hoover, Mr. Warren Baker and Mr. Eric Satchel for their guidance and technical expertise, and to the National Surface Warfare Center (NSWC)-Carderock Division for the financial support that made this research possible.

Table of Contents

Dedication	ii
Acknowledgements	iii
Table of Contents	iv
List of Tables	v
List of Figures	vi
Nomenclature	viii
Chapter 1: Introduction	1
1.1: U.S. Navy/Military Renewable Energy Technology Needs	1
1.2: Project Motivation and Objectives	6
Chapter 2: Literature Review	11
2.1: Thermoelectric Technology Research	12
2.2: Nanofluids Research	20
2.3: Microchannel Research	27
2.3.1: Microchannel Studies—Conventional Base Fluid Coolants Only	28
2.3.2: Microchannel Studies—Nanofluid and Conventional Coolants	43
Chapter 3: Experimental Apparatus and Procedure	49
3.1: Design and Construction of the Microchannel Heat Exchanger	50
3.1.1: Microchannel Material Selection	50
3.1.2: Microchannel Surface Design	53
3.1.3: Microchannel Dimensions	55
3.2: Design and Construction of the Microchannel Test Section	60
3.3: Design and Construction of the Microchannel Test Rig	70
3.4: Experimental Procedure	78
3.5: Simulation Procedure	82
Chapter 4: Results and Analysis	87
4.1: Pressure Drop Results and Analysis	88
4.2: Brinkman Number-Based Analysis	101
4.2.1: Flow Regime Verification	102
4.2.2: Viscous Heating Assessment	105
4.3: Microchannel Heat Transfer Results and Analysis	108
4.3.1: Nusselt Number vs. Heat Flux	109
4.3.2: Nusselt Number vs. Reynolds Number	114
4.3.3: Heat Transfer Coefficient Analysis	120
4.4: Thermoelectric Power Generation Analysis	127
4.5: Simulation Results and Analysis	137
Chapter 5: Conclusions and Future Work	145
5.1: Conclusions	145
5.2: Recommendations for Future Work	155
5.3: Professional Contributions Made by the Author	159
References	161

List of Tables

Table 1: CHP Efficiency ratings rendered in each mode of TEPG integration.....	16
Table 2: Experimentally obtained coolant properties at 12 °C.....	79
Table 3: Experimental Water, NF1 and NF2 Re_D values at the 6 flow rates...	88
Table 4: Coolant shear rates and slip lengths at the 6 flow rates.....	91
Table 5: HF_C and $HF_{S/R}$ values for Water, NF1 and NF2 at the 6 flow rates...	114
Table 6: Re_C and $Re_{S/R}$ values for Water, NF1 and NF2 at the 9 heat fluxes..	119

List of Figures

Figure 1: Illustration of the Seebeck effect. Adopted from [7].....	13
Figure 2: Illustration of the Peltier effect. Adopted from [7].....	14
Figure 3: (a) Thermal conductivity enhancement and (b) Viscosity vs. volume fraction of alumina in water. Adopted from [13].....	22
Figure 4: (a) Friction factor and (b) Heat transfer predictions in the laminar flow regime. Adopted from [21].....	29
Figure 5: Scaling effects on mean Nusselt number for (left) water and (right) iso-propanol. Adopted from [27].....	37
Figure 6: Engineering drawing of the microchannel heat exchanger. All dimensions are in millimeters.....	55
Figure 7: Stepwise assembly of the microchannel heat exchanger.....	59
Figure 8: (a) The exploded and (b) unexploded views of Moores et al.'s test section. Adopted from [39].....	61
Figure 9: Microchannel Test Section at different stages of its assembly...	62
Figure 10: Engineering drawings of the header. All dimensions are in millimeters.....	65
Figure 11: Engineering drawings of the gasket. All dimensions are in millimeters.....	65
Figure 12: (a) 2 side-by-side TEC1-12708 modules and (b) engineering drawings of the TEC1-12708. All dimensions are in millimeters.	67
Figure 13: (a) The HM6800R4.5L36T1 heater and (b) corresponding engineering drawings. All dimensions are in millimeters.....	68
Figure 14: Schematic of the entire test rig with both the primary and secondary flow loops.....	71
Figure 15: Test rig schematic—primary/single loop part only.....	72
Figure 16: Photographs of the Microchannel Test Rig.....	74
Figure 17: Simulated portion of the test section with all (a) parts labeled and (b) thermal boundary conditions labeled.....	83
Figure 18: Engineering drawings of the simulated portion of the test section. All dimensions are in millimeters.....	83
Figure 19: Experimental pressure drop vs. flow rate.....	89
Figure 20: Excess pumping power vs. flow rate.....	89
Figure 21: Experimental friction factors vs. Reynolds number.....	93
Figure 22: Experimental friction factors of (a) water, (b) NF1 and (c) NF2, compared with those predicted by microchannel correlations [21, 22].....	95
Figure 23: Experimental friction factors of (a) water, (b) NF1 and (c) NF2, compared with those predicted by conventional correlations [30, 44].....	98
Figure 24: Experimental Br-Br _r values of (a) water, (b) NF1 and (c) NF2.	103
Figure 25: Viscous heating significance in all (a) water, (b) NF1 and (c) NF2 test runs.....	106
Figure 26: Experimental and Hausen Nusselt numbers against applied heat flux at all 6 relevant flow rates.....	110

Figure 27: Experimental and Hausen Nusselt numbers against Reynolds numbers at all 9 relevant applied heat flux values.....	115
Figure 28: Experimental heat transfer coefficients against applied heat flux at all 6 relevant flow rates.....	121
Figure 29: Heat transfer coefficients against heat flux (left column) and Reynolds number (right column).....	124
Figure 30: Total thermoelectric power generation against applied heat flux—coolant curve comparison.....	129
Figure 31: Total thermoelectric power generation against applied heat flux—flow rate curve comparison.....	131
Figure 32: Net power output against applied heat flux—coolant curve comparison.....	132
Figure 33: Net power output against applied heat flux—flow rate curve comparison.....	135
Figure 34: Difference between experimental and simulation microchannel temperatures against applied heat flux—coolant curve comparison.	138
Figure 35: Difference between experimental and simulation microchannel temperatures against applied heat flux—flow rate curve comparison.	140
Figure 36: Microchannel surface temperature variation from 4 simulation runs. All temperatures shown at the top right of each image are in °C.....	142

Nomenclature

A	area, [m ²]
Br	Brinkman number, [-]
c _p	specific heat, [J/kg-K]
D (or d)	diameter [m]
f	Darcy friction factor, [-]
Gz	Graetz number, [-]
h	heat transfer coefficient, [W/m ² -K]
HF	applied heat flux, [W/cm ²]
I	electric current, [A]
k	Thermal conductivity, [W/m-K]
L	length, [m]
m [?]	Mass flow rate, [LPM]
Nu	Nusselt number, [-]
p	pressure, [Pa]
P	power, [W]
Po	Poiseuille number, [-]
Pr	Prandtl number, [-]
Q	heat current, [W]
R	Electric resistance
Re	Reynolds number, [-]
T	temperature, [°C]
v	velocity, [m/s]
V	voltage, [V]
ZT	Thermoelectric Figure of Merit [-]

Greek Symbols

α	Seebeck coefficient, [V/K]
β	slip length, [m]
η	efficiency, [%]
μ	dynamic viscosity, [Pa-s]
Π	Peltier coefficient, [V]
ρ	Density, [kg/m ³]
τ	Thomson coefficient, [V/K]

Subscripts

bulk	bulk
C	conjugate heat transfer/cold
D	diameter
el	electric
h	hydraulic
H	hot

in	inlet
L	load
max	maximum
out	outlet
p	pressure
R	surface roughness
S	slip
surf.	surface
TE	thermoelectric
TEPG	thermoelectric power generator
th	thermal
tr	transitional

Chapter 1: Introduction

1.1: U.S. Navy/Military Renewable Energy Technology Needs

The development of electrical power generation technology during the Industrial Revolution has since been propelling mankind to the utmost heights of socioeconomic progress. To date, the major advancements in this field have resulted, not only, in the global establishment of high-capacity electrical power generation plants, but also in the creation of portable, compact, high-energy-storage/delivery devices such as batteries. However, such advanced technologies have drawbacks that are becoming increasingly consequential and call for immediate attention from the engineering community. A particular concern, of this paper, is that almost all machines whose function depends partly on some type of battery and/or engine (i.e. automobiles, tanks, navy aircraft, no-man surveillance drones) additionally require consumption of fuel, typically petroleum/fossil fuels, in order to generate enough power to maintain and carry out their function. Today, over 90% of all global power is being generating via combustion of petroleum, which cannot be taken for granted in the long term. In fact, recent studies performed by British Petroleum estimate that, at the current rate of consumption, only about 150 years worth of ‘useful’ (energy efficient) petroleum remains in the world [1]. Furthermore, scientist Gregson Vaux has predicted that coal (the most commonly used fossil fuel) production in the United States would inevitably decline as early as 2032, thus making it evermore prudent to explore and develop alternate, *preferably renewable*, energy solutions [1]. A

generally applicable renewable energy technology could help to minimize excess petroleum and battery power consumption if properly incorporated into commonly used machines. Such technology would be a sizeable step towards securing the nation's future military and non-military power generation needs. While it is important that U.S. commercial and industrial sectors would be allowed to maintain their rate of progress, the navy/military sector would gain far more from renewable energy technology. Specifically, many lives of the men and women of the armed forces could potentially be saved and missions could be completed with minimized expenditure of petroleum—ultimately helping to secure not only the nation's energy future but also the safety of the American people. Since the military sector stands to gain the most from feasible renewable energy technology, it would be reasonable that the United States defense agencies lead the world in the research and development (R&D) of such technologies.

In recent years, U.S. government agencies, such as the Department of Energy (DOE) and various army/navy research labs, have indeed become aware of the imminent need for renewable energy and energy efficiency enhancement. In accordance with the American Recovery and Reinvestment Act of 2009, the DOE budget pertaining to energy efficiency and renewable energy (EERE) R&D has seen a tremendous rise [2]. This record-setting budget spike has led the DOE to loan a total of \$124 billion to several private companies of the commercial sector for EERE research [2]. As per the research of National Laboratories Technologies Fellow R. J. Umstatt, it seems that the Recovery Act is a godsend for the U.S.

military sector, especially for the Department of Defense (DOD) [3]. The DOD is likely to benefit the most from Recovery Act-induced EERE progress as it has been the most energy consuming U.S. government agency, accounting for 80% of the total energy used by the government in Fiscal Year 2006 (FY06) [3].

Furthermore, U.S. government agencies face a growing environmental dilemma in the form of increased hazardous carbon emissions and concentration in the atmosphere [1, 2]. Namely, since the dawning of the Industrial Revolution, the atmospheric carbon dioxide concentration has risen from 280 parts per million to 350 parts per million primarily due to the combustion of petroleum for the sake of power generation [1]. At this alarming rate of emission, carbon concentration in the global atmosphere is estimated to double by 2050, raising the global temperature by 6 degrees Fahrenheit, thus worsening the threat of global warming [1]. On the other hand, due to raised awareness of lawmakers regarding looming pollution hazards and the international pressure on the U.S., President Obama has established a firm goal of reducing the national rate of carbon emissions by 80% by the year 2050 [2]. Although, the DOD is the main U.S. government energy user, historically, it has only been able to dedicate very small percentages (2.5% in FY07) of its overall budget towards EERE R&D, therefore, outside collaboration is essential if the ambitious standards of President Obama's carbon emission goal are to be met [3].

Now that the EERE problems of the U.S. military sector have been sufficiently addressed, potential solutions and their payoffs/tradeoffs will be touched upon.

Considering the magnitude and large national-scale of the entire problem at hand, R. J. Umstatted has proposed, for the sake of manageability, the following three classifications of navy/military energy solutions: (1) develop and implement new principal energy sources that are not reliant on petroleum and are '*preferably renewable*,' (2) practice conservation to reduce consumption, and (3) enhance energy use efficiency as to accomplish more mission per unit of energy input [3].

Recently, the DOD has seen some success in being able to military aircraft, such as B-52s and C-17s, on a half-and-half blend of JP-8 and petroleum based fuel—making this a significant new solution of the first kind [3]. This solution is indeed advancement but not a breakthrough as it is still highly dependent on petroleum, and thus, is only good for buying more time until a more permanent solution is derived. As far as energy conservation goes, DOD employees have always been encouraged to practice it as much as possible, however, if too much energy is conserved, missions may not complete because of lack of resources or because pilots may be unready and under-trained—making this type of solution impractical, unwise and unsafe if practiced more often than it currently is [3].

The third solution of energy efficiency enhancement, if achieved the appropriate way, can boast for considerable immediate and long-term military payoffs. For example, if a novel renewable energy technology could simply convert waste heat generated by the internal machinery of a B-52, C-17 or no-man surveillance drone into usable electrical energy without requiring any additional fuel source, then such a technology would make the entire aircraft a much more energy efficient

system. This is the general idea that has been practically realized and will be further explained throughout this thesis.

With the recently passed Recovery Act bolstering the EERE budget, the DOE is poised to finance many changes on large-scale sites (renovating buildings and eventually replacing petroleum based power generation stations with renewable energy stations). Umstadd has strongly advised under his solution (3) that most government buildings can be refurbished in terms of their heating, cooling and lighting to reduce their current energy consumption by half [3]. Efforts in this respect are already underway, as the DOE has very recently devoted \$5 billion to the ‘Weatherization,’ or efficiency upgrade, of government buildings first, and later private homes and commercial buildings [2]. As for power generation stations, the EERE Office of the DOE is pursuing geothermal technologies research backed by a \$400 million of funding, and has requested a total FY 2011 renewable energy budget of \$520 million for large-scale solar, wind, geothermal and hydroelectric power generation research [2]. The EERE Office has also awarded a total of \$2.4 billion to private companies, such as Ford and General Motors (GM), and universities, such as Purdue University, for advanced battery and hybrid component manufacturing R&D to make American automobiles more energy efficient and less carbon emitting [2]. While civilian vehicle EERE research has gained much attention and is well on its way, navy and military machines such as the abovementioned B-52, C-17 and no-man drone are still in need of well-funded EERE R&D. The next section of this thesis presents a

renewable energy technology, which is able to convert the internally generated waste heat of a military aircraft to usable electrical energy, thus minimizing the need for battery energy and/or petroleum combustion and opening doors for financial, mission-wise and environmental benefits.

1.2: Project Motivation and Objectives

This project was possible due to the collaboration between the Systems & Materials For Power & Protection Systems Branch of the National Surface Warfare Center (NSWC) Carderock Division and the Nanoscale Heat Transfer & Energy Conversion Lab of the Center for Environmental Energy Engineering (CEEE), Department of Mechanical Engineering, University of Maryland, College Park (UMCP). The common research interests of the two collaborating parties, along with the abovementioned EERE needs, had most greatly influenced the nature of the project. Specifically, the NSWC and CEEE had been interested in thermoelectric power generation technology research, and microchannel heat sink research [4, 5]. Furthermore, CEEE Professor Bao Yang had proposed experimentally studying the use of the newly emerging water-in-FC-72 nanofluids (colloidal suspensions of nanoparticles in a base fluid) as coolants in conjunction with a microchannel heat sink [6]. However, due to budget constraints and difficulty of manufacturability of water-in-FC-72 nanofluids, it was later decided that alumina-in-water nanofluids would be used instead [5]. Therefore, a device was designed and constructed as follows: a thin film heater (waste heat simulator) was attached via graphite thermal interface material (TIM) to one surface of two

thermoelectric (TE) power generation modules (arranged electrically in series and thermally in parallel), while a microchannel heat sink was similarly attached to the other surface of the TE modules. The simultaneous heating of one side of the TE modules and cooling of the other side imposed a temperature difference across the modules, inducing an electromotive force (EMF) between the hot and cold sides of the modules as per the Seebeck effect [7, 8]. Once the EMF was experimentally found and the specific TE modules' internal resistance was known, the theoretical maximum TE power generation was computed. Also, the excess pumping power, or the parasitic power of the device, required to pump the coolant through the microchannel was computed from the measured pressure drop readings along with the corresponding flow rates. The difference between power generated by the thermoelectric modules and the parasitic power is finally computed to obtain the net power generation of the device. The general goal of this project has been to achieve a positive net power generation and prove the feasibility of the microchannel-thermoelectric power generator.

In addition to the general project goal stated above, this project was conceived and conducted with more detailed analytical objectives, which, once met, would allow us to scientifically rate the overall performance of the thermoelectric-microchannel power generator. The experimentation was basically done as follows: the abovementioned device was incorporated into a closed test loop in which the coolant was pumped through the microchannel at constant inlet temperature with the heater running for each test run, while pressure drop across

the microchannel was measured by two pressure transducers at each end of the microchannel, relevant temperatures were measured by thermocouples, and the induced thermoelectric EMF was measured and recorded via a computerized data acquisition system. In the experimentation, 3 distinct coolants were used (plain water and two different alumina-in-water nanofluids) in conjunction with the microchannel, with 6 distinct coolant flow rates (all intended and hypothesized to be in the single-phase laminar flow regime) corresponding to each coolant, and 9 different heater settings for each coolant-flow rate set, making a total of 162 test runs that were analyzed and compared to each other. The first objective of this project, had been to compare the measured friction factors (nondimensionalized pressure drop), thus also, the parasitic powers for each test run to their theoretical counterparts (obtained via macrochannel correlations, and microchannel correlations proposed in recent microchannel research articles). The second objective was to assess and make certain the coolant flow regime inside the microchannel for each test run is indeed laminar using a Brinkman Number-based analysis. After sufficiently completing the first and second objectives and understanding the nature of the coolant flow in the microchannel, it was deemed wise to begin the third and perhaps most complex objective. The third objective was to assess the cooling/heat dissipation merit of the coolant conjunct with the microchannel in each test run primarily by computing the experimental mean Nusselt Numbers (nondimensionalized heat transfer coefficient) for each test run and comparing them to each other and their respective theoretically computed counterparts. The third objective was likely to be the most complex due to various

understudied microchannel-related issues, such as conjugate heat transfer effects, microchannel entry effects, viscous effects and slip flow, among others that are likely to be significant in most or all of the test runs. Finally, 1 computer simulation run using the Mechanica subprogram of ProEngineer was performed parallel to each of the 162 experimental test runs to further understand the nature of the heat transfer, particularly conjugate heat transfer effects, occurring in this experiment. Although this is not an optimization study, after completing the experiment and analysis of the type mentioned above, the optimal running conditions, namely, coolant type, heater setting/amount of heat and coolant flow rate, of the microchannel-thermoelectric power generator were determined based mostly on the test run which yielded the total EMF pertaining to the maximum possible net power generation.

The successful completion of this project has resulted in the prototype of a novel renewable energy power generation device, which the NSWC can later expand upon and market to the DOD as a technology falling under the abovementioned energy solution (1) proposed by Umstatt. In addition, this technology could also be seen as a contributor, in a sense, to solutions (2) and (3) because although it does not conserve energy per se and does not necessarily make energy use more efficient, it does conserve nonrenewable battery power and petroleum, reducing their consumption and making the entire system (B-52, C-17, or drone) more nonrenewable-fuel-efficient and ultimately leading to the benefits desired by the DOD and DOE. Specifically, thermoelectric power generation provides solid-state

renewable power generation without carbon or any other gaseous pollutant emissions; also, this device is very compact, lightweight, portable and has no moving parts, requires no regular maintenance and boasts a relatively long service life (typically 100,000-200,000 hours)—making this technology environmentally safe, very reliable and easy to install and apply alongside a traditional battery and petroleum combustion engine [4, 7, 8]. TE technology also emits no signatures of vibration, noise, heat or fume, adding to the stealth and safety of navy/military aircraft and pilot and contributing to overall mission accomplishment [4, 7, 8].

Academically, this project has provided UMCP and the entire engineering community more insight into the relatively new and under-explored research fields of nanofluids and microchannel heat sinks. The remainder of this thesis is mapped out as follows: Chapter 2 presents a literature review on all relevant technologies involved in this project, Chapter 3 describes the microchannel-thermoelectric power generator and test loop design and construction, and explains the experimental and simulation procedures, Chapter 4 presents the results and analyses after experimentation, and Chapter 5 discusses the project conclusions and recommendations for future research regarding microchannel-thermoelectric power generation technology.

Chapter 2: Literature Review

The previous chapter has clearly established the ever-growing energy needs of the U.S. military sector and described a potential renewable energy technology solution in the form of a microchannel-thermoelectric power generator. This chapter presents the research, development and application of the main aspects of the relevant renewable energy technology, namely, the thermoelectric modules, microchannel heat sinks and nanofluids. Since the experiment and analysis of this project have focused primarily on furthering the overall understanding of the physics of laminar single-phase microchannel flows under varying hydrodynamic and thermodynamic conditions, the present literature review will primarily emphasize microchannel research studies and advancements/obstacles in regard to this particular technology. Sections 2.1 and 2.2 of this chapter will discuss the background information, relevant experimental and theoretical studies performed, and ongoing research development efforts in regard to thermoelectric technology and nanofluids, respectively. Next, Section 2.3 will cover a more in-depth review of a number of the most prominent and groundbreaking mechanics, applications and performance studies in the field of microchannels. For the sake of clarity, Section 2.3 is organized such that: Subsection 2.3.1 contains microchannel studies that only involve traditional or base fluids as coolants/working fluids, whereas, Subsection 2.3.2 presents studies, which compare cooling performance of nanofluids to that of their respective base fluids in microchannels.

2.1: Thermoelectric Technology Research

In thermoelectric materials, electrons and holes operate as both charge and energy carriers [7, 9, 10]. Thermoelectric cooling is the direct conversion of electric voltage to temperature difference. The related effects include: Seebeck effect, Peltier effect, and Thomson effect. The Peltier and Seebeck effects are reversals of one another.

The Seebeck effect, which was discovered by Thomas Seebeck in 1821, is associated with the generation of a voltage along a conductor subject to a temperature gradient [7, 9, 10]. As shown in Figure 1, if a temperature gradient applies to a conductor, an electromotive force (EMF), $\Delta V=(V_2-V_1)$, will occur between the hot and cold ends due to charge carrier diffusion and phonon drag. The whole system is in semi-equilibrium; chemical potential due to the concentration is balanced by the built-in electrostatic potential, namely the Seebeck voltage. The Seebeck coefficient α of the conductor is defined as

Equation 1:
$$\alpha = -\frac{\Delta V}{\Delta T},$$

with a positive value when the electrical carriers are holes [7, 9, 10].

Thermoelectric power generators are based on this phenomenon. Note that the Seebeck coefficient is sometimes called the *thermal EMF coefficient* or *thermoelectric power*.

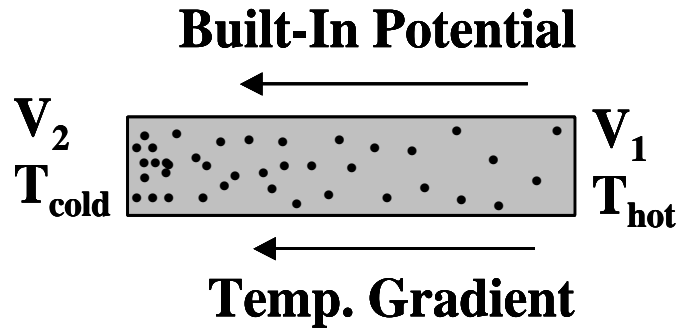


Figure 1: Illustration of the Seebeck effect. Adopted from [7]

The thermoelectric cooling phenomenon is physically based on the Peltier effect, which was discovered by Jean Peltier in 1834, 13 years after the Seebeck effect was unveiled [7, 9, 10]. The Peltier coefficient is a measure of heat carried by electrons or holes. The heat current accompanies and is proportional to the electrical current and is proportional to the electrical current. The proportionality constant is defined as the Peltier coefficient

Equation 2:
$$\Pi = Q/I,$$

where Q is the heat current and I is the electrical current.

When two different materials are jointed together to form a loop, as shown in Figure 2, there will be an abrupt change in heat flow at the junctions because the two materials have different Peltier coefficients. The excess energy released to the lattice causes heating; the deficiency in energy supplied by the lattice causes cooling. An interesting consequence of this effect is that the direction of heat transfer is controlled by the polarity of the electric current; reversing the electric polarity will change the direction of transfer and thus the sign of the heat absorbed/evolved.

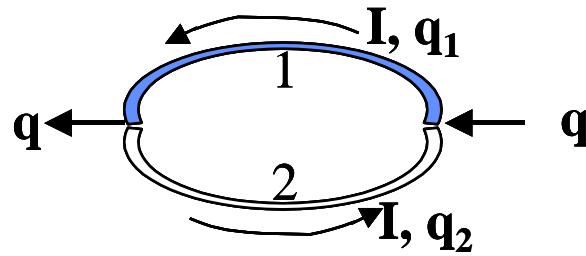


Figure 2: Illustration of the Peltier effect. Adopted from [7]

The Peltier effect is the reverse of the Seebeck effect, and is the principle at work behind thermoelectric coolers or refrigerators, which are used for transferring heat from one side of the device to the other. Thermoelectric coolers are also called Peltier coolers.

The Thomson effect describes the heating or cooling of a current-carrying material subject to a temperature gradient, which was discovered by William Thomson (Lord Kelvin) in 1851 [7, 9, 10]. Any current-carrying conductor, with a temperature difference between two points, will either absorb or emit heat, depending on the material. The Thomson coefficient τ is defined as,

Equation 3:
$$\frac{dq}{dx} = \tau I \frac{dT}{dx},$$

where dq/dx is the rate of the heating per unit length, I the electrical current, and dT/dx the temperature gradient.

It is of great importance in thermoelectric theory that there exist thermodynamic relationships between these thermoelectric coefficients, called the Kelvin or Thomson relations [7, 9, 10],

Equation 4:

$$\begin{aligned} \Pi &= \alpha T \\ \tau &= T d\alpha / dT \end{aligned}$$

The above explanation of the basic phenomena that underlie the operation of thermoelectric devices has been previously introduced by Yang, Ahuja and Tran and can be read upon further in their 2008 journal article [7]. It is pertinent to reiterate that the thermoelectric power generators driven by the Seebeck effect are most relevant to this paper. Thus, this section will bring to light a few scientific studies, which assess the applicability of common commercially available thermoelectric technologies as power generators.

In recent years, thermoelectric power generators (TEPGs) have gained considerable notice for their ability to recovery waste heat from industrial and private sectors and convert it directly to electrical energy. Chen et al. have studied the technical and economic aspects of the large-scale industrial TEPG application intended to supplement a Denmark-based combined heating and power (CHP) system [11]. The study began by theoretically considering a typical CHP system of the form depicted in Fig. 1 of [11]. The relevant CHP system originally produced electrical power and heating power at the efficiencies of $\eta_{el}=40\%$ and $\eta_{th}=50\%$, respectively, making the overall system efficiency $\eta_{el}+\eta_{th}=90\%$. The technological change was computed after the integration of a given TEPG system

into the CHP in three distinct modes. The modes are as follows: Mode 1: placement of the TEPG between the generator and the waste heat boiler, using the temperature difference between the high temperature exhaust gas from the generator and the coolant to produce electricity; Mode 2: placement of the TEPG at the outlet of the waste heat boiler, using the temperature difference between the final exhaust gas from the boiler and the ambient to produce electricity; Mode 3: placement of the TEPG at the condenser, between the inlet fluid to be warmed and the outlet fluid to be used for heating demands. The results are presented in Table 1 below.

Table 1: CHP Efficiency ratings rendered in each mode of TEPG integration

TEPG Integration Mode	TEPG efficiency η_{TEPG} (%)	Electrical Power eff. η_{el} (%)	Heating Power eff. η_{th} (%)	Total CHP system eff. $\eta = \eta_{el} + \eta_{th}$ (%)
w/o TEPG	--	40	50	90
Mode 1	15	40.3	49.75	90.05
Mode 2	5	40.5	50	90.5
Mode 3	1	40.5	49.5	90

From the above results, it is clear that TEPG integration into the CHP system via Mode 2 is the optimal choice because it ideally provides the most notable increase in electrical power efficiency with minimal or no loss of heating power efficiency. Although this option is likely to increase η_{el} with no significant tradeoffs, in practical application, concerns such as boiler chimney corrosion and boiler temperature change could possibly arise and threaten the functionality of the CHP power plant. If Mode 2-based TEPG application is found to be impractical, then Chen et al. have suggested studying Mode 1 application for a more modest gain of electrical efficiency at the small expense of heating efficiency. However, Mode 1

application may not be very practical to most existing CHP plants because of their relatively short (<20 m) exhaust gas tube lengths, therefore, design engineers can ‘fall back’ on TEPG integration via Mode 3. While Mode 3 is not expected to bear risk, its implementation beyond a certain point may be impractical because the increase in η_{el} would come at an equally high cost of η_{th} , thus, dropping heating power supply below the heating demand. In fact, Chen et al. have simulated a Mode 3-based TEPG application to Danish district (co-generation) heating systems that are similar to their theoretical CHP system and found that, TEPGs may yield several desired benefits. Since Modes 1 and 2 were deemed beyond the scope of their study due to lack of experimental opportunity, therefore, only the outcome of Mode 3-based simulation was studied. It was seen that, because of the abovementioned drawback of Mode 3, the TEPG system was only practical in the summer months of June-August when the heating demand is very low and a significant fraction of the heating power efficiency can be exchanged for electrical power efficiency. In favor of TEPGs, it was discovered that, for a TEPG-induced 2.2% improvement in CHP η_{el} , an additional 100 GWh/year of electricity could be produced with a simultaneous reduction in carbon emission by 0.049 measurement tons (MT) and annual reduction in fuel consumption worth 190 GWh/year. Chen et al. are confident that their presentation of the promise of thermoelectric power generation is only the proverbial tip of the iceberg, and that international TEPG research and development will reach monumental heights in the near future.

Maneewan et al. have performed a numerical investigation on private home ceiling heat gain reduction via thermoelectric modules integrated into a conventional roof solar collector (RSC) [12]. This TE-RSC was composed of transparent glass, air gap, a copper plate, TEC1-12708 thermoelectric modules (same TE model is used in this thesis project for its low cost and high efficiency in the relevant operational temperatures as explained in Chapter 3) and a rectangular fin heat sink. Fig. 1 of [12] provides a schematic of the TE-RSC and illustrates its installation into a standard private two-story home with living area and ceiling surface area of 155 and 94 square meters, respectively. The TE-RSC took advantage of the incident solar radiation, in that, from resulting temperature differential across the TE modules, direct current was generated. The TE-generated current was used to power a ventilating fan for cooling the TE-RSC, thus, augmenting attic ventilation that reduces ceiling heat gain. It was found by simulation that the relevant TE-RSC unit of 0.0525 m² surface area generated about 9 W of electricity under 35 °C ambient temperature and 972 W/m² global solar radiation. Due to the TE-RSC, ceiling heat transfer rate fell by 3-5 W/m² (roof heat gain decreased by 25-35%), resulting in annual energy savings of 362 kWh. Maneewan et al. conclude by declaring the TE-RSC to be an interesting cost-competitive energy alternative, especially because of its relatively brief ‘payback’ period of 3.36 years as compared to the 4.36 and 4.37 years for micro fiber or radiant barrier insulation installation, respectively.

Chen et al. and Maneewan et al. have noted that thermoelectric power generation supports current primary heating and power generation systems fairly well with minimal drawbacks, however, it is also mentioned that the TEPG support is typically quite limited and can sometimes become insignificant due in large part to low efficiencies 5-10% of most commercially available TE modules [7, 9-12]. As Da Rosa puts it, optimization of a thermoelectric device depends on three considerations: (1) choosing the appropriate thermoelectric materials in order to maximize the Seebeck coefficient, (2) choosing the best geometry of the thermoelectric materials in order to minimize the product of the heat conductance and internal electrical resistance, (3) simply, matching the load electrical resistance as closely as possible to the thermoelectric internal electrical resistance [9]. The commercially available, best, and simple compound thermoelectric material for power generation around room temperature is bismuth telluride (Bi_2Te_3), which was developed in the late 1950s [7]. Bi_2Te_3 materials usually have figure-of-merit ZT of about 1, which can be raised to about 1.1 by doping with antimony (Sb) to form $(\text{Bi}_{0.25}\text{Sb}_{0.75})_2\text{Te}_3$ [7]. The use of nanostructures for thermoelectric applications was triggered by conceptual studies in the early 1990s that identified the potential benefits of quantum confinement of electrons and phonons and phonon interface scattering [7]. Since then, much attention has been paid to the development of nanostructures for enhancing ZT , and thus, TE efficiency [7]. $\text{Bi}_2\text{Te}_3/\text{Sb}_2\text{Te}_3$ superlattices were reported to have a $ZT \sim 2.5$ around room temperature, which is one of the highest ZT values to date and inspires further nanostructured TE research [7]. Although the currently low commercial

thermoelectric efficiencies limit TE potential, this so-called technical barrier is overridden when thermoelectric devices generate electricity while operating entirely on free waste heat that would have otherwise provided no return whatsoever.

2.2: Nanofluids Research

Nanofluids are solid-liquid composite materials comprised of solid nanoparticles, ranging in size between 1 and 100 nm, that are suspended in a conventional heat transfer liquid (base fluid) [13, 14]. Nanofluids have been experimentally shown to considerably increase the thermal conductivity of most pure conventional heat transfer liquids, indicating their possible worth to the field of novel coolant research. Almost all of the nanoparticle materials studied thus far can be categorized as one of the three broad types: ceramic (i.e. oxides, nitrides, metallic carbides), pure metallic (i.e. copper, silver, gold, iron), and carbon nanotubes (CNTs). In its early stages, nanofluid research was only conducted using ceramic type nanofluids, particularly oxide-based nanofluids (i.e. alumina-in-water) for their greater availability, because only ceramic type particles could be synthesized at the time [13, 14]. Since the present thesis project has researched the use of alumina-in-water nanofluids flowing in a microchannel, the remainder of this section will primarily focus on the relevant thermal transport and hydrodynamic research conducted, to date, on the forced convection behavior of ceramic nanofluids.

Modern nanofluid theory was, first introduced in 1993 by Argonne National Laboratory (ANL) scientist Stephen Choi [13]. Since Choi first described nanofluids and suggested some of their potential benefits for various applications, many researchers have been examining nanofluids and working to discover where their application might be the most fruitful. Current research not only focuses on describing nanofluids by developing theory but also explores the behavior of nanofluids' conduction and convection compared to their base fluid counterparts.

Since nanofluids were first proposed and explored, many scientists have inquired as to what enhancements nanofluids can provide and how they might do so.

Traditional theories originally focused on Maxwell's theory relating to conductivity [13]. As with electricity, Maxwell's ideas were translated to a use in heat transfer. Because nanofluids involve the addition of small particles to a base fluid, many other original theories considered dependencies on particle size, shape and motion within the solution. More modern theories continue to include these dependencies but also focus more specifically on elements of the kinetic theory of gases, Brownian motion, and liquid layering. Das et al. have presented a thorough overview summary of earlier theoretical work completed between 1999 and 2005, which is recommended to readers who are interested in further study in the field of nanofluid developing theory [13]. As mentioned previously, these theories focus mainly on particle geometry and motion. All proposed theories are slightly different in their approaches and assumptions, and there does not seem to be a good agreement as to why and how nanofluids really come about in the way that

they do. More recent theories build directly on the results that are obtained in the lab and further experimentation is also performed solely to understand the physical properties of nanofluids.

Research in nanofluid thermal conductivity enhancement began with ceramic nanoparticles in aqueous heat transfer liquids. Although at first synthesis methods limited researchers to studying only this type of nanofluid, ceramics study was preferred over that of pure metallic and CNT nanofluids because some ceramic nanofluids were relatively well predicted by theory [13-15]. A study by Lee et al. shows that the Hamilton-Crosser (H-C) model does an adequate job in predicting experimentally determined thermal conductivity enhancement with respect to nanoparticle volume fraction of alumina-in-water, as shown in Figure 3(a); on the other hand, the H-C model is found to be quite inaccurate for the prediction of CuO-in-water [13].

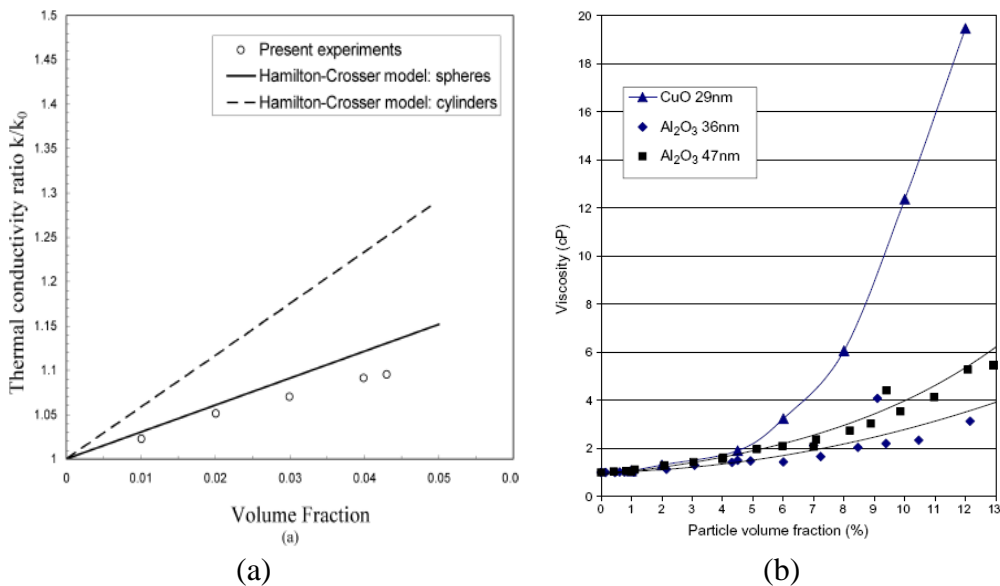


Figure 3: (a) Thermal conductivity enhancement and (b) Viscosity vs. volume fraction of alumina in water. Adopted from [13]

Figure 3(a) also suggests a significant dependence of thermal conductivity enhancement on nanoparticle geometry, namely, cylindrical geometries are more favorable than spherical ones. In support, Das et al. found that for TiO₂-in-water 15 nm sized spherical particles show slightly less enhancement than 10 by 40 nm rods, which showed an enhancement of 33% for a volume fraction of 5%; however, the enhancement using spherical particles was much better predicted by the H-C model [13]. For this reason, much of the earlier nanofluid research was done using spherical nanoparticles; as was the research entailed in the present thesis project (see Chapter 3 for further rationale). Average ceramic nanofluids, added to conventional heat transfer liquids at 1-5 vol%, tend to raise thermal conductivity in the range of 20-30% at room temperature [13-15]. However, most ceramic nanoparticles larger than 10 nm in size are found to greatly raise the viscosity of the base liquid. For example, 29 nm sized aqueous CuO particles double the viscosity of water at only 4.5 vol%, which can be seen in Figure 3(b) [13]. Since the viscosity increase requires much greater pumping power in power generation applications and increases the chance of heat exchanger erosion, high-volume-concentration ceramic nanofluids are not very practical for such applications [14]. In fact, ceramic nanofluids are usually only used for studies in thermal conductivity enhancement, but are still being considered for applications in convection and heat transfer coefficient enhancement. In the relevant thesis project, low-volume-concentration (<1 vol%) alumina-in-water nanofluids were deemed worthy of experimentation because alumina only raises water viscosity very slightly (as seen in Figure 3(b)) in comparison with other ceramics, such as

CuO, while yielding a modest but significant thermal conductivity enhancement (as seen in Figure 3(a)).

While much of nanofluid research has focused on thermal conductivity, several researchers have also explored the enhancement of heat transfer in natural and forced convection through the use of nanofluids. Research has included both simulation and experimental efforts, but most results have returned contradictory and conflicting evidence. Researchers continue to study nanofluid convection in order to understand the pertinent tradeoffs that can occur and how these fluids can be accurately described in this mode of heat transfer. Notably, it is important to understand that research has proven nanofluids to have normal Newtonian behavior [13]. Several researchers, including Wang et al., Pak and Cho, and Choi et al. have conducted experiments in which they observed various nanofluids' viscosity dependence only on temperature, pressure and chemical composition, and not on the forces acting upon them [13, 14]. No experiments to date have provided any evidence that nanofluids display any sort of non-Newtonian behavior. Thus, with reasonable confidence, nanofluids can be assumed to be Newtonian fluids.

Numerical as well as experimental studies have shown promising enhancements for forced convection when nanoparticles are added to a base fluid. The degree of enhancement and the reasons thereof, however, vary depending on the type of nanofluid used and assumptions made. In 2004, Wen et al. numerically studied

the affects of Al_2O_3 nanoparticles in water undergoing laminar flow through a horizontal macropipe [16]. The addition of nanoparticles led to an increase the heat transfer coefficient of the base fluid, which was positively associated with nanoparticle concentration and Reynolds number (Re) of the flow, and was far more pronounced in the hydrodynamic entry region. In fact, it was found that a 1.6 vol% alumina-in-water nanofluid yielded up to 47% higher heat transfer coefficient than plain water at 63 diameter lengths into the tube for a $\text{Re}=1600$ flow. In light of these results, Wen et al. suggest creating ‘artificial entrance’ regions along the pipeline for maximum performance of the alumina-in-water nanofluid, which should be kept below 2 vol% alumina in order to avoid requiring pumping power excess due to elevated working fluid viscosity. It was also observed that the classical Shah equation failed to accurately predict the heat transfer behavior of nanofluids.

Numerical modeling performed by Maiga et al. [17] in 2005 explored the use of alumina nanoparticles with both water and Ethylene Glycol base fluids. Both mixtures were shown to have an enhancement on heat transfer for laminar flow in a uniformly heated tube and through parallel heated discs. Unlike natural convection, the heat transfer coefficient was shown to increase with increasing particle concentration, but it was also shown that this increase in concentration leads to higher wall shear stresses due to viscosity increase. As in most nanofluid studies, the nanoparticles were assumed to be well-dispersed within the base fluid and basic relations for two-phase fluids were used to calculate average fluid

properties. Basic assumptions and relations including continuity, momentum and energy conservation were also used. Results were validated by comparison with other numerical prediction data, models and experimental data, where available. The study indicated that in both cases, with the heated tube and heated discs, heat transfer was enhanced with increasing nanoparticle concentration. Better effects were seen using the Ethylene Glycol base fluid (nearly doubling the heat transfer coefficient relative to the base fluid), however this nanofluid also provided greater adverse affects on wall shear stress (due to tripled viscosity of the nanofluid relative to its corresponding base fluid. The results of this study proved that nanofluids are beneficial in forced convection but also indicate that more research is necessary to find the optimal combination of nanoparticles and base fluid. As will be surmised in Section 2.3 of this thesis, it may have been prudent for Maiga et al. to consider slip-flow conditions at the tube walls for more clarity regarding elevated wall shear stress and nanofluid heat transfer behavior in circular tubes in general.

The current outlook on nanofluid heat transfer behavior commonly held by most members of the engineering community can best be summarized by the conclusive remarks of very recent works by Yang et al. and Heris et al. [18, 19]. After reviewing other nanofluid studies and comparing them with their own, Yang et al. conclude that, in addition to synthesis methods and nanoparticle size and material, the geometry and overall structure of nanoparticles is critical to the level of heat transfer enhancement the nanofluid can provide [18]. Heris et al. believe

the enhancement observed in forced convection is not only due to the enhancement of thermal conductivity of the nanofluid, but also to the motion of the particles within the nanofluid [19]. In addition to particle size and concentration, Heris et al. contribute enhancements to aspects of Brownian motion and particle migration. Although the field of nanofluids remains to date relatively under-explored, leading researchers strongly agree that nanofluids have demonstrated indubitable promise as novel coolants of the future.

2.3: Microchannel Research

Microchannel heat exchangers/sinks, or simply microchannels as they are called, consist of one or more channels with hydraulic diameters around (typically below, but sometimes slightly above) 1 millimeter. Microchannels were originally conceived for tight-spaced, high-heat-dissipation applications that limited coolant flow rate, because they take advantage of a high wetted surface area to unit volume ratio. Tuckerman and Pease are recognized as the pioneering microchannel experimenters, in that, their 1981 study establishes microchannels as feasible heat exchangers for effectively cooling high-heat-density, very-large-scale integrated (VLSI) circuits [20]. In fact, for a 1-cm² VLSI giving off 790 W/cm² of heat, a maximum attached microchannel substrate temperature rise of 71 °C above input water temperature was measured [20]. However, in order to achieve this feat, a high pressure of 31 psi, and proportionately high excess in pumping power, was required to drive water through the microchannel. This study sheds light on the fundamental tradeoff of ‘high heat dissipation vs. excess

pumping power' that is central to understanding and optimizing microchannel design for any given application. Although the preliminary research of Tuckerman and Pease has sparked a keen interest in microchannels among members of the engineering community, they had made a number of unsubstantiated assumptions—leaving important exploration in the relevant field undone. These researchers had taken for granted the typical macrochannel assumptions, such as 'no-slip flow' at the channel walls, fully laminar water flow inside the microchannel, relevant Nusselt numbers (Nu) were in the broad range of 3-9, and that wetted surface roughness played no significant role. As will be seen in Subsections 2.3.1 and 2.3.2, subsequent studies indicate that such macrochannel assumptions are not always valid when studying microchannel flow and heat transfer, as a number of complex phenomena may come into play at the micro-scale. At this point, it is worthy to note that the remainder of this chapter will focus primarily on studies of laminar single-phase flow in microchannels with constant wall heat flux (CWHF) boundary conditions, as they are the most relevant to this thesis project.

2.3.1: Microchannel Studies—Conventional Base Fluid Coolants Only

Sobhan et al. have compiled and comparatively analyzed results from several investigative studies on heat transfer and fluid flow in microchannels conducted before 2001 [21]. Their compilation provides readers with well-organized introduction to the nature and conclusions of the most prominent microchannel investigations of the 1980s and 1990s, and depicts the overall progress in the

relevant field along with uncertainties that were yet to be fully understood. In fact, Sobhan et al. had found that most of the friction factor (non-dimensional pressure drop) and Nusselt number (non-dimensional heat transfer coefficient) correlations for microchannels derived by independent researchers were conflicting with each other and with their conventional/microchannel counterparts. The scattering of these correlative predictions is illustrated in Figure 4 below.

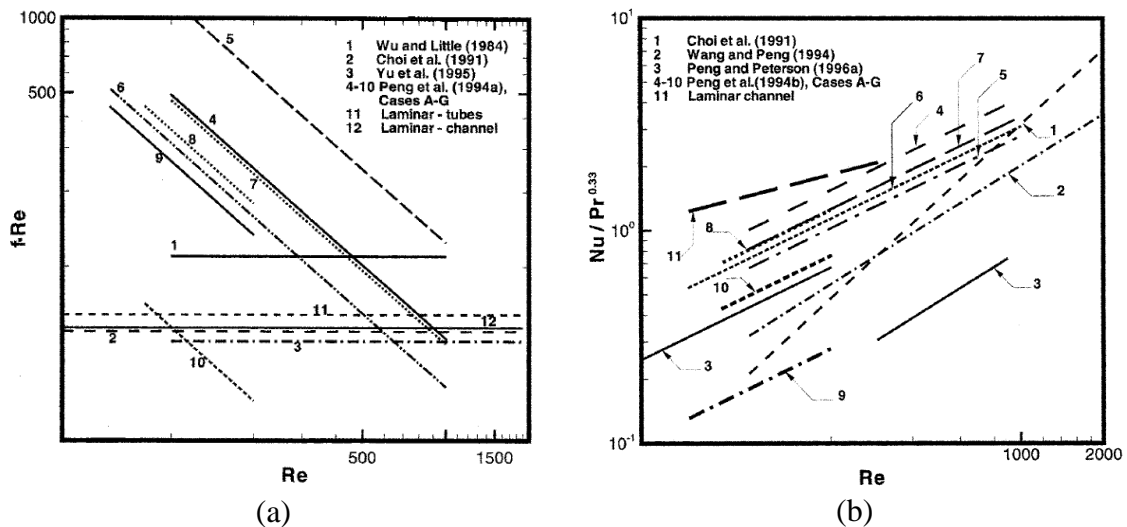


Figure 4: (a) Friction factor and (b) Heat transfer predictions in the laminar flow regime. Adopted from [21]

As can be seen from Figure 4(a), all microchannel friction factor correlations vary greatly in trend and magnitude from their conventional counterpart (Hagen-Poiseuille equation: $f \cdot Re = 64$, labeled as '11' in Figure 4(a)). In fact, the correlations of Wu and Little, Choi et al., and Yu et al. predict constant $f \cdot Re$ values, with the $f \cdot Re$ magnitude being higher than for conventional channels according to Wu and Little, and lower in Choi et al. and Yu et al. In further contradiction, Peng et al.'s rectangular microchannel correlations predict an entirely different trend, that is, in all cases, $f \cdot Re$ is negatively associated with Re . Furthermore, for Peng et al. cases A-C (in which the hydraulic diameter $D_h \geq 267$

μm), the laminar regime was said to extend to about $\text{Re}=700$, whereas for cases E-G ($D_h < 200 \mu\text{m}$), it was believed that the onset of turbulence occurred as early as $\text{Re}=300$. While the slopes for all testing cases, A-G, were identically $\text{Re}^{-0.98}$, the $f \cdot \text{Re}$ magnitude was highest for the largest (D_h) microchannels and lowest for the smallest [21].

From Figure 4(b), it is apparent that all microchannel Nusselt number correlations (by the same researchers as above) also differ in trend and magnitude from their conventional counterpart ($\text{Nu}=4.36$ for laminar flow and CWHF boundary conditions). Notably, the Reynolds number ranges of correlation applicability also vary due to the abovementioned distinct identifications of the end of the laminar regime. It was generally found that Nu depended more strongly on Re in all microchannel correlations (as indicated by the steeper slopes) than in the conventional prediction. Particularly, Choi et al. predicted the strongest positive association of Nu with Re , and all cases A-G of Peng et al. showed the same trend/slope but were all conflicting when it came to heat transfer magnitude at any fixed Re [21].

In conclusion, Sobhan et al. had presented a large disagreement between single-phase, laminar flow microchannel and conventional correlations for Nusselt number and friction factor predictions. However, they did not believe that the scattering of data pointed to unequivocal trends of variation or reasons thereof. Furthermore, no evidence was found suggesting that continuum assumptions were

violated in any microchannel tested. Therefore, Navier-Stokes and energy equations-based analyses should have modeled the relevant phenomena adequately, as long all measurements were taken precisely and experimental conditions were identified correctly. These researchers reason that the inconsistencies in predictions were most likely due to entrance and exit effects, surface roughness differences between microchannels of different studies, lack of understanding of the nature of the thermal and flow boundary conditions, non-uniformity of channel dimensions, and uncertainties/errors in instrumentation, measurement and measurement locations. Sobhan et al. concluded by stating that, as of 2001, there was no reliable prediction of heat transfer rates and pressure drops in microchannels; therefore, they called for further systematic studies which carefully considered each relevant parameter potentially affecting transport in microchannels [21].

A more recent review paper by Rosa et al. has taken into consideration the many inconsistencies between past microchannel studies and possible reasons thereof, and have stated with confidence that conventional correlations can be adequate descriptors of heat transfer and pressure drop in microchannels if certain ‘scaling effects,’ typically negligible in macrochannels, are accounted for [22]. The pertinent scaling effects for single-phase liquid coolants are as follows: entrance effects, conjugate heat transfer, viscous heating, temperature dependent properties, and surface roughness. Similarly as Sobhan et al., Rosa et al. have also suggested more carefully checking, and minimizing if possible, measurement

uncertainties, which may be relatively high due to reduced characteristic dimensions. Therefore, much of the remainder of this chapter will highlight microchannel studies, which focus on one or more of the scaling effects that are most relevant to the current thesis project.

Gamrat et al. have investigated conjugate heat transfer and entrance effects in rectangular microchannels by experiment and numerically simulation using a 3D conjugate heat transfer model [23]. Water was used as the coolant at Reynolds numbers of 200-3000 in microchannels with hydraulic diameters of 0.2-2 mm, and channels spaced apart by 0.1, 0.3, and 1 mm. It was found that both 2D and 3D numerical computations agreed strongly with the continuum model (conventional mass, energy and NS equations) for flow and heat transfer predictions. Thermal transport analysis had shown that entrance effects were dependent on Reynolds number and channel spacing separately, in contradiction to Shah and London's 1978 case of uniform inlet temperature and velocity profiles. Numerical simulations were instrumental to the interpretation of experimental data because the measurements of relevant conjugate heat transfer effects were clearly not possible. It was also found that for a fixed Re flow, entrance effects, namely, increase in Poiseuille number (Po) and Nu, increased slightly as channel spacing was increased from 0.1 mm to 1 mm. A significant reduction (by 40-80%) in measured Nusselt number was observed for microchannels of hydraulic diameter below 1 mm. Their numerical model was unsuccessful in predicting this reduction, despite the model fully capturing the

geometry of their particular experimental setup. The strong reduction in measured Nu could not be clearly explained as it was likely not due to conjugate heat transfer effects (axial conduction in microchannel walls and/or lack of two-dimensionality of heat flux distribution) as the Maranzana parameter (axial conduction-to-convection ratio) was always $M < 0.01$. Therefore, Gamrat et al. concluded by stating that the unexpected Nu reduction probably could have been accounted for had their numerical model considered viscous heating, temperature-dependent fluid properties and thermal expansion effects on the channel spacing.

Tso and Mahulikar carefully considered the scaling effects of temperature-dependent properties and viscous heating as they performed a dimensional analysis on the experimental data from Wang and Peng's 1994 rectangular microchannel study [24, 25]. They attempted to explain the observation that Nu may decrease with increasing Re in laminar regime but may be unaffected in the transition regime. They deduced that the Brinkman number (Br) might better correlate convective heat transfer than the Reynolds and Prandtl numbers. Tso and Mahulikar later conducted their own experiments, in the same regard, with aluminum circular microchannels of 0.73 mm diameter, using water as the coolant [26]. They found that the single-phase forced convective heat transfer in the laminar flow regime in microchannels (with CWHF boundary condition) correlated well with the Brinkman number when experimental data was obtained locally along the flow; however, global correlation with Br yielded a far better trend. Universal correlation of convective heat transfer with Br was possible for

the CWHF boundary condition and relevant experimental data. Despite its relatively low values (order of 10^{-8}), Br correlated the convection. For large Brinkman numbers ($Br \geq 1$), viscous dissipation/heating had become significant as it directly affected the coolant film temperature, and thus, reduced Nu—this was termed the ‘primary effect’ of Br. For large as well as much smaller Brinkman numbers, Viscosity variations coupled the temperature and velocity fields, causing changes in the temperature profile, and therefore, in thermophysical properties of the fluid, ultimately affecting (usually slightly reducing) convection—this was termed the ‘secondary effect’ of Br. Finally, Br was useful in determining flow transition points, in that, if Br values are above Br_{tr} (where $\log(Br_{tr}) = 2.00 \log(Re) - 10.34$) at the given Re, then the flow regime would certainly be fully laminar, otherwise the flow would be in transition towards turbulence.

Celata has recently evaluated previous microchannel research as Rosa et al. have, and is in agreement with them that microchannel heat transfer and fluid flow are not affected by any new, unknown ‘micro phenomenon’ [27]. Again in concurrence with Rosa et al., Celata attributes the inconsistencies in the findings of prior microchannel studies to scaling effects, which are typically insignificant when pertaining to conventional channels but are often very influential in miniaturized systems such as microchannels. The three particularly relevant scaling effects, according to Celata, are viscous heating, thermal entrance length (entrance effects) and axial conduction (conjugate heat transfer). Celata began his

argument by considering a given mass flow rate through a tube. A reduction in the tube diameter would cause a squared increase in fluid velocity. Conventionally assuming that the no-slip boundary condition is valid at the tube walls, it is intuitively clear that the high velocities would also mean high wall shear stresses, resulting in very stretched-out parabolic velocity profiles. This extreme viscous deformation of the relevant flow is the sole reason of exceedingly high pressure drops occurring in microchannels. Furthermore, from the perspective of the Second Law of Thermodynamics, the great effort to drive the flow in microchannels must cause a considerably large irreversible entropic heat loss somewhere—the relevant phenomenon of viscous heat/dissipation is established. As an example, Celata states that a $Re=1000$ (laminar) flow through a 1-meter-long tube with inner diameter of 0.1 mm would raise the fluid temperature on the order of 10 K due to viscous heating alone. When and how viscous dissipation ‘stacks up’ with axial conduction and entrance effects is summed up in Figure 5, though basically, it becomes significant at higher Re . The same high fluid velocity that contributes to the viscous heating effect typically also yields high Graetz numbers (Gz of 200 are common; whereas $Gz < 10$ indicates a ‘fully developed’ temperature profile), and therefore, serves to lengthen the thermal entrance region to span most or all (if channel length is relatively short as it often is) of the microchannel. Additionally, unlike the hydrodynamic entrance effect, which enhances heat transfer (Nu) at the cost of pressure drop increase as described by Gamrat et al. [23], the thermal entrance effect augments heat transfer without increasing pressure drop because this effect does not affect the fluid velocity or

mass flow rate—making the thermal entrance effect quite favorable to microchannel flows, especially at higher Reynolds numbers [27]. Celata has recommended using the Hausen correlation to predict mean Nu as it is fairly adequate in accounting for thermally developing flow, assuming no velocity slip at the microchannel walls and a fully developed velocity profile. Figure 5 superimposes entrance effects among other scaling effects. Though heat conduction in tubes, under CWHF conditions, is ideally only in the radial direction, due to axial inlet-to-outlet temperature difference of the fluid, there is clearly some degree of conduction in the undesired axial direction as well. The coexisting perpendicular convective and conductive heat fluxes are known as conjugate heat transfer. Since conventional heat exchanging channels are thin-walled with relatively large cross-sectional flows, the axial component is typically negligible. On the other hand, microchannel cross sections are often similar in size to their wall thickness, making axial conduction and ensuing conjugate heat transfer effects significant, especially at lower Re flows due to reduced convective heat dissipation—more trapped heat axially conducted through MC → raising coolant bulk temperature and thus, lowering Nu. As Gamrat et al. [23] and most other researchers, Celata relies on the abovementioned Maranzana parameter M to determine significance of axial conduction in microchannel heat transfer. All three major scaling effects considered by Celata are illustrated in Figure 5 below.

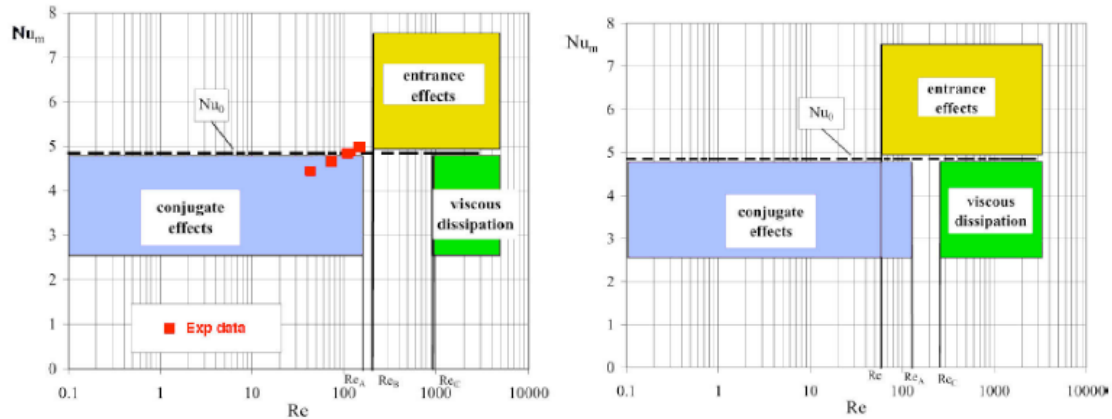


Figure 5: Scaling effects on mean Nusselt number for (left) water and (right) iso-propanol. Adopted from [27]

The thresholds labeled in Figure 5 as Re_A , Re_B and Re_C , above or below which the relevant scaling effects are considered significant are not unique and depend on case-based thermal/flow conditions and thermo-physical properties of the fluid. However, Celata has made the following generalizations regarding scaling effects occurrence: for lower Reynolds numbers ($Re < Re_A$) the axial heat conduction through the solid microchannel wall is coupled to the intended internal convection—this effect is apt to reduce mean Nu ; entrance effects become significant at higher Reynolds numbers ($Re > Re_B$) and tend to increase mean Nu ; also for high Reynolds numbers ($Re > Re_C$) viscous dissipation effects become more notable, tending to reduce mean Nu and counteract the entrance effects. Unlike Rosa et al., Celata does not discuss microchannel surface roughness, wall slip velocity, or measurement error scaling effects, as he regards them as inapplicable or simply non-issues that were dealt with by improvements in microfabrication techniques and standard measurement methodology since the early-mid 2000s [22, 27].

While uncertainties related to measurement error have been greatly reduced over recent years as Celata has mentioned, they remain relevant and are worthy of noting. Rosa et al. have given the gist of the factors that require particular attention in manufacture, design and experimentation to avoid unnecessary errors in measurement as made by most researchers prior to the year 2000 [22]. First, inaccuracy in measurement of diameter and its variation along the channel can directly influence the comparison between measured and calculated values of heat transfer coefficient due to its inverse proportionality to diameter in the laminar flow regime. Second, temperature sensors such as the widely used thermocouples may have dimensions of the same order of magnitude as the microchannels themselves, potentially affecting temperatures of interest (heat loss through thermocouples, disturbance in thermal interface). Third, maldistribution issues and difficulty in measuring representative channel wall temperature can also drastically impair results. Fourth, the classical correlations are valid only under idealized conditions such as constant wall heat flux, which is often non-uniform and is altered by effects such as conjugate heat transfer, channel surface roughness and uneven/improper thermal interfacing.

Baviere et al. have investigated the abovementioned Gamrat et al. microchannel study from the angle of bias in measurement in order to shed light on the strong Nu reduction (40-80% below the expected value for $d_h < 1$ mm), which could not be explained earlier [28]. Baviere et al. began by recalculating actual wall temperatures at the abscissa of each thermocouple and proposed a heat flux-

dependent correction factor to the thermocouple readings to obtain true wall temperature readings—this effort yielded for a far more accurate experimental Nu (in the laminar regime), which was only about 20% lower than the expected value. Furthermore, they performed a complementary experiment that allowed them to estimate the bias effects on the wall temperature measurement due to thermal contact resistance between the thermocouple junction and the brass of the solid blocks. After correcting the thermocouple readings, they proceeded to consider the temperature drop across the brass itself and, ultimately, computed the global error in measuring Nu. With the global error well accounted for, the final experimental Nusselt numbers were reevaluated and found to be in close agreement with the laminar Shah and London classical data for $d_h < 1$ mm. In conclusion to Baviere et al.'s study, Gamrat et al.'s Nu reduction 'mystery' was solved by considering and accounting for measurement error factors of the second and third kinds as listed by Rosa et al.

Although the measurement bias check performed by Baviere et al. on the study of Gamrat et al. was sufficient for clearing up any discrepancy in that case, other cases are not so simply understood. For example, in 2006, Celata et al. declared their experiments with a microtube of inner diameter 0.050 mm to be unaccountable due to intrinsic total error (60-100%) contained within the test setup [29]. The reasons for this large error was originally presumed to pertain to large inertia of the pipe wall in proportion to the small passage of flow at this diameter, and the fact the thermocouples used were of the same diametric size as

the microtube itself (measurement error factor of the second kind as put by Rosa et al.) [29]. With regard to Celata et al.'s unaccountable experiment, El-Genk et al. have reexamined the experimental and numerical values of the temperature rise of the water flowing through the 0.050-mm microtube with the seldom-considered, 'outside-the-box' assumption of velocity slip at the channel walls [30]. Specifically, El-Genk et al. found that by incorporating a slip length of $\beta=1.0 \mu\text{m}$ into the numerical calculations of Celata et al., they would closely agree with the corresponding experimental observations—strongly suggesting the plausibility of slip flow as a relevant phenomenon that cannot be overlooked in microchannels, especially those with diameters of or below 0.500 mm. Generally, El-Genk et al. have found that velocity slip typically occurs under very highly stressed/pressurized flow conditions (with shear rates $>10,000 \text{ s}^{-1}$), and increases with increasing shear rate and decreasing channel diameter. It is most pertinent to note that El-Genk et al. have found that, for fixed Reynolds number, fluid temperature difference across the microchannel and friction factor both decrease with increasing slip length, however, friction factor, along with viscous dissipation, typically falls below the Hagen-Poiseuille value of 64 more rapidly, especially for smaller channels ($D < 0.500 \text{ mm}$). In contrast, when microchannels are very short ($L/D \ll 1500$), thermal entrance effects are significant along with slip, rendering a combined effect, which increases the friction factor above that of the fully developed, no-slip value of 64. El-Genk et al. hypothesized that slip flow can easily occur in microchannels due to driving force overcoming interfacial resistance, which creates a nanolayer (on the order of 10 nm) between the wall

and flowing liquid. In conclusion, El-Genk et al. call for further investigation combining molecular dynamics and continuum flow calculations to determine the nature of the slip. It was also mentioned that wettability and surface roughness might influence slip more than shear rates/flow pressures—particularly, hydrophobic walls have shown pressure loss reductions by 20-40%, whereas hydrophilic walls preclude slip except under highly stressed flow conditions [30].

The final and perhaps most influential microchannel scaling effects are those pertaining to surface roughness. However, the very thorough and recent review done by Rosa et al. suggests not performing any corrections to account for surface roughness on heat transfer [22]. Rosa et al. concluded that surface roughness seemed to have a weak influence on heat transfer in microchannels, often within experimental uncertainties, and depending on cross-sectional geometry, since the Nusselt number was seen to both increase and decrease—ambiguous effects almost canceling themselves out. While Rosa et al. have studied the direct effects of surface roughness, they gave essentially no mention to surface wettability or indirect effects of surface roughness coupled with hydrophobicity, such as velocity slip of liquid coolants at channel walls.

Davies et al. have investigated laminar, periodically repeating flow in a parallel-plate microchannel with superhydrophobic (with contact angle of 177° for water droplets) walls [31]. The walls, which were treated with hydrophobic coating, exhibited microrib and cavity structures (4 μm length and 5 μm depth) oriented

perpendicular to the flow direction. This condition of superhydrophobicity combined with ‘controlled surface roughness’ of the microrib-cavity structure led Davies et al. to observe regions of significant slip within their microchannels. This slip flow helped to achieve a reduction in the frictional pressure drop by up to 50% relative to the classical smooth channel Stokes flow—encouraging the engineering community to design microchannels such that they take advantage of hydrophobicity and ‘controlled roughness.’ Reductions in frictional drag were greater as the cavity-to-rib length ratio was increased (increasing the shear-free fraction of surface area), and channel hydraulic diameter was decreased. Finally, their results also showed that the normalized slip length and Poiseuille number exhibit Reynolds number dependence.

Chakraborty et al. have conducted another enlightening study, regarding hydrophobicity, surface roughness and apparent velocity slip in microchannels [32]. These researchers have investigated entrance region transport in hydrophobic microchannels both experimentally and theoretically. They have verified El-Genk et al.’s nanolayer hypothesis, as it was found that a nanobubble-dispersed layer did indeed exist in the vicinity of the microchannel wall as a consequence of localized hydrophobic interactions. This thin vapor layer was said to act as a shield, preventing the liquid from being directly exposed to the microchannel surface irregularities, and resulting in velocity slip at the wall and reduction of Poiseuille number and viscous dissipation. The main finding of Chakraborty et al. is as follows: for a nanobubble layer formed with a typical

thickness about three orders of magnitude lower than the characteristic microchannel dimensions, the entrance length can be enhanced to a limit over 1.5 times than that for cases devoid of any hydrophobic interactions. Simply put, a longer entrance length implies further enhancement of Nusselt number due to increased entrance effects—raising the merit of the relatively understudied effects of hydrophobic slip coupled with microchannel surface roughness.

2.3.2: Microchannel Studies—Nanofluid and Conventional Coolants

While numerous publications are currently available on the flow and heat transfer of nanofluids in conventional channels and conventional fluids in microchannels, very limited research has been conducted on the nanofluid flow and heat transfer in microchannels. The separately growing popularities of nanofluids and microchannels as novel cooling technologies, along with recent advancements in microfabrication technology and nanofluid synthesis methods, have prompted a few tentative experimental and theoretical studies on nanofluids in microchannels. A few of the most relevant nanofluid-microchannel studies are summarized in this subsection.

Recently, Lee et al. explored the use of 1 and 2 vol% alumina-in-water nanofluids in rectangular copper-based microchannels with hydraulic diameter of 340.8 μm [33]. The high thermal conductivity of 36-nm-diametered alumina nanospheres (36.0 W/m-K) was found to enhance the single-phase heat transfer coefficient by about 1% and 2% for 1 and 2 vol% alumina, respectively, in the laminar regime;

whereas enhancement in the turbulent regime was miniscule due to decreased dependence of heat transfer coefficient h on thermal conductivity k (turbulence: $h \sim k^{0.6}$, laminar: $h \sim k$). Furthermore, higher heat transfer coefficients were observed mostly in the entrance region of the microchannels, similar to that in conventional channels as explained in Section 2.2 of this thesis. However, the enhancement was weaker in the fully developed region, establishing the appreciable effect that nanofluids have on thermal boundary layer development in microchannels. Despite the enhancement of the laminar heat transfer due to increased thermal conductivity, axial conduction through the microchannel walls and decreased specific heat of the nanofluids relative to the base fluid greatly limited this enhancement. It was also observed that nanofluid volume fraction had almost no effect on friction factors for single-phase laminar flow in microchannels. Lee et al. also studied two-phase cooling and found that nanoparticles deposited into large clusters near the channel exit due to localized evaporation once boiling commenced, ultimately completely clogging the microchannels and ending in catastrophic system failure—discouraging further research on two-phase nanofluid flow in microchannels.

Following the research efforts of Lee et al., Wu et al. have similarly experimented with the use of alumina-in-water nanofluids in trapezoidal silicon-based microchannels with hydraulic diameter of $194.5 \mu\text{m}$ and relative roughness on the order of 10^{-5} (smoothness assumption is valid) [34]. Notably, Wu et al. had learned from Lee et al.'s finding that the enhancing effect of rising nanofluid

thermal conductivity on the heat transfer coefficient began to be essentially negated by the simultaneous reduction of nanofluid specific heat with increasing volume fraction at values as low as 1 vol% alumina. With this in mind, Wu et al. tested working fluids of 0.15 and 0.26 vol% alumina-in-water along with pure water. The alumina nanoparticles were 56-nm-diametered spheres. It is also worthy to note to that all experiments were conducted in the Reynolds number range of 200-1300—well within the laminar flow regime—in order to take advantage of higher dependence of heat transfer coefficient on fluid thermal conductivity and relatively long entrance regions in laminar flow as compared to turbulent flow. The single-phase heat transfer coefficient enhancements of 0.15 and 0.26 vol% alumina-in-water were by 4.2-5.7% and 10.2-15.8%, respectively, as compared with that of pure water—an appreciable increase. The corresponding friction factors of 0.15 and 0.26 vol% alumina-in-water increased by 3-4.2% and 3.4-5.5%, respectively, as compared with that of pure water—bearable pumping power excess. Thus, there is a clear indication that the convective heat transfer through silicon microchannels can be enhanced by using the relevant alumina-in-water nanofluids instead of pure water, increasing particle concentration contributes to heat transfer enhancement as long as the volume fraction remains well below 1%. Also for single-phase nanofluid flow in microchannels, the Nusselt number was found to increase with increasing particle concentration, Reynolds number and Prandtl number. Wu et al. also studied two-phase cooling and found that nanoparticles deposited and adhered to channel walls more easily with increasing wall temperature and decreasing flow rate, and once boiling

began, the microchannel cooling system failed very similarly to that of Lee et al., proving once again the total impracticality of researching two-phase nanofluid flow and heat transfer in microchannels.

Bergman employed the traditional ϵ -NTU heat exchanger analysis method to evaluate the turbulent single-phase flow and heat transfer of alumina-in-water nanofluids in rectangular copper-based minichannels with flow cross sections of 5 mm by 0.3 mm [35]. Bulk fluid velocities within the minichannels were within the range of 2-6 m/s, with all simulations corresponding to Reynolds numbers well into the turbulent flow regime. The alumina volume fraction range was 0-5%, inclusive, with 0 vol% denoting pure water. The alumina-in-water nanofluid enhanced heat transfer of pure water by a maximum of about 2%, and the pressure drop was essentially unaffected by alumina volume fraction—substantiating the abovementioned fruitlessness of turbulent flow applications of alumina-in-water nanofluids in conjunction with microchannels/minichannels. In concurrence with Lee et al. and Wu et al., Bergman attributed the virtual non-effectiveness of the nanofluids to offsetting, competing effects of thermal conductivity increase and specific heat decrease with increasing volume fraction.

Jung et al. experimentally investigated the single-phase laminar application of 0.6, 1.2 and 1.8 vol% alumina-in-water nanofluids in rectangular silicon-based microchannels with flow cross sections of 50 by 50 μm^2 , 50 by 100 μm^2 and 100 by 100 μm^2 [36]. Notably, their microchannels had a significant wavy-type

surface roughness of 0.15-0.17 μm due to the etching process used to fabricate them. The alumina nanoparticles used were nominally spherical with diameters of 170 ± 10 nm. In order to make certain that all experimental flows were well within the laminar flow regime, Reynolds numbers tested were between 5 and 300. Jung et al. found alumina-in-water nanofluids to be quite effective, in that, an appreciable increase of over 32% in the convective heat transfer coefficient for the 1.8-vol% nanofluids as compared to the pure water case was achieved in the 50 by $50 \mu\text{m}^2$ microchannels. This as well as the other more significant heat transfer enhancements obtained were observed to occur at higher as opposed to lower Reynolds number flows for the stated reason of longer entrance region and thus greater entrance effects—reaffirming this already well-established finding by Lee et al., Wu et al. among others. Experimental Nusselt numbers were unexpectedly found to be below 0.5, whereas laminar theory for conventional channels predicted all Nu values to be in the range of 4.0-5.6. The reason for this was hypothesized to be high surface roughness of the channel walls, which induced roughness viscosity. Microchannel Nusselt number was found to depend moderately on the Reynolds and Prandtl numbers, contradicting laminar theory for conventional channels. Measured friction factors closely agreed with the Hagen-Poiseuille theory and were essentially invariant with respect to nanoparticle volume fraction—again, fairly consistent with the other studies reviewed in this subsection.

The first section of this chapter discussed thermoelectric fundamentals and a few studies, which explored under-tapped, developing potential thermoelectric power generation technology has to offer. The second section covered the relevant thermal transport and hydrodynamic research conducted, to date, on the forced convection behavior of ceramic nanofluids in macro-sized applications. The third section of this chapter focused primarily on studies of laminar single-phase flow in microchannels with constant wall heat flux (CWHF) boundary conditions, as they are the most relevant to this thesis project. Specifically, Subsection 2.3.1 highlighted studies that pertained to the relevant scaling effects that come into play for microchannel base fluid flow and heat transfer; afterwards, Subsection 2.3.2 alluded to the discoveries and inconsistencies in the scarce amount of microchannel research performed with alumina-in-water nanofluids as coolants. In conclusion to this chapter, alumina-in-water nanofluids have shown promise when applied as coolants in conjunction with microchannels, but this field is highly specialized and requires much further exploration. Thus, the next three chapters will expound upon the work conducted in order to make headway in this specialized field. Hopefully, the review presented here provides interested readers with the framework within which this work was performed so as to achieve a better understanding of it.

Chapter 3: Experimental Apparatus and Procedure

The previous chapter has served to bring readers up to speed with the most pertinent research on technologies relevant to the present project, namely, thermoelectric power generators, nanofluids and microchannels. This chapter will present in detail the design and construction of the relevant microchannel-thermoelectric power generator and the apparatus used to test its performance, as well as the experimental procedure as per the particular research interests of the involved parties (UMCP and NSWC) and pertinent budget constraints that were alluded to in Chapter 1. It is worthy to note that funding for this thesis project was strictly constrained in accordance with the current Advanced Research Projects Agency-Energy (ARPA-E) call for ‘creative and transformational, yet inexpensive or self-funded’ energy research [2, 5]. Also as stated in Chapter 1, the main focus of this project has been to study the heat transfer and fluid flow behavior inside the *microchannel*. Hence, the microchannel (heat exchanger) was considered the central experimental component and was most carefully designed as per the significant microchannel scaling effects mentioned in the previous chapter as well as the need to cater to the fixed dimensions/characteristics of some of the other components involved. Therefore, Section 3.1 of this chapter will present the design and construction rationale of the microchannel heat exchanger component. Further, Section 3.2 will proceed to discuss the design and construction of the relevant test section (the actual thermoelectric power generation device) around the microchannel component. Next, Section 3.3 will

present the design and construction of the relevant closed-loop test rig/apparatus around the test section. Section 3.4 will cover the experimental procedure that was followed to test the performance of the microchannel-thermoelectric power generator. Section 3.5 will conclude this chapter by discussing the procedure of a supplementary computer simulation in support of the relevant experimentation.

3.1: Design and Construction of the Microchannel Heat Exchanger

The microchannel heat exchanger used in all experimental test runs of this project was basically a somewhat thin rectangular block with 12 circular micro-sized channels extruded in parallel for the sake of coolant flow. This section presents the rationale behind the design and construction of this microchannel heat exchanger, or simply microchannel, in terms of material selection, microchannel dimensions and surface characteristics. It is worthy to note the major factors that influenced the design and construction of the microchannel, which were carefully accounted for: the relevant microchannel scaling effects (as expounded upon in Chapter 2), other components of the test section/apparatus and manufacturability limitations which were fixed and had to be designed around, and other issues such as thermal interfacing of the microchannel with other components.

3.1.1: Microchannel Material Selection

It was prudent to begin the design process by assessing potential material choices for the microchannel—a key fundamental as in most heat transfer projects. Upon initially conferring with the involved parties, copper, brass and aluminum were

deemed reasonable material choices due to their relatively high thermal conductivities (approximately 400, 110 and 250 W/m-K, respectively), low cost and commercial availability [5]. The next and perhaps most highly weighted criterion used to assess the applicability of these three materials was their resistance to corrosion. At this point, the possibility of making the microchannel out of brass was immediately ruled out because brass is well known to corrode highly when it comes into contact with flowing water [37]. Particularly, the corrosion would likely have formed a non-uniform layer of oxidized brass that would have born the following adverse/undesired affects on the flow and heat transfer behavior inside the microchannel: considerably reducing the channel diameters, altering wetted surface roughness, invalidating the CWHF boundary condition, causing maldistribution and ultimately leading to unacceptable inaccuracy of experimental data. On the other hand, pure aluminum is known to have excellent corrosion resistance in almost all water (assuming neutral pH and fair purity) flow conditions—encouraging further consideration of aluminum as the microchannel material [38]. The corrosion resistance of copper is intermediate to that of aluminum and brass [37]. Specifically, under most water flow conditions the *smooth* wetted copper surface would typically experience passivation, that is, a uniform layer (almost 1 μm thick) of copper oxide would form immediately between the copper and flowing water and protect the copper from further corrosion. However, as will be discussed later in this section, the relative roughness (to microchannel diameter) of the wetted surfaces of the microchannel used in this thesis project is approximately 10%—reasonably rough.

As pure copper is very hydrophilic, even mild water flow conditions over *rough* copper surfaces can cause non-uniform or ‘pitting’ corrosion to occur, forming copper oxide layers of thickness on the order of a few hundred micrometers.

Although in most macrochannel applications a copper oxide layer of, say, about 300- μm in thickness could easily be neglected; this is not so in the case of microchannel experiments because 300 μm is usually a very significant fraction of diameter as well as most other characteristic dimensions of a microchannel.

Therefore, copper was evaluated to be less than reliable, especially when considering the alumina-in-water nanofluid coolants, for the microchannel design, leaving only the material choice of aluminum at this point in the design process.

As mentioned above, pure aluminum is essentially impervious to any corrosive effects seen in the flow conditions relevant to this project; however, since a minimal amount of *controlled* corrosion of the wetted surfaces was intended as per design, it was finally decided that the microchannel would be made of the aluminum alloy AA 2014 [38]. AA 2014’s composition by weight percent is as follows: 93.5% aluminum, 4.4% copper, 0.8% silicon and 0.5% magnesium; its thermal conductivity is 235 W/m-K, and its density is 2.70 g/cm³, making it much lighter in weight than pure copper (density: 8.94 g/cm³) while remaining sufficiently thermally conducive for the relevant purposes. The relative lightweight of AA 2014 is a notable benefit, in that, the incorporation of a AA 2014 microchannel into an existing no-man surveillance drone design would not weigh down the drone nearly as much as a copper microchannel of the same size.

In keeping with the ARPA-E spirit of ‘self-funded’ projects, cooperation with

other departments within the NSWC allowed for the AA 2014 material, manufacture and assembly of the desired microchannel to be included in a previously ongoing work order, resulting in a delivery of the completed microchannel with no cost to the budget of this project. The Precision Machine & Tool Company located in Beltsville, Maryland manufactured the microchannel. Section 3.1.2 will now proceed further to explain the merit of the material choice of AA 2014 due to its enhancing effect on the microchannel wetted surface roughness and overall performance of the microchannel heat sink.

3.1.2: Microchannel Surface Design

Contrary to most previous microchannel researchers who have designed wetted surfaces to be as smooth as possible in order to minimize pressure drop, the surface of the microchannel used in this project was designed to have a ~10% (with tolerance of +/-1%) relative roughness. This moderate surface roughness was relied on in conjunction with the AA 2014 material and the corrosion it was hypothesized to undergo to considerably reduce the pressure drop below the value predicted by the Hagen-Poiseuille Theory. While AA 2014 is almost entirely aluminum, the small amount of copper it contains reduced its corrosion resistance by what was hypothesized to be just enough for the wetted surface to experience passivation, or uniform corrosion. In preparation of the microchannel, the wetted surfaces were abraded and lightly pneumatically aired, which produced via passivation a uniform layer of aluminum oxide (alumina or Al_2O_3) that would serve to protect from further corrosion [38]. The thickness of the passivated

alumina layer was not noticeable to the naked eye, and was most likely between 20 to 200 nm as per the pertinent literature on aluminum corrosion [38].

Therefore, due to its thinness and uniformity, the alumina layer was considered insignificant in altering the microchannel diameters and wetted surface roughness values. Although AA 2014 and pure aluminum are usually hydrophilic, the alumina layer made the microchannel wetted surfaces highly hydrophobic—yielding a contact angle in the range of 120-150° with water, as per the pertinent literature. Since the type of sophisticated microfabrication and electrochemical resources used by Davies et al. [31] and Chakraborty et al. [32] (see Section 2.3.1 for a description of their work) were not available for this project, the current coupling of conventional wetted surface roughness with passivated hydrophobic alumina layer were meant to achieve similar effects as Davies et al.'s microrib-and-cavity surface with superhydrophobic coating. Namely, the abovementioned design and preparation of the wetted surface were expected to induce a coolant velocity slip at the channel walls, resulting in a significant reduction in pressure drop (relative to the Hagen-Poiseuille Theory) as well as viscous heating across the microchannel. All non-wetted surfaces of the microchannel were smooth. Next, Section 3.1.3 will conclude the microchannel description by covering the remainder of the microchannel dimensions and providing illustrations of the final product as it was applied to the relevant experimentation.

3.1.3: Microchannel Dimensions

With the above parameters set in place, it is now pertinent to discuss the rationale behind the length, width and thickness dimensions of the microchannel heat exchanger as well as the diameter and orientation of its 12 micro-sized channels. Specifically, the microchannel length, width, thickness, channel diameter and channel spacing parameters were 157.0, 40.01, 10.72, 1.44 and 1.75 mm, respectively. Tolerances for these parameters were all ± 0.01 mm. Figure 6 presents an engineering drawing, which illustrates the completed microchannel with all relevant isometric views and labeled dimensions.

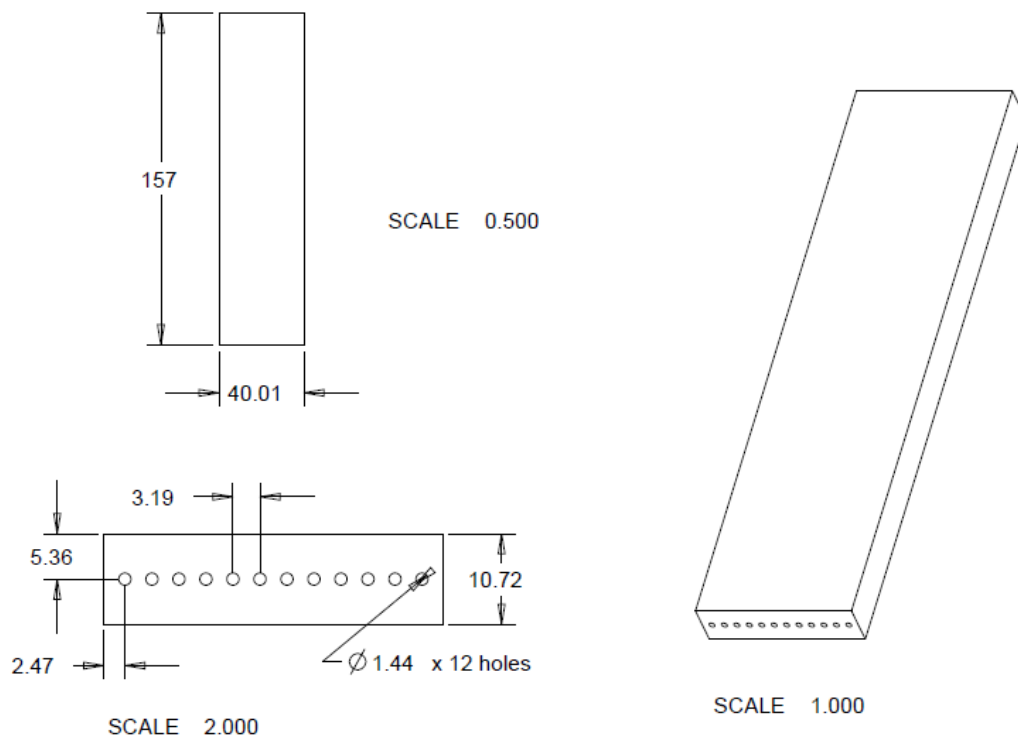


Figure 6: Engineering drawing of the microchannel heat exchanger. All dimensions are in millimeters.

The width of the microchannel was set to 40.01 mm due to the TEC1-12708 thermoelectric electric modules (only available TEPG option) that would interface with its top (40.01 mm by 157.0 mm) surface. As will be explained in Section 3.2,

the TEC1-12708s were 40 mm by 40 mm square-shaped modules with 3 mm thickness—this dimension of 40 mm compelled the microchannel width to be the same in order to maintain the validity of the CWHF boundary condition, minimize heat-spreading uncertainty that would have been inevitably present due to thermal interface methodology, minimize 3D conjugate heat transfer-related complexities, and simply use the microchannel for most efficient heat sinking.

As with most similar designs, it was wisest to minimize the microchannel thickness for apparent and/or intuitive reasons such as: minimization of amount of material to increase compactness and reduce cost, weight and thermal resistance. Another reason to design a thin microchannel was to minimize conjugate heat transfer (axial conduction), as the Maranzana parameter is directly proportional to the difference in the squares of the inner and outer microchannel hydraulic diameters [27]. The abovementioned manufacturer could only machine a microchannel of thickness as low as 10.72 mm (as labeled in Figure 6) without damaging/misshaping the micro-sized channels. This relatively high thickness was originally expected as the manufacturer typically only dealt with macro-sized parts. The 10.72 mm thickness along with its boost to the significance of 3D conjugate heat transfer effects in the microchannel were simply accounted for in the analysis and are explained in Chapter 4 of this thesis.

With the width and thickness design aspects clearly explained above, it is now pertinent to discuss the chosen micro-sized channel diameters and spacing.

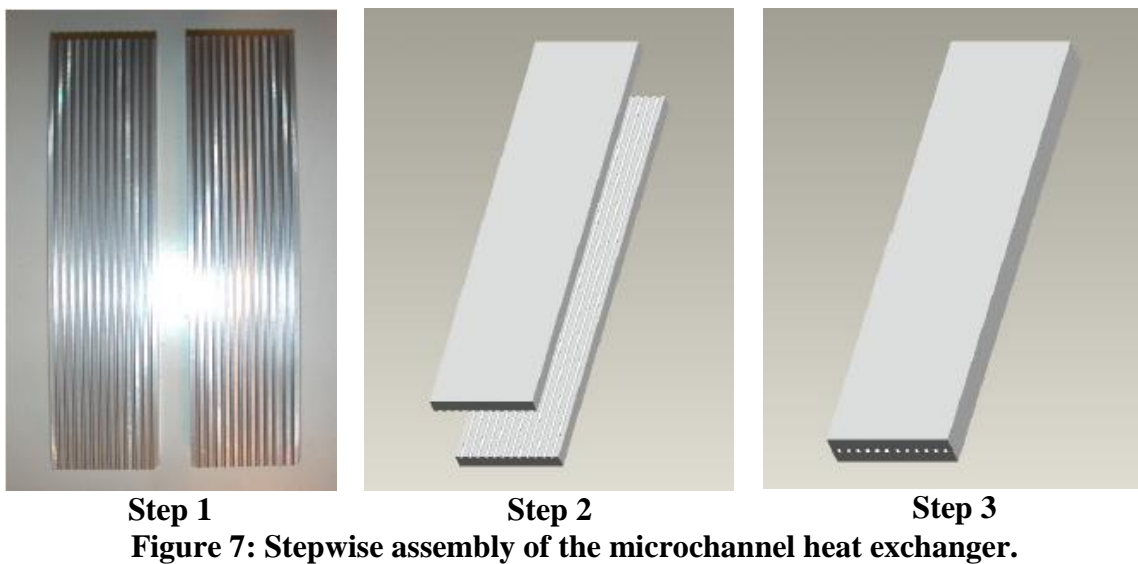
Clearly from Figure 6, the microchannel heat exchanger contains, in parallel, multiple channels of diameters of 1.44 mm and spacing of 1.75 mm between them. Since the microchannel thickness had already been set to the relatively high value of 10.72 mm, it was decided that channel diameters (that is, inner diameters as per the Maranzana parameter) had to be at least 1 mm in order to avoid severe degradation of Nusselt numbers, and thus overall losses in heat sinking and power generation performance of the relevant device, to inevitably significant axial/lengthwise conduction. Furthermore, larger microchannel diameters (>1 mm) were also preferred in this design in order to minimize excess pressure drop, viscous heating losses and experimental uncertainty due to reduced characteristic dimension-related intrinsic error as with Celata et al. [29]. Additionally, larger diameters led to larger Graetz numbers, which meant longer thermal entrance lengths to take advantage of, especially in the case of the nanofluid coolants as explained in Chapter 2. The machining limitations of the manufacturer ultimately decided the lower limit of the channel diameters to be 1.44 mm, hence making this the chosen diameter value. Although reduced channel spacing led to only a slight decrease in Nu in the case of Gamrat et al. [23], Baviere et al. [28], who have extensively studied microchannel spacing issues including those of Gamrat et al., have found that reduced microchannel spacing can sharply lower Nu because it gives rise to axial conduction, especially in thicker microchannels as the one used in this project. In fact, one can easily infer from the work of Baviere et al. that channels should be equally spaced out by a distance equal to or slightly greater than their diameter in order to minimize the adverse effects of axial

conduction on overall cooling performance. Therefore, the micro-sized channels were conservatively designed with a spacing of 1.75 mm. The channel diameter, spacing, and the total width of the microchannel heat exchanger having been set to 1.44 mm, 1.75 mm, and 40.01 mm, respectively, had allowed for a maximum of 12 micro-sized channels. The 12 microchannels were designed to have a circular cross section, as opposed to any other shape, due simply to the fact that circular microchannels are arguably better understood than, say, rectangular or trapezoidal ones as there has been more ongoing and explicative research on circular microchannels that this academic study was able to take advantage of.

The length of the microchannel heat exchanger was designed to be 157.0 mm—relatively long for reasons that will now be explained. Just as the width of the microchannel was basically constrained to be 40.01 mm to match with the TEC1-12708 thermoelectric module dimension of 40 mm, its length is also strongly influenced by the TEC1-12708 modules. In fact, as will be seen in Section 3.2, the top (157.0 mm by 40.01 mm) surface of the microchannel heat exchanger was interfaced with 2 such thermoelectric modules connected thermally in parallel adjacent to each other, thus requiring a minimum microchannel *heated* length of 80 mm. Additionally, taking into consideration the necessity of 2 headers in order to securely connect the microchannel with the rest of the testing apparatus, a reasonable *total* microchannel length had to be at least 100 mm for the relevant experimentation. The finally designed microchannel length, as sent to the manufacturer, was set to 160 mm with a leeway of +/-5.00 mm. Thus, the

microchannel was machined out with a length of 157.0 mm. The microchannel was made a few centimeters longer than necessary for this the current experimentation due to the NSWC's plans for further experimentation, which was not included in the current project. Although longer axial length brought with it the disadvantages of increased pressure drop and potential for 3D conjugate heat transfer, it did serve to reduce experimental uncertainty pertaining to pressure drop measurements. Specifically, the microchannel pressure drop data from 2 pressure transducers at the ends of the microchannel inevitably included small header losses as well, which became reasonably insignificant as the microchannel pressure drop become even higher, due to longer length, than originally designed.

The microchannel heat exchanger was machined as 2 parts, which were carefully assembled, as shown in Figure 7 below, with high-thermal-conductivity silicone sealant (4.0 W/m-K) to complete the central component to the relevant experimentation.



3.2: Design and Construction of the Microchannel Test Section

The microchannel test section was essentially the thematic microchannel-thermoelectric power generator, which was intended to undergo performance testing. This section of the thesis describes the design and construction of the test section around the microchannel component of Section 3.1. First, a brief look will be taken at a test section, which was studied in a somewhat similar research project that provided considerable inspiration to the structural interfacing of the components comprising the test section of this project. Second, the design of the relevant test section will be presented and thoroughly explained in terms of overall arrangement as well as structural and thermal interfacing of the relevant components for the sake of reliable and precise experimentation. Along with the overall design explanation, pertinent details regarding the individual components of the relevant test section will also be provided.

In 2001, the UMCP research team of Moores et al. had designed a test section in order to evaluate the performance of a novel heat sink combining a pin-finned base plate with an open flow-through channel [39]. Clearly from Figure 8 below, their base plate-flow channel heat sink is the counterpart of the microchannel heat sink of this project. It is also pertinent to note that the current characteristic dimensions closely resemble those of Moores et al.'s experiment. The design of their test section components and assembly around the heat sink were of particular interest in the design phase of this project. Figure 8 illustrates the individual components and their assembly to form Moores et al.'s test section.

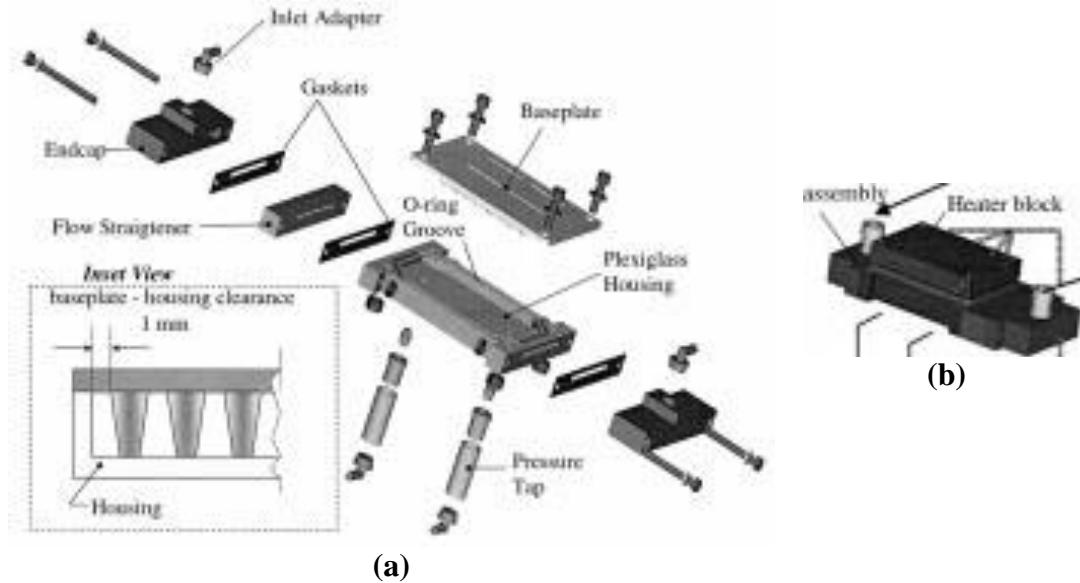
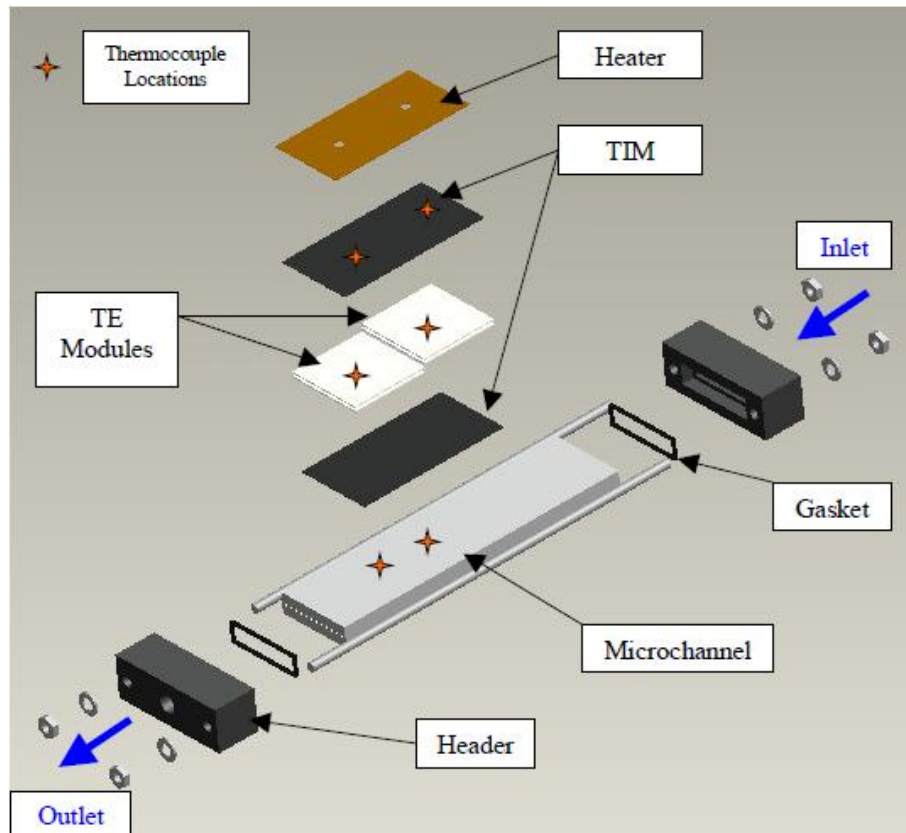
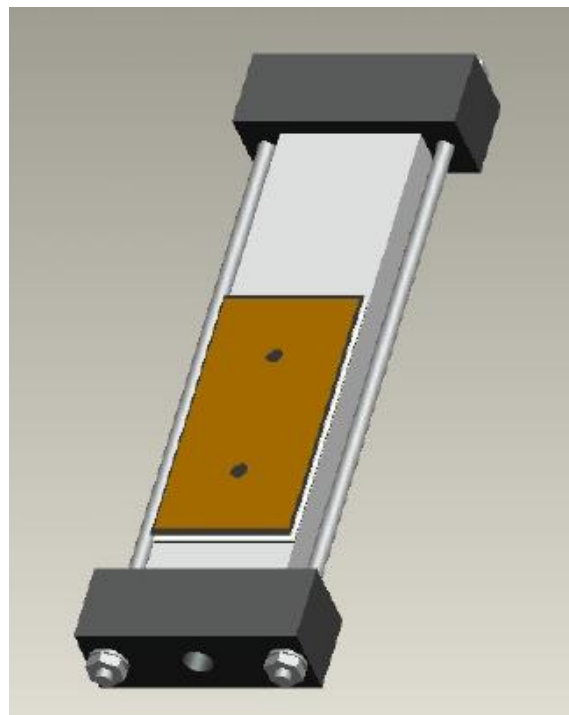


Figure 8: (a) The exploded and (b) unexploded views of Moores et al.'s test section. Adopted from [39]

The test section depicted in Figure 8 had become a ‘tried-and-true’ design since it consistently provided Moores et al. with accurate pressure drop and heat transfer data when uniformly heated from the top surface (with CWHF thermal boundary conditions as in this case). Therefore, the present thesis project was encouraged to take a similar design path as chosen by Moores et al. The relevant microchannel test section will now be presented and described in a compare-and-contrast manner with the abovementioned test section shown in Figure 8. Below, the images in Figure 9 show the relevant microchannel test section during different stages of its assembly.



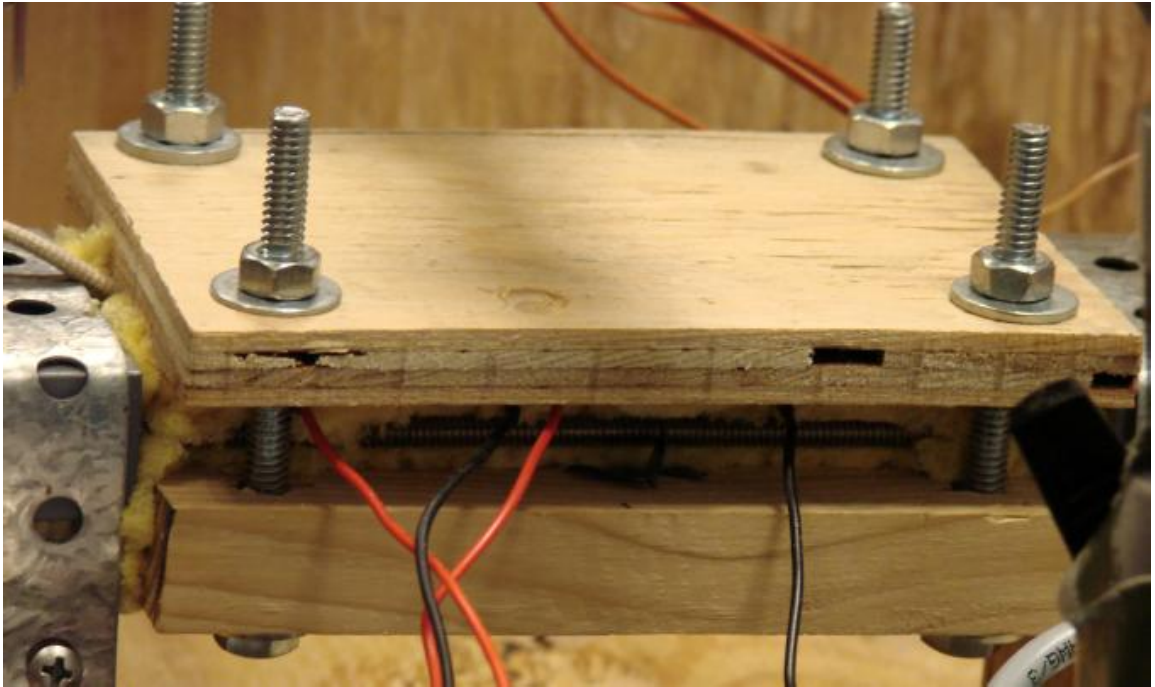
Step 1 (Exploded View)



Step 2 (Unexploded View)



Step 3: (Fully Assembled)



Step 4: (Assembled and Insulated)

Figure 9: Microchannel Test Section at different stages of its assembly.

As clearly seen from the Step 1 and 2 images of Figure 9, the completed microchannel test section bore fair resemblance to Moores et al.'s test section shown in Figure 8 as predicted. Most of the similarity between the two test sections can be found in the header and gasket designs as well as their structural

interfacing with their respective central components (microchannel/fin plate-channel). First, the end-caps (headers) and gaskets used by Moores et al. were made of the thermally insulating materials of plexiglass (0.17 W/m-K) and silicone rubber (0.16 W/m-K), respectively [39], similarly to the present header and gasket material choices of PVC (0.16 W/m-K) and silicone rubber. These material choices were advantageous due to their tendencies to greatly minimize undesired heat losses without the need for additional insulation. In further similarity to Moores et al., the structural interfacing, including secure leak guarding, of the headers and gaskets with the microchannel was achieved via nut-and-bolt type compression as can be seen in Figures 8 and 9 above. The relevant header design deviated slightly from that of Moores et al. as it used a female NPT connection to connect the test section to the relevant test rig instead of connecting to it via specialized inlet and outlet adapters. This particular header design was necessary to accommodate pressure transducers while allowing for secure installation of the test section into the test rig as will be seen in Section 3.3. Figures 10 and 11 below provide readers with the engineering drawings of the relevant headers and gaskets, respectively.

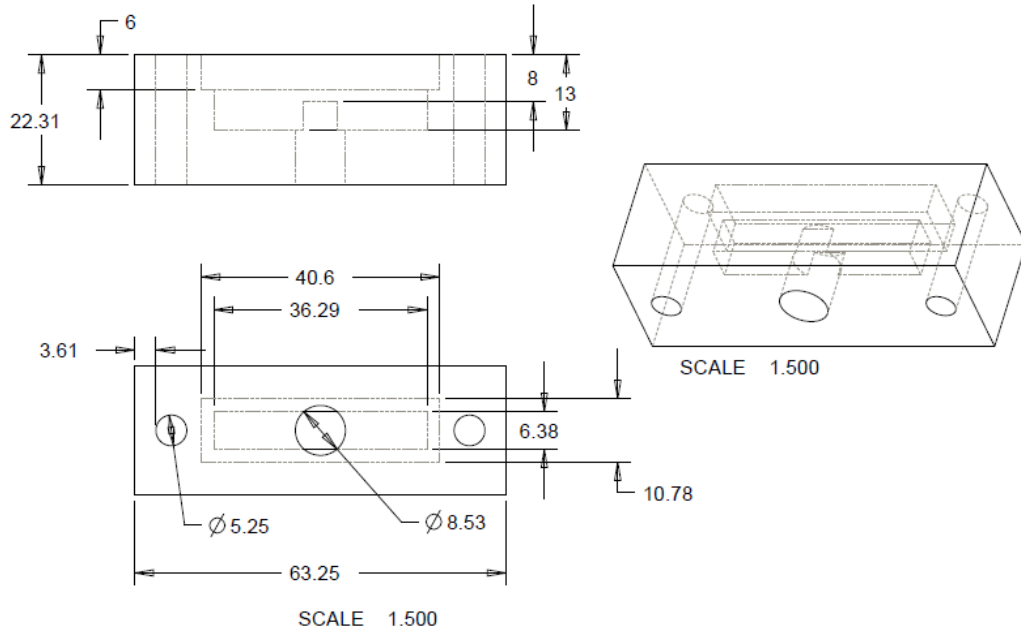


Figure 10: Engineering drawings of the header. All dimensions are in millimeters.

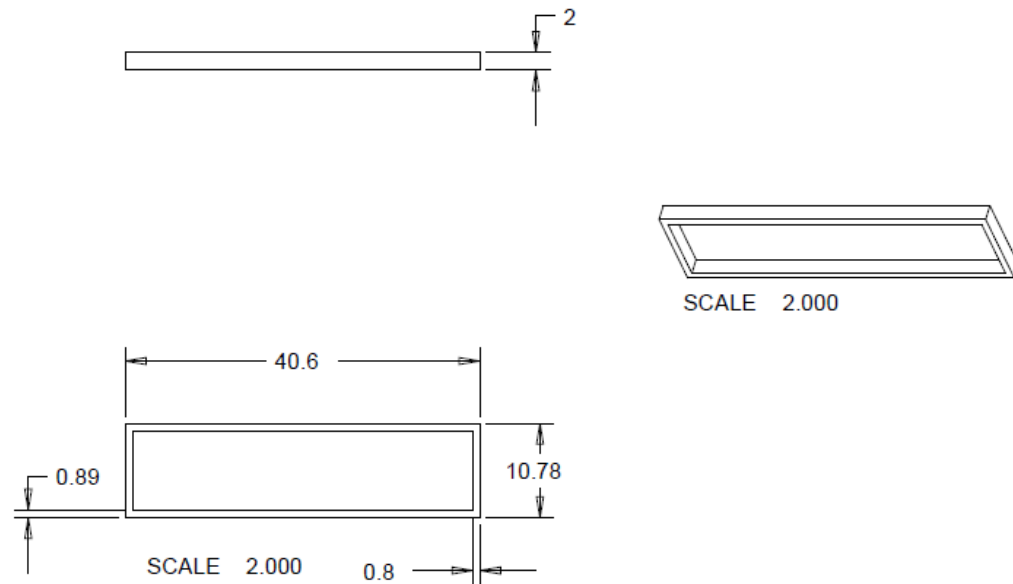


Figure 11: Engineering drawings of the gasket. All dimensions are in millimeters.

Although the structural interfacing methods used by the relevant project and the work of Moores et al. were very similar, thermal interfacing techniques employed by the two works were quite different. Moores et al. achieved a CWHF boundary

condition with the aid of seven cartridge heaters embedded in the custom-machined copper block (shown in Figure 8(b)), which was mechanically fastened on and had direct contact with the top surface of their base plate [39]. Such an approach would have led to severe impedance and non-uniformity in heat flux in the present project as the heater and thermoelectric modules were not specially designed or manufactured but were standard commercially available equipment. At this point, the relevant thermoelectric modules and heater will be described in preparation for the discussion on the pertinent thermal interfacing method. The relevant test section contained 2 TEC1-12708 thermoelectric modules, connected electrically in series and thermally in parallel, for the sake of power generation via the abovementioned Seebeck effect. Specifically, the heater would heat the TE modules' hot side and the microchannel with water/nanofluid coolant flow would cool the cold side, inducing a voltage difference across the TE modules allowing for electrical power to be generated. It must be made clear that the TEC1-12708 modules are designed primarily for cooling applications but can be used for power generation as well. The TEC1-12708s were reliable devices available at no cost to this project and were, thus, strongly recommended as the thermoelectric power generators of choice by the relevant constrained budget and all interested parties. Additionally, as discussed in Section 2.1, Maneewan et al. numerically demonstrated the effectiveness of the TEC1-12708 modules as power generators running on renewable energy [12]. For more information regarding this type of thermoelectric module, readers are referred to the TEC1-12708 Performance

Specifications Sheet [40]. Figure 12 below provides illustrations of the relevant thermoelectric modules.

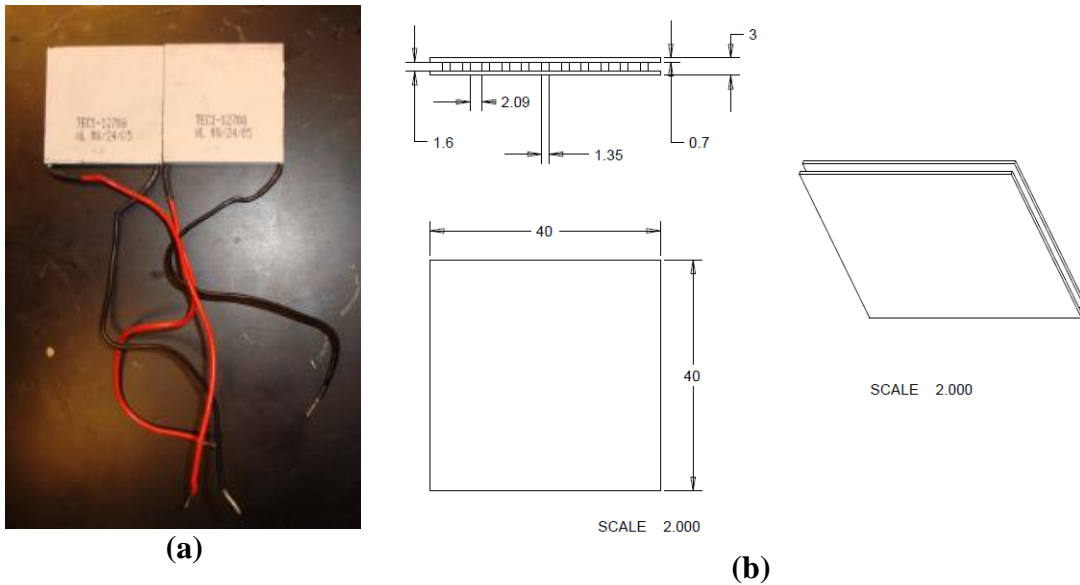
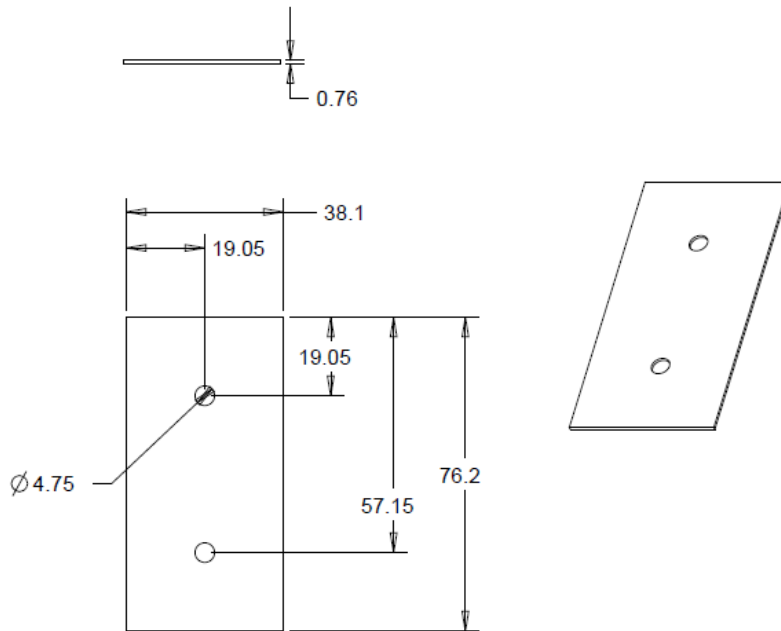


Figure 12: (a) 2 side-by-side TEC1-12708 modules and (b) engineering drawings of the TEC1-12708. All dimensions are in millimeters.

The heater shown in Steps 1 and 2 of Figure 9 that was used to heat the hot side of the thermoelectric modules was a Minco-brand Mica Thermofoil™ Heater with model number HM6800R4.5L36T1. This heater consisted of an etched foil element sandwiched between layers of mica [41]. A 4.5-Ω electric resistance option was selected for the HM6800 heater, allowing for a maximum heat flux of 352 W over an effective area of 2064.5 mm² [41]. Furthermore, the HM6800 was an off-the-shelf heater purchased costing only \$32.00—a price well suited to the relevant budget. The role of the heater in this project was simply to simulate waste heat that would be used as a renewable fuel for the thermoelectric power generators. For more information regarding this HM6800R4.5L36T1 heater, readers are referred to the Minco website [41]. Figure 13 below provides illustrations of the relevant heater.



(a)



(b)

Figure 13: (a) The HM6800R4.5L36T1 heater and (b) corresponding engineering drawings. All dimensions are in millimeters.

Having presented all of the major components of the relevant test section, it is now prudent to discuss the thermal interfacing methodology used to conjoin the heater to the thermoelectric modules, and the modules to the microchannel heat sink. Clearly in Figure 9, the heater, modules and microchannel are compression-assembled using a thermal interface material (TIM) between each component [42]. The particular thermal interface materials used in the relevant test section

were two 0.2-mm-thin plastic-coated graphite sheets having in-plane and through-thickness thermal conductivities of 400 and 3.5 W/m-K, respectively; this TIM was an eGRAF Spreadershield with model number SS020P-400. The TIM sheets were cut out to be 40 mm by 80 mm (3200 mm²) in surface area to match the thermoelectric module surface area and to spread the heat uniformly from the smaller effective heating area of 2064.5 mm² over the intended CWHF area of 3200 mm². The interfacing surfaces of the heater, TE module and microchannel were sufficiently cleaned and laid out with the TIM sheets, as shown in Steps 1 and 2 of Figure 9, and compression-assembled with help of 2 wooden blocks and 4 sets of nuts and bolts as shown in Step 3—this method was reminiscent of that suggested in [42] and strongly assured unobstructed and uniform heat flux as the TIM sheets left essentially no air between the heater, TE modules and microchannel. Finally, the fully assembled test section was completely and securely surrounded by sponge insulation as shown in Step 4 of Figure 9 to minimize any uncontrolled heat losses from conduction and natural convection.

To conclude this section, the location of the 80-mm long heated length of the microchannel and, thus, the corresponding placement of the heater and TE modules will be touched upon. The heated length of the microchannel began at a distance of 60 mm from the microchannel inlet and ended 140 mm downstream from the inlet as can be seen from Step 2 of Figure 9. The heated length was placed closer to the outlet of the microchannel primarily to avoid *hydrodynamic* entrance effects on heat transfer as the Hausen correlation and most specialized

microchannel correlations do not take hydrodynamic entry into consideration—a largely academic reason to explore only laminar single-phase *hydrodynamically fully developed* liquid flow and heat transfer in this project.

3.3: Design and Construction of the Microchannel Test Rig

The microchannel test rig was basically a closed-loop flow cycle, which was made to test the performance of the relevant microchannel-thermoelectric power generator (the abovementioned test section) by regulating such pertinent parameters as coolant temperature and flow rate and heat flux from the heater. At this point, the design and construction of the test rig around the relevant microchannel test section will be discussed. This section will begin by describing the ‘double-loop’ design of the *entire* test rig that was constructed at the NSWCC for a planned series of experimental projects starting with present project. Additionally, this thesis will cover the ‘single-loop’ *part* of the test rig that was used in the experimentation of this thesis project.

The design of the complete experimental test rig was originally conceived as a double-loop closed flow cycle in order to dedicate the primary loop largely to the plain water coolant while having a secondary loop available, if necessary, for nanofluids and/or non-water coolants that may not be materially compatible with the water chiller/recirculator apparatus belonging to the first loop. Schematics of the test rig, in its ‘double-loop’ entirety and ‘single-loop’ part, are provided below in Figures 14 and 15, respectively.

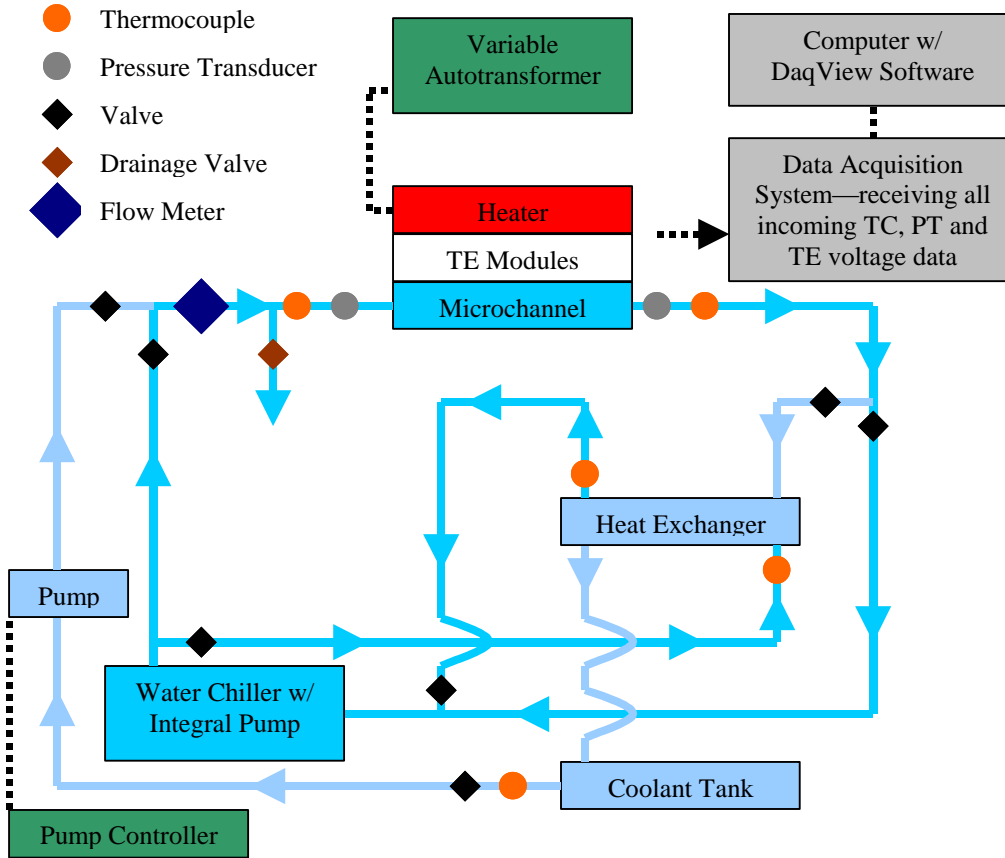


Figure 14: Schematic of the entire test rig with both the primary and secondary flow loops.

When water was selected as the coolant, it was simply pumped from the water chiller directly to the microchannel (test section) and returned to the water chiller—this flow path, drawn in aqua blue in Figure 14, was defined as the single or primary loop, which could have been, and in fact was, used by itself. In primary loop flow, the water chiller controlled the coolant temperature at the microchannel inlet, and the coolant flow rate was monitored by the flow meter and controlled by partial opening and closing of the valve between the chiller and microchannel. When the secondary loop, drawn largely in sky blue in Figure 14, came into use, the coolant tank stored the coolant; the external pump with electronically attached pump controller pumped the coolant to the inlet of the

microchannel and regulated its flow rate; the external heat exchanger, with the help of cold water cycling to and from the water chiller, would then cool the heated coolant back to its controlled microchannel inlet temperature and allow it to flow back to the coolant tank to complete the cycle. Since all of the coolants tested in this project were water-based, they did not present an erosion threat to the storage area of the water chiller; therefore, only the primary/single-loop part of the test rig was active in the relevant experimentation of this project. For the sake of clarity, the active single-loop part of the test rig is shown in Figure 15.

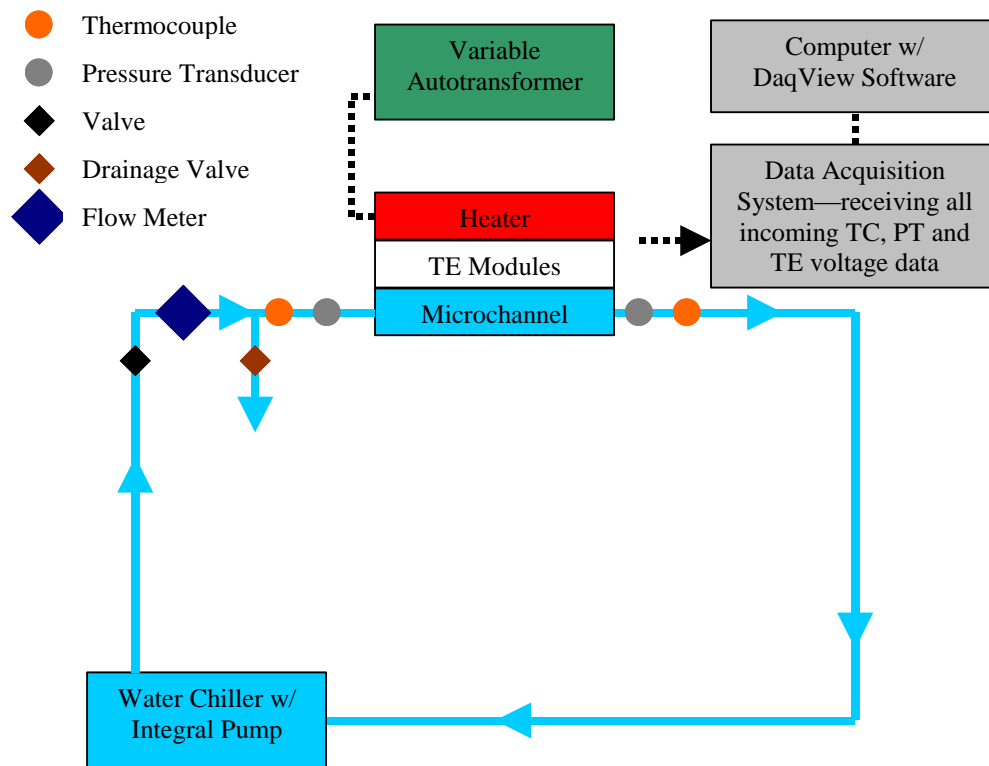
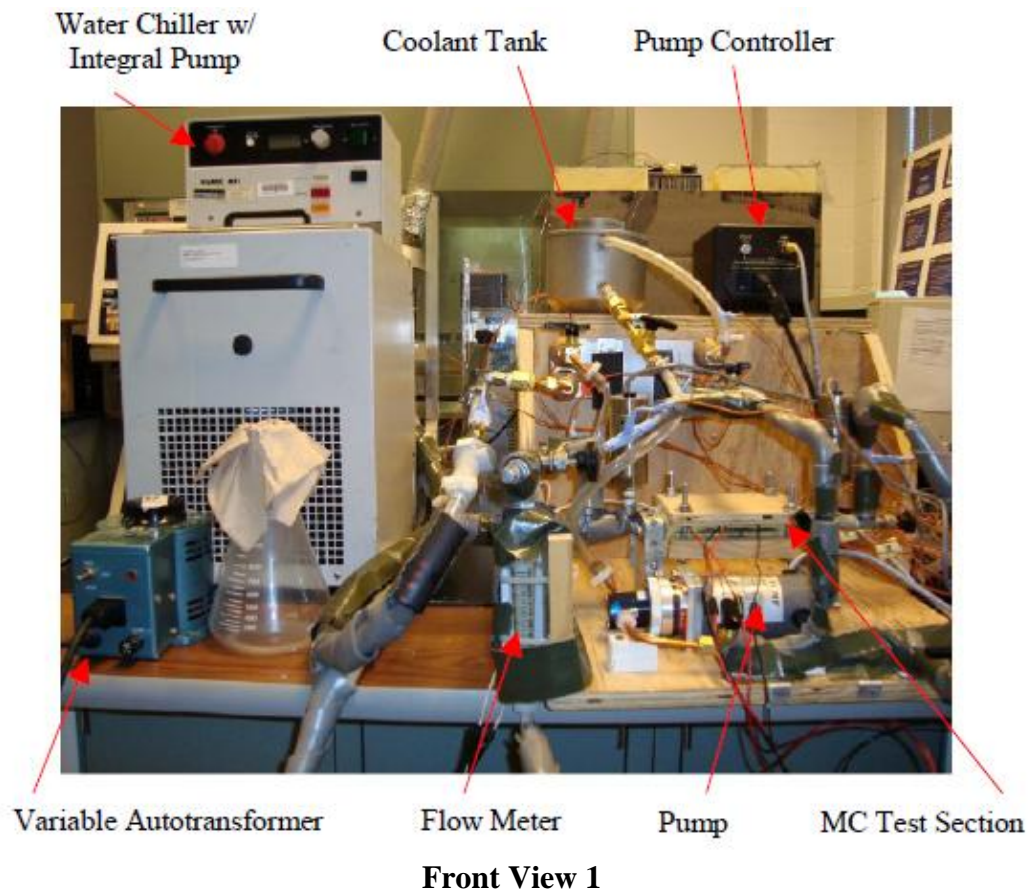
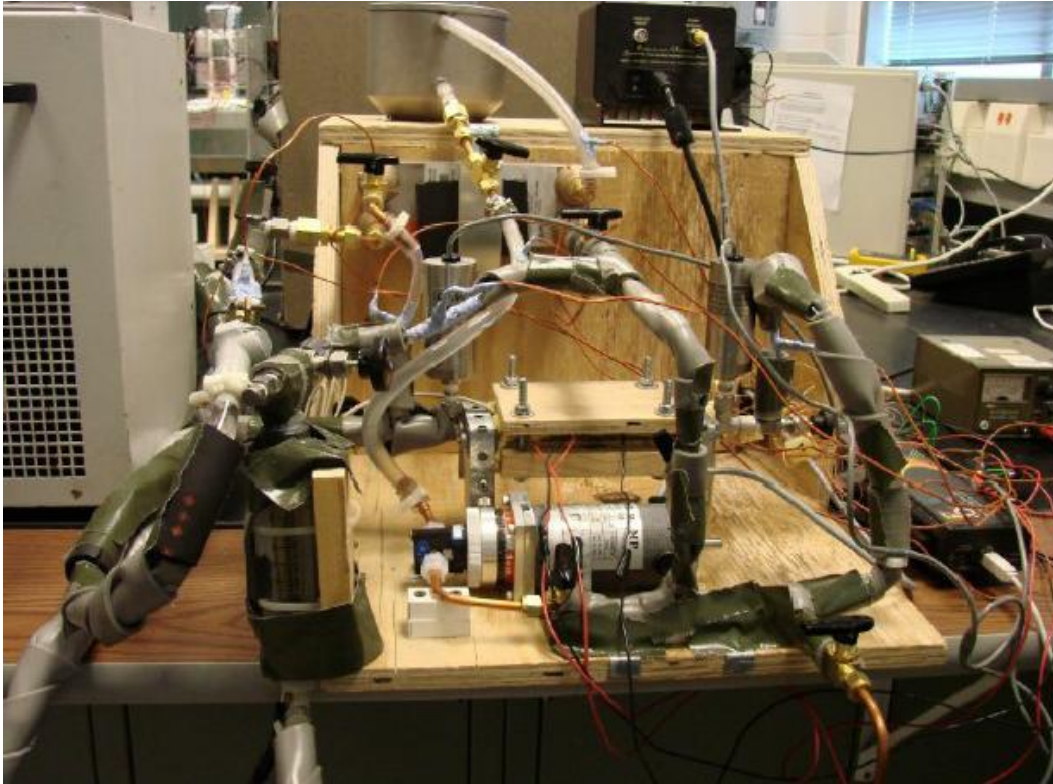


Figure 15: Test rig schematic—primary/single loop part only.

Although the secondary loop of the test rig was not needed for the present experimentation, the entire test rig was carefully constructed and iteratively revised in terms of assembly techniques and materials to yield a reliable final product that allowed for precise, meaningful experimentation and data acquisition. Actual photographs of the completely constructed test rig (as per the schematic in Figure 14) are provided in Figure 16.

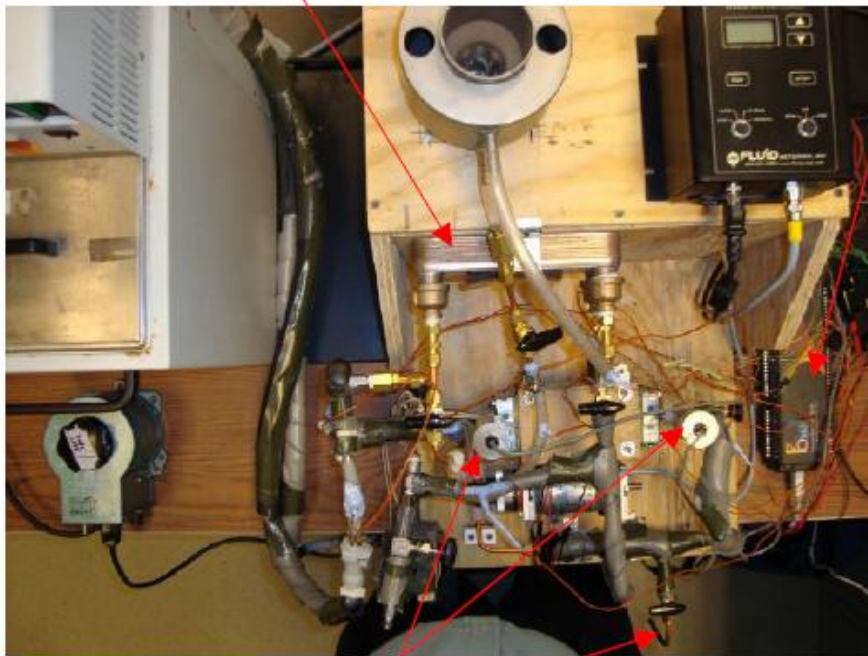




Front View 2

Heat Exchanger

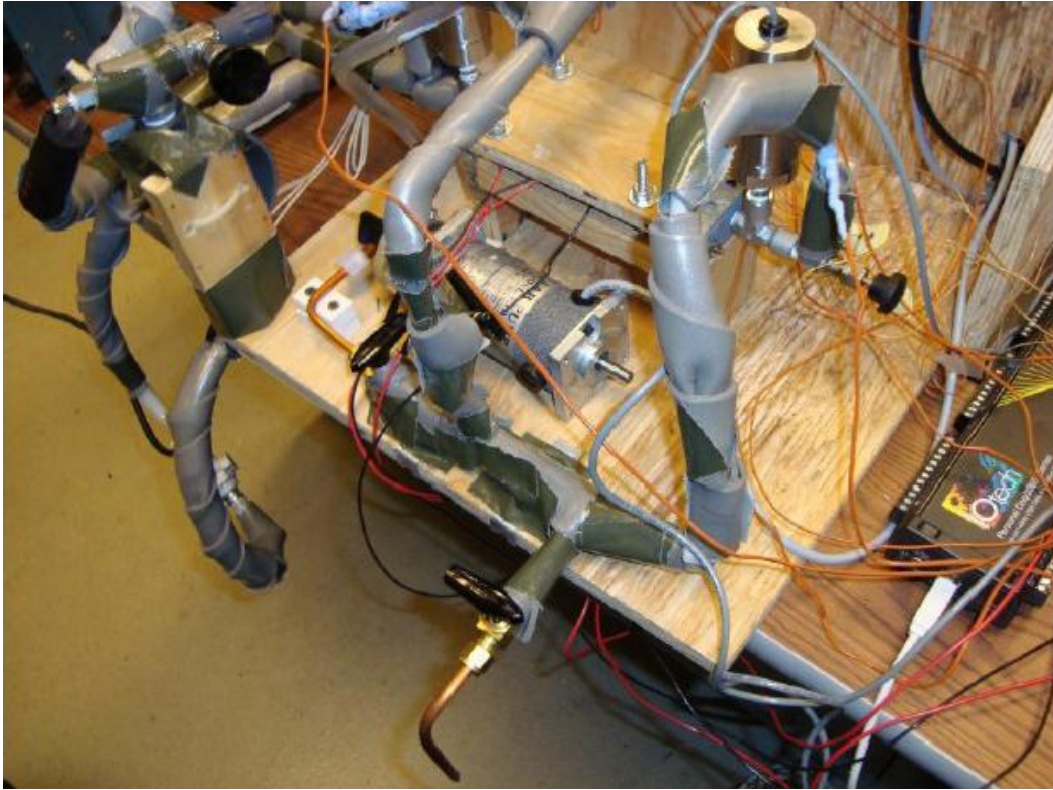
Data Acquisition System



Pressure Transducers

Drainage Valve and Port

Top View



Angled View

Figure 16: Photographs of the Microchannel Test Rig.

As can be seen from Figure 16, the structural base of the test rig was made of wood, upon which most of the major components/apparatuses were securely mounted. The tubing, fittings (leak-guarded with Teflon tape) and valves applied to regulate the coolant flow between the relevant components were standard commercially available products made of copper, plastic, brass or stainless steel. The tubing of the single-loop part of the test rig was insulated with standard wrap-around insulation—the gray elastic material shown in Figure 16—to minimize any uncontrolled conductive or convective heat losses. The drainage valve was always fully closed during experimentation but, as the name suggests, it was opened only when the coolant had to be drained out for replacement. The

abovementioned items, along with the major components of the test rig, were borrowed from or traded for with other departments within NSW at no cost to the relevant budget in accordance with the largely self-funded nature of this project. The water chiller with integral pump that was used to cool and recirculate the coolants through the test rig was a Haake A81, which was sufficient for these purposes and was materially compatible with water as well as the alumina-in-water nanofluid coolants. The flow meter shown in Figure 16 came with the Haake A81; although it was pre-calibrated, the flow meter's accuracy was checked against manual flow rate measurements and was found to be ± 0.005 liters per minute (LPM). The test section consisted of the heater, TE modules and microchannel as was presented in Section 3.2. The device used to vary the amount of heat flux from the heater was a Staco Type 3PN1010 Variable Autotransformer; the heater with autotransformer was checked against previously recorded practical data and found that the accuracy of the heat flux setting pertaining to the relevant experimentation was $\pm 0.003 \text{ W/cm}^2$. The pump placed in the secondary flow loop was the Fluid Metering Inc.-brand (FMI) RHV1CTC—a valve-less variable speed pump, which is controlled by a V300 Automatic Rate Controller. The RHV1CTC was an adequate choice in terms of flow rate requirements and was strongly resistant to unwanted chemical reactions with a wide range of coolants due to its wetted parts being made of Tefzel. The secondary-loop heat exchanger choice was the Paul Mueller Company's WP1 Brazed-Plate Heat Exchanger. The WP1 was compact, lightweight (2.64 lbs), yielded minimum pressure drop, and was designed to sufficiently exchange heat

between the hot working fluid and cold water from the Haake A81. Additionally, the WP1 was made of stainless steel and brazed with 99.9% pure copper to make it resistant to acids and most other erosive chemicals. The coolant tank of the secondary loop was simply an aluminum vessel used to store the coolant. All temperature sensors used within the test section and tubing of the test rig were K-type thermocouples, which appear as orange wires in Figure 16 and orange dots in Figures 9, 14 and 15. A total of 8 thermocouples were *actively used* in the relevant experimentation: 1 at the test section inlet, 1 at the test section outlet, and 6 within the test section as shown in Figure 9 (3 thermocouples located 80 mm downstream of the microchannel inlet and the other 3 located 120 mm from the inlet). All thermocouples were connected to the data acquisition system and then calibrated with the help of pre-calibrated thermocouples provided by the NSWC to an accuracy of ± 0.01 °C. Similarly, all TEC1-12708 wire leads (the red and black wires seen coming out of the test section and going into the data acquisition system in Figure 16) were connected to the data acquisition system; the thermoelectric modules were basically set to give zero-voltage readings for zero temperature difference, and were calibrated to an accuracy of ± 0.001 V. The pressure transducers used to measure the pressure at the inlet and outlet of the microchannel were manufactured by GP:50 and had the model number of 311-B-PP-2/CZ. These two pressure transducers were the metallic cylindrical objects seen in Figure 16 that were mechanically connected to the T-fittings at both ends of the test section and electrically connected to a Hewlett Packard HP 6218B Power Supply for power and the data acquisition system for pressure data

management. The pressure transducers were calibrated to an accuracy of +/-10 Pa (gauge) with the assistance of a precise manual manometer. All temperature, pressure and voltage data were acquired by an Iotech Personal Daq/3001 Data Acquisition System (pDaq3001), supported by a PDQ30 Analog Expansion Module for extra ports to accommodate all sensors. The pDaq3001 was connected to a computer with DaqView software, to which it sent the relevant data for recording and management.

3.4: Experimental Procedure

The purpose of the relevant experimentation was to evaluate the performance of the microchannel-thermoelectric power generator (MC-TEPG) under varying forced convection conditions. Specifically, the pertinent variables were heater setting/heat flux amount, coolant flow rate, and coolant type. The heat flux amount was discretely varied 9 times between 0.341 and 3.41 W/cm² at increments of 0.341 W/cm², corresponding to heater settings of 2-20% of its maximum, 17.05 W/cm², on the autotransformer. The maximum allowable heater setting of 3.41 W/cm² was limited by the 138 °C-melting point of the BiSn solder used to construct the TEC1-12708 modules [40]. Similarly, the 6 discrete coolant flow rate settings were as follows: 0.56, 0.78, 0.99, 1.13, 1.36 and 1.53 LPM. The maximum allowable flow rate of 1.53 LPM was limited by the maximum pumping power of the integral pump of the water chiller as well as the <2000 Reynolds number condition for fully laminar flow. The 3 coolants tested were plain deionized water, a 0.13-vol% alumina-in-water nanofluid (referred to as

NF1), and a 0.50-vol% alumina-in-water nanofluid (referred to as NF2). The alumina nanoparticles dispersed in both relevant nanofluids were approximately spheres with diameters of 30 nm. Table 2 provides the pertinent, experimentally verified thermophysical properties of the above 3 coolants.

Table 2: Experimentally obtained coolant properties at 12 °C.

Property Coolant	Thermal Conductivity (W/m-K)	Specific Heat (J/kg-K)	Dynamic Viscosity (Pa-s)	Density (kg/m ³)
Water	0.592	4184	0.00105	998
NF1	0.716	4172	0.00106	999
NF2	0.728	4125	0.00128	1001

In short, coolant type, flow rate and heater setting were varied 3, 6 and 9 times, respectively as mentioned above, yielding a total of 162 (multiplicative product of 3, 6 and 9) distinct test runs, of which the relevant experimentation was comprised. All experimentation conducted in this thesis project was done so under the following heat transfer and flow-related assumptions:

1. steady, *hydrodynamically* fully developed flow;
2. thermophysical properties of the coolants were invariant with temperature;
3. incompressible flow;
4. all coolants were continuum media;
5. all coolants were Newtonian fluids;
6. constant-wall-heat-flux (CWHF) boundary condition over the abovementioned 80-mm heated length;
7. insignificant heating (<10% of total heating) due to viscous dissipation;
8. the combined effects of wetted surface roughness and hydrophobicity such as slip-flow were significant.

It is worthy to note that Assumptions 1, 3, 4 and 5 were essentially taken for granted due to the numerous arguments made in the Chapter 2 regarding typical assumptions that had been found to be indubitably valid in past studies.

Assumption 2 was strongly believed to be valid because it was hypothesized that the inlet-to-outlet temperature rise of the coolant would never exceed 5 °C, making all temperature-based property variation very insignificant. Assumption 6 was simply made for the sake of convenient and systematic analysis, and was checked later. Assumptions 7 and 8 were ‘taken with a grain of salt’ but, along with most other microchannel scaling effects, were later checked in the results of the relevant experimentation.

With the pertinent details as to the nature of the present experimentation having been covered above, it is now prudent to discuss the actual experimental procedure of this project. Before beginning the experimental test runs, all components of the test rig were finally checked for cleanliness, complete functionality, and all valves, including drainage and excluding the one shown in Figure 14, were fully closed to ensure that the complete test rig of Figure 16 only allowed single-loop flow as shown in Figure 14; also, the data acquisition system and computer with DaqView Software was on and monitoring the thermocouple, thermoelectric voltage and pressure readings. The step-by-step experimental procedure was as follows:

1. pour the coolant (deionized water, originally) into the water chiller and set the coolant temperature at 12 °C—making this temperature the microchannel inlet temperature for each test run;
2. turn on the water chiller and wait until the coolant is cooled to 12 °C;
3. partially open the flow rate-adjustment valve (the one in Figure 14) such that the flow rate of the coolant is 1.53 LPM;
4. turn the variable autotransformer (and heater) on and set it to the highest allowable heater setting for the currently running flow rate (20% for 1.53 LPM, and 18% for the other 5 flow rates);
5. wait for steady-state heat transfer conditions, that is, all thermocouple temperature, pressure transducer and thermoelectric voltage readings stop changing by more than 0.1 °C, 10 Pa and 0.001 V, respectively;
6. have DaqView record the temperature, pressure and TE voltage readings of the current test run (note: once steady state was achieved for each test run, DaqView was set to take and record all relevant sensor readings 45 times over 7.5 minutes with all recordings taken 15 seconds apart—these raw data were saved in spreadsheet form as the results);
7. for the currently fixed coolant type and flow rate, decrease the heater setting by 2%, then repeat Steps 5 and 6;
8. continue to repeat Step 7 until a total of 9 test runs, all with distinct heater settings, are completed for the current flow rate and coolant;
9. repeat Steps 3-8 5 times, each time decreasing the flow rate in Step 3 to one of the 5 other abovementioned flow rates (1.36, 1.13, 0.99, 0.78 and 0.56 LPM)

- until all heater setting and flow rate combinations have been covered—
making a total 54 test runs for the current coolant;
10. turn off the heater and autotransformer;
 11. open the drainage valve to completely drain the current coolant from the test rig;
 12. turn off and power down all machinery that is still in running;
 13. repeat Steps 1-12 twice: the first time, using NF1 as the coolant, and the second time, using NF2 as the coolant—completing all 162 test runs each with a distinct set of heater setting, flow rate and coolant type.

The analysis of the results obtained from the above experimentation discusses the values and trends of heat transfer coefficients, friction factors, and power generation maximums, as well as the significance of the pertinent scaling effects mentioned in Chapter 2. Results and analysis discussions are presented in Chapter 4 of this thesis.

3.5: Simulation Procedure

Although this thesis project had largely focused on experimental research, a modest numerical research effort was put forth in order to bolster the experimental results and analysis. Specifically, the numerical research was a basic thermal simulation performed on a *portion* of the relevant test section using ProEngineer Wildfire 3.0 and its Mechanics subprogram. The simulated portion of the test section and its engineering drawings appear in Figures 17 and 18.

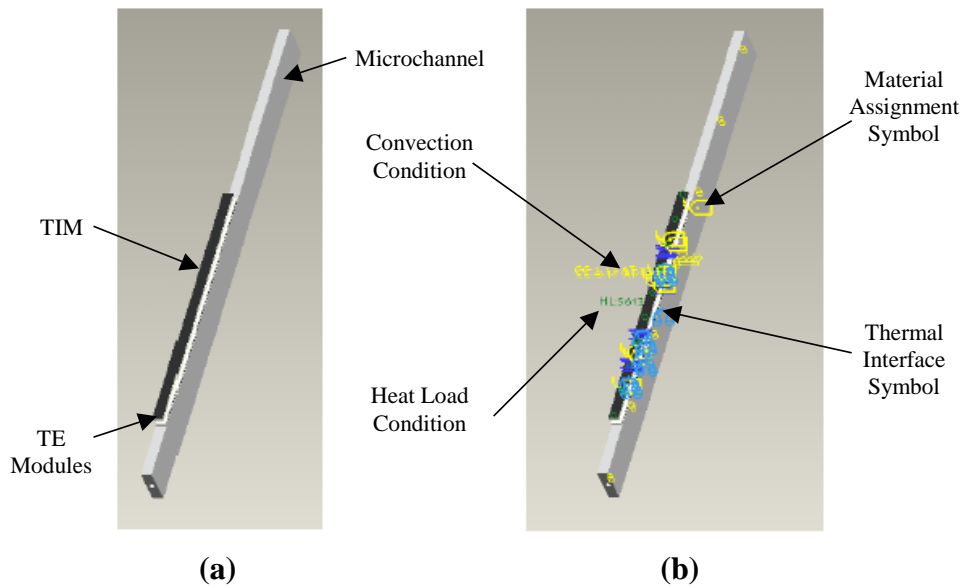


Figure 17: Simulated portion of the test section with all (a) parts labeled and (b) thermal boundary conditions labeled.

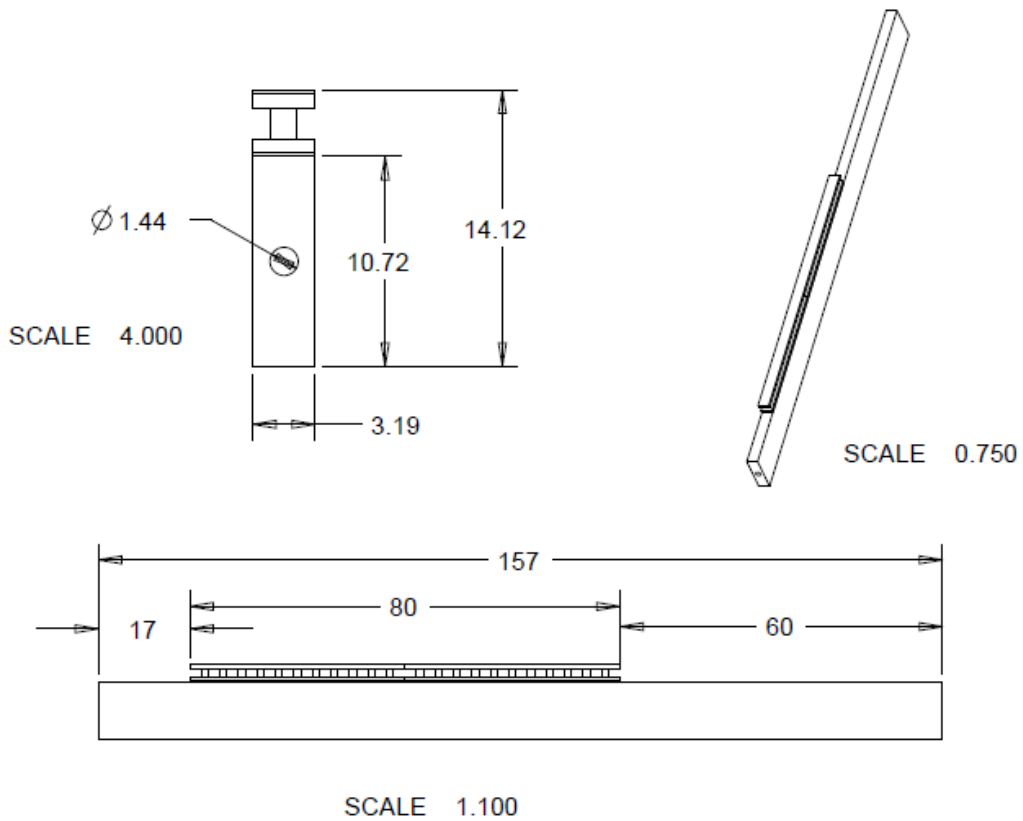


Figure 18: Engineering drawings of the simulated portion of the test section. All dimensions are in millimeters.

The finite element analysis (FEA) tools—ProE, Mechanica and computer—used for this study were unable to simulate the entire test section in Figure 9 due to its size and complexity. Therefore, approximately one twelfth of the entire test section was selected and prepared for thermal simulation as seen in Figures 17 and 18. The microchannel heat exchanger in the simulation test section remained 157.0 mm long and 10.72 mm thick with 1.44 mm channel diameter, but was reduced in width to 3.19 mm (diameter + channel spacing=1.44 mm + 1.75 mm) as only one channel could be simulated. The simulated TIM and thermoelectric modules were reduced in size proportionately to the microchannel heat exchanger. Material assignments of the TIM, microchannel and TE plates were set to the abovementioned respective thermophysical properties as that of the practical materials used to make these components. Since the exact material composition of the TE semiconductor elements was unknown, the TE leg structure material was taken to be pure Bismuth Telluride with thermal conductivity of 3 W/m-K, density of 7.73 g/cm³ and specific heat capacity of 16 m²/s²-K. The headers, gaskets and compressive wooden blocks shown in Figure 9 did not appear in the simulation test section because their roles were mainly in the area of mechanical, as opposed to thermal, interfacing; furthermore, these components were thermal insulators, so, the surfaces that they touched were simply set to adiabatic in Mechanica. All surfaces that were directly insulated with the yellow sponge insulation shown in Figure 9 were also set to adiabatic in preparation for simulation. The partial or entire surfaces of the TIM sheets, TE modules and microchannel that were mated together in ProE were set to ideal, zero-roughness

thermally interfaced surfaces in Mechanica. The HM6800 heater shown in Figure 9 was replaced by its thermal function in Figure 17—providing the uniform heat flux/load over the entire TIM surface above the thermoelectric modules. Since liquid flow was not a programmable feature in Mechanica, the flowing coolant with prescribed inlet temperature of 12 °C was approximated by the convection condition on the ‘wetted surface’ of the microchannel as shown in Figure 17.

It is worthy to note that the FEA simulation was performed after obtaining the experimental results of this project. A total of 162 distinct simulation test runs were conducted, that is, one comparable counterpart to each of the 162 experimental test runs. Each simulation run ran a distinct pair of heat load and convection condition based on practical heater settings and experimentally obtained coolant bulk temperature and mean heat transfer coefficient. The heat load in each simulation run was set as per the abovementioned dimensional differences between the experimental and simulation test sections to 3.19/40 times that of the heat flux value set in the corresponding experimental run. The convection condition on the wetted surface in each simulation run was determined by the bulk coolant temperature and mean heat transfer coefficient values that were obtained from the corresponding experimental run. Each simulation run provided the average of the 2 steady-state temperature readings corresponding to the average of the practical readings from the 2 thermocouples shown placed on the top surface of the microchannel in Step 1 of Figure 9. These simulated microchannel surface temperatures were compared to their experimental

counterparts in an attempt to better understand the nature of heat dissipation by the relevant microchannel heat exchanger. This simulation was hypothesized to be particularly useful in gaining insight as to the relatively unpredictable 3-dimensional conjugate heat transfer effects, including axial conduction, that clearly played a significant role in the overall performance of the relevant microchannel-thermoelectric power generator as seen in the experimental results. A comparison between the simulation and experimental results can be found at the end of Chapter 4 of this thesis.

Chapter 4: Results and Analysis

This chapter provides the detailed results and comparative analysis of the relevant experimentation that was conducted using the test rig and experimental procedure discussed in Chapter 3. Hopefully, the present results and analysis suffice in providing readers with a comprehensive understanding of and appreciation for the overall performance of the thematic Microchannel-Thermoelectric Power Generator with water and alumina-in-water nanofluid coolants. The analytical discussions of this chapter cover the pertinent performance aspects of pressure drop, cooling performance and power generation in terms of the scaling effects mentioned in Chapter 2. Notably as hypothesized in Section 3.4, the coolant temperature rose by 2.6 °C or less from the microchannel inlet to the outlet in all 162 test runs, clearly rendering the scaling effect of temperature dependent coolant properties negligible. Section 4.1 will begin this chapter by analyzing the results of the pressure drop across the microchannel heat exchanger in order to verify the laminar flow assumption and to achieve an understanding of the nature of some of the relevant scaling effects before proceeding to tackle the more complicated performance aspect of microchannel heat transfer. Then, Section 4.2 will present a Brinkman number-based analysis in order to make certain that the coolant flows were indeed fully laminar and that viscous heating effects were insignificant throughout the experimentation. Next, Section 4.3 will assess the overall cooling performance of microchannel heat exchanger by comparison of experimental data with conventional correlations while considering the

complexities of 3D conjugate heat transfer and entrance effects along with rough surface-induced hydrophobic slip. Section 4.4 will sum up the documentation of the experimental findings by discussing the maximum power generation possible from the relevant voltage data from the thermoelectric modules under varying test conditions. Finally, Section 4.5 will conclude this chapter with a brief comparative analysis between the experimental results and those obtained via the computer simulation described in Section 3.5.

4.1: Pressure Drop Results and Analysis

The pressure drop across the microchannel exhibited different, interesting flow rate-based trends for each coolant as expounded upon in this section. Before discussion can begin, it is prudent to provide the experimental coolant (diameter-based) Reynolds numbers corresponding to the 6 relevant flow rates—this information can be found in Table 3 below. Notably, Reynolds numbers did not vary with heater setting as coolant temperature did not directly affect Re , nor were the relevant thermophysical properties varying with coolant temperature as mentioned above.

Table 3: Experimental Water, NF1 and NF2 Re_D values at the 6 flow rates.

Parameter Flow Rate (LPM)	Water Re_D	NF1 Re_D	NF2 Re_D
1.53	1789	1774	1472
1.36	1586	1573	1305
1.13	1323	1312	1089
0.99	1159	1149	954
0.78	913	906	751
0.56	659	653	542

From Table 3, it can be said with confidence that all Reynolds number flows tested were well within the bounds of the laminar flow regime as they were all $Re_D < 2000$. With laminar flow all but confirmed, the pressure drop discussion at hand will now begin with the graphical presentation of the experimental pressure drop and consequential pumping power excess data against flow rate given in Figures 19 and 20, respectively.

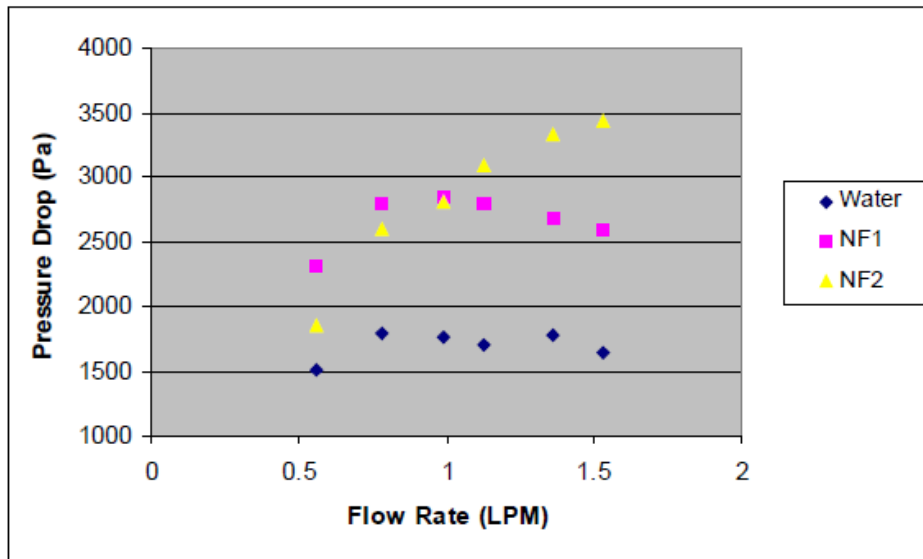


Figure 19: Experimental pressure drop vs. flow rate.

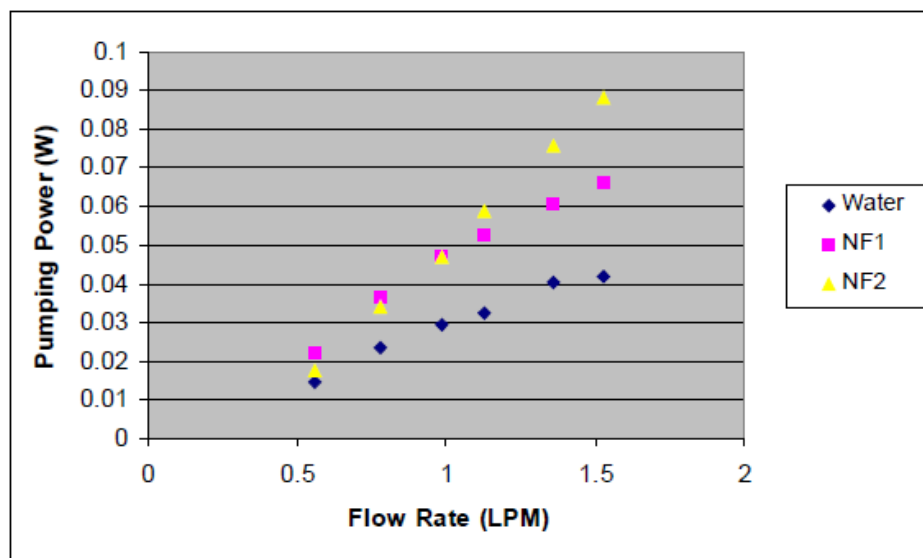


Figure 20: Excess pumping power vs. flow rate.

One interesting difference immediately noted from Figure 19 is that the pressure drop of NF2 monotonically increased with flow rate, however, the corresponding pressure drop values for water and NF1 seemed at first to rise with flow rate but then start to slowly fall with it. This trend for NF2 strongly suggests that for all flow rates (and thus Re) tested, the NF2 flow regime remained fully laminar and free of most unconventional microchannel scaling effects, including velocity slip at the microchannel walls. In contradiction, the rise-and-fall pressure drop trends of water and NF1 suggest that the flow of these coolants remained quite laminar until flow rate was increased to about 1 LPM, whereupon the flow either transitioned towards turbulence or experienced some ‘anomaly’ such as hydrophobic slip. The review papers of Sobhan et al. [21] and Rosa et al. [22] state that most researchers have come to agree that flow transition does not occur more easily ($Re < 2000$) than in conventional channels in microchannels with diameters > 0.200 mm; and since all present experiments were conducted using channels of 1.44 mm diameter, it can be said with confidence that the decline in pressure drop with flow rate for NF1 and water is due not to transition, but rather to slip flow as in the work of El-Genk et al. [30]. The nearly constant rate of increase of NF2 in Figure 20 and the decrease of this rate of water and NF1 at about 1 LPM reaffirm the abovementioned indications of NF2’s monotonic increase and water and NF1’s trends from Figure 19. In addition, Figure 20 clearly shows water to be the most easily pumped coolant through the microchannel, whereas NF1 and NF2 require notably higher pumping powers. The argument of this section will continue on to explain this phenomenon.

Since the microchannel walls were intentionally designed to be rough and hydrophobic to achieve pressure drop reductions via slip flow as mentioned in Chapter 3, this part of the analysis goes on to explore possible velocity slip conditions appearing in the test runs of the relevant experimentation that may explain the pressure drop variation trends seen in Figure 19. Next, Table 4 provides the shear rates and slip lengths at various flow rates for water, NF1 and NF2.

Table 4: Coolant shear rates and slip lengths at the 6 flow rates.

Parameter Flow Rate (LPM)	All coolants shear rate (s^{-1})	Water slip length (μm)	NF1 slip length (μm)	NF2 slip length (μm)
1.53	7260	185	53	32
1.36	6438	119	19	14
1.13	5373	80	-	-
0.99	4705	40	-	-
0.78	3707	-	-	-
0.56	2675	-	-	-

Note: slip length was estimated from Equation 3b of [30].

Since actual experimental slip lengths could not be observed or measured, Equation 3b of El-Genk et al. [30] was invoked to make the estimations given in Table 4, above. El-Genk et al. [30] took the approach of solving the steady state Navier-Stokes momentum balance equation subject to the (slip) boundary condition that the fluid velocity at the channel wall is not zero, but proportional to the shear stress. From this solution, the fully developed, slip radial velocity profile was derived. This led to their Equation 3b—the following expression of average flow velocity in the microchannel—from which slip length β could be obtained if all other relevant variables are known:

Equation 5:

$$\bar{v}_{z,t} = \frac{D^2 \Delta P}{32 \bar{\mu} L} (1 + 8(\beta/D))$$

It is prudent to recall from Chapter 2 the almost-unanimous conclusion of several leading microchannel researchers that the Navier-Stokes relationships remain valid and can thus be relied upon, with appropriate boundary conditions as El-Genk et al. have set, to derive expressions for flows in microchannels. Therefore, it can be said with confidence that the slip lengths obtained from Equation 5 are reasonable estimates of experimental slip lengths.

As mentioned in Section 2.3.1, velocity slip at the microchannel walls typically occurs under highly pressurized flow conditions with shear rates greater than $10,000 \text{ s}^{-1}$, or when the walls are highly hydrophobic. In Table 4, it is apparent that all shear rates were well-below $10,000 \text{ s}^{-1}$, meaning all velocity slippage occurring in the relevant experimentation was primarily caused by the hydrophobicity of the thin passivated alumina layer on the wetted surfaces of the channel walls. In other words, rough-surface hydrophobic channel walls encouraged slip at lower shear rates and, thus, pressure drop reduction, as with Davies et al. [31] and Chakraborty et al. [32]—verifying the hypothesis made in Section 3.1. A noteworthy point is that, according to Figure 19, the pressure drop of water began to decrease at 0.99 LPM—the same flow rate around which slip length started to become significant ($\sim 40 \text{ mm}$ as per Table 4)—and continued decreasing with flow rate, while slip length continued to increase.

In order to better understand the nature of the evident slip flow and the overall pressure drop trends of the relevant experimentation, the remainder of this section will discuss the pressure drop in terms of its non-dimensional counterpart of Darcy Friction Factor. The experimental friction factors of water, NF1 and NF2 are presented, against Reynolds number, with their respective power law best-fit trendlines in Figure 21.

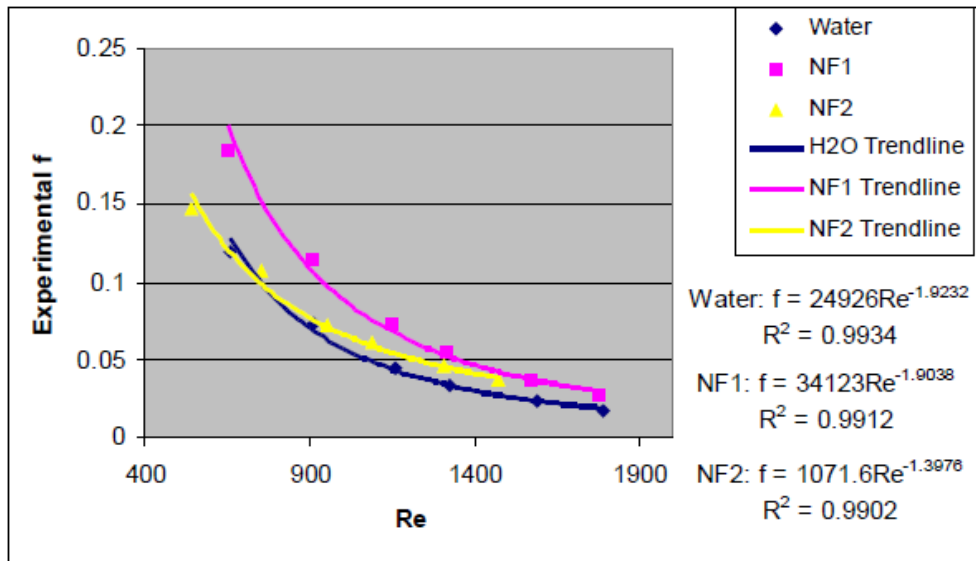
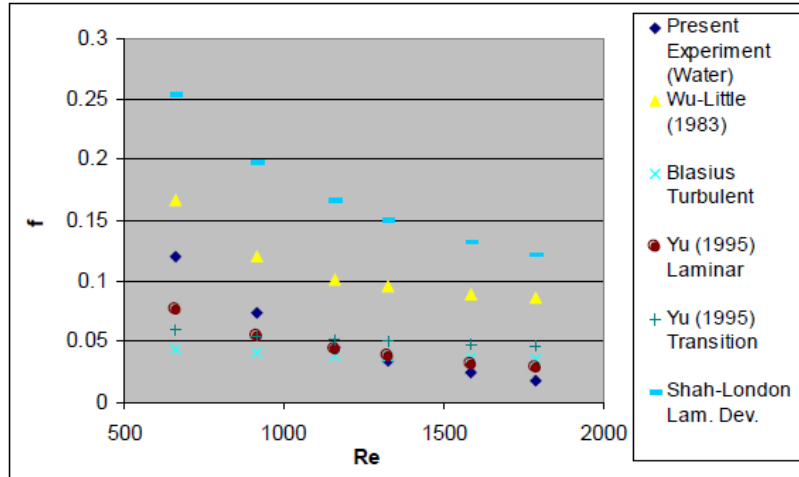


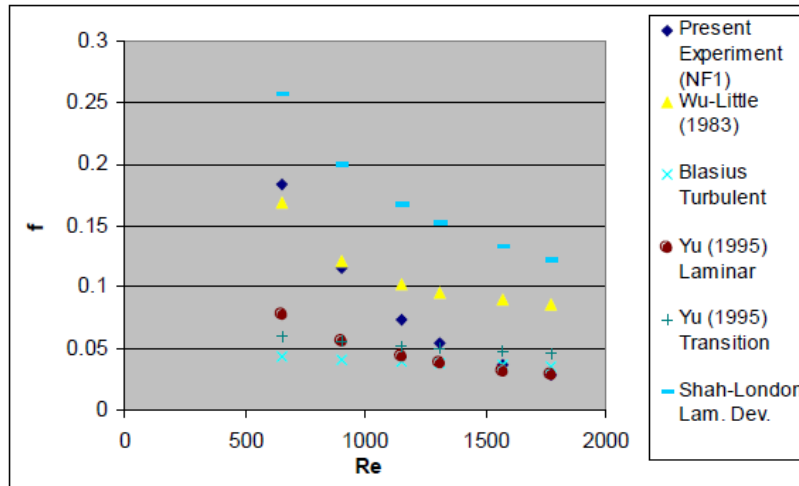
Figure 21: Experimental friction factors vs. Reynolds number.

The power laws of Figure 21 further support the abovementioned indications of varying slip flow effects as the experimental friction factors of water, NF1 and NF2 were found to be directly proportional to $Re^{-1.9232}$, $Re^{-1.9038}$ and $Re^{-1.3976}$, respectively, instead of Re^{-1} as in no-slip laminar flow theory. Particularly, water and NF1 friction factors deviated far more from no-slip laminar theory than the NF2 friction factors, which was made clear by their more negative Re exponents of ~ -1.9 as compared to the less deviant NF2 counterpart of ~ -1.4 —another conclusive analytical observation that corroborates the pressure drop trend

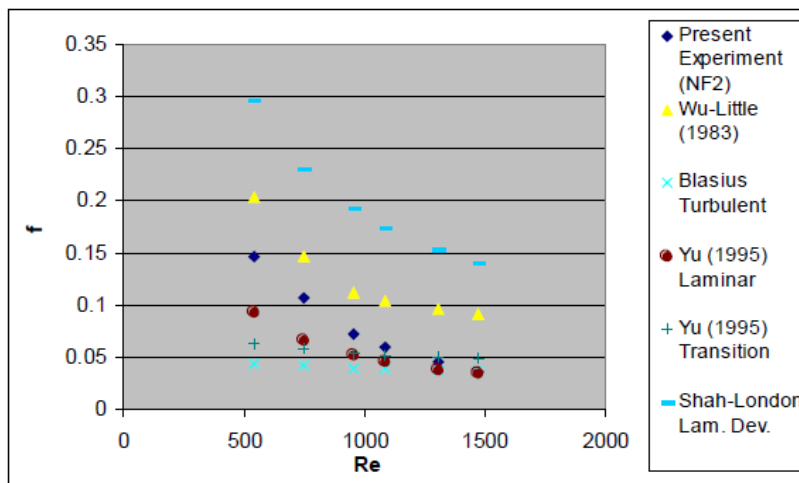
differences pointed in Figure 19 and accounts them to slip flow effects when considered along with the estimated the slip lengths given in Table 4. At this point, it has become adequately clear that rough-surface hydrophobic slip flow effects were present in the relevant experimentation and varied with coolant type and flow rate/Reynolds number. Therefore, it is now prudent to check for and explain the naturally competing effect of surface roughness that was expected to coexist with hydrophobic slip and contrarily serve to raise friction factors above those predicted by the no-slip laminar theory. On this note, Figure 22 graphically compares experimental friction factors with corresponding values predicted by correlations, which had been especially derived or simply often considered in general by past researchers for microchannel friction factor prediction.



(a)



(b)



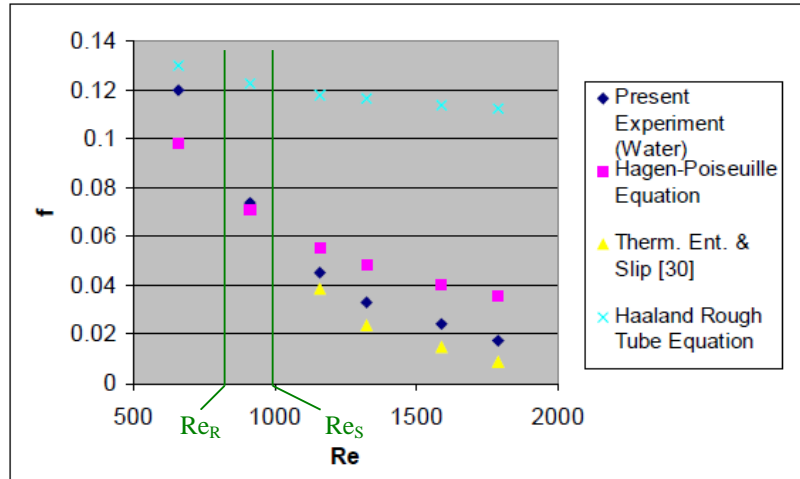
(c)

Figure 22: Experimental friction factors of (a) water, (b) NF1 and (c) NF2, compared with those predicted by microchannel correlations [21, 22].

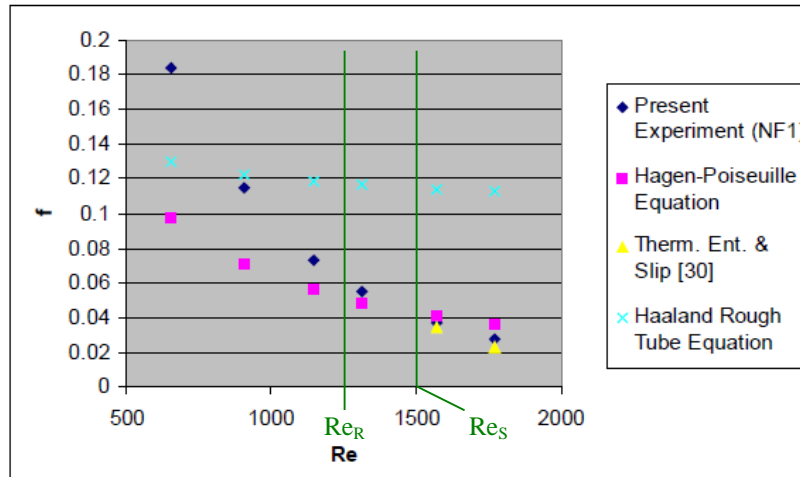
First, it is clear from Figure 22 that turbulent and transition flow regime friction factor correlations do not apply because of vastly differing trends from those of the experimental friction factors, which were adequately determined to be in the laminar flow regime. Next, the Shah-London laminar correlation, which considers hydrodynamic flow development was found to be very inaccurate and an over predictor of the experimental friction factors of all 3 relevant coolants due to its inherent inaccuracy for low values (≤ 0.2 —includes all present test runs) of the non-dimensional hydrodynamic entrance length parameter L^+ , where L^+ is the microchannel length-to-diameter ratio divided by Reynolds number ($L/D \cdot Re_D$) [28]. Furthermore, the Blasius and Shah-London equations proved to be inadequate predictors due to their validities strongly relying on the assumptions of smooth channel walls and no-slip, both of which were diametrically opposite to the relevant experimentation conditions. The 1983 Wu-Little correlation also over-predicted friction factor in all relevant cases as is seen above in Figure 22. The reason for this over-prediction was found recently by Tang et al. to be as follows: although Wu et al. assumed complete smoothness of their microchannel walls when establishing their correlation, their testing apparatus was later closely examining to reveal that they had neglected an extreme relative roughness of 20-30% [43]. The laminar Yu correlation (modified Hagen-Poiseuille equation), although sometimes coincidentally accurate as seen for all coolants at higher Reynolds numbers in Figure 22, is not generally reliable because it was derived as a predictor of liquid as well as gas flow in microchannels, leading to error from irrelevant compression and rarefaction considerations. The above correlations'

failures to accurately predict the experimental friction factors corroborates the widely believed conclusions of Sobhan et al. and Rosa et al. that there currently exists no single correlation that can be applied generally to all microchannel friction factor predictions [21, 22]. The above microchannel correlations along with others of their time are applicable in a very narrow range of case-based experiments [21, 22]; therefore, the present experiment would likely be best understood by taking a ‘custom approach’ as recommended by Rosa et al. [22].

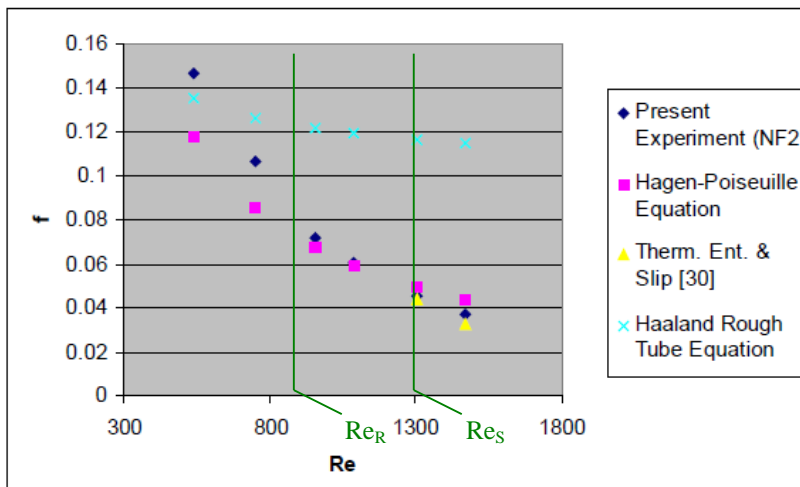
The custom approach taken in this pressure drop analysis was to finally compare the experimental friction factors shown in Figures 21 and 22 with the following three conventional friction factor correlations in order to explain the relevant competing effects of surface roughness and hydrophobic slip: Haaland equation, Hagen-Poiseuille equation and the slip friction factor correlation (Equation 10) of El-Genk et al. [30]. The Haaland equation considers channel relative roughness, but not slip [44]; conversely, the El-Genk equation, which is a modified Hagen-Poiseuille equation, considers slip (and thermal entrance) but not surface roughness; and the Hagen-Poiseuille equation considers neither roughness nor slip but is useful in determining under which conditions the two competing effects essentially cancel each other out. The friction factor predictions by these three correlations were graphically compared with experimental friction factors in Figure 23.



(a)



(b)



(c)

Figure 23: Experimental friction factors of (a) water, (b) NF1 and (c) NF2, compared with those predicted by conventional correlations [30, 44].

Just as with Figure 22, it is immediately apparent that no individual correlation of Figure 23 succeeded in predicting all of the experimental friction factors either. However, Figure 23 and the correlations therein, when considered together, were instrumental in determining the natures of the competing slip and roughness effects on the relevant friction factors. The abovementioned custom approach to the relevant explanation was taken as follows (in reference to each graph of Figure 23): when the experimental friction factors were observed to significantly exceed (by at least ~10%) the Hagen-Poiseuille friction factors it was evident that channel roughness effects were overtaking slip effects; when the experimental friction factors were observed to be significantly lower (by at least ~10%) than the Hagen-Poiseuille friction factors it was reasonably accepted that slip effects were overtaking roughness effects; and when the experimental friction factors were observed to be about the same (within ~10%) as the Hagen-Poiseuille friction factors it was clear that the roughness effects and slip effects were canceling each other out to match with the predictions of conventional laminar flow theory. In a similar fashion to the Celata [27] argument pertaining to Figure 5 of Chapter 2, for each coolant, regions of slip predominance, roughness predominance, and balance between the two competing effects are shown divided the Reynolds numbers Re_S and Re_R on Figure 23 above. On each graph of Figure 23, the slip predominance region is comprised of all $Re > Re_S$, the roughness predominance region is comprised of all $Re < Re_R$, and the balanced region is comprised of all $Re_S > Re > Re_R$. It is worthy to note that Re_S values for water, NF1 and NF2 were 1000, 1500 and 1300, respectively; and Re_R values for water, NF1

and NF2 were 800, 1250 and 900, respectively. Furthermore, the experimental friction factors in the slip predominance region were considered to be completely unaffected by roughness effects if they were very close (within ~5% of) to the corresponding El-Genk friction factors, but would become increasingly influenced by roughness effects the more they departed from El-Genk and went towards Hagen-Poiseuille friction factors. Similarly, the experimental friction factors in the roughness predominance region were considered to be completely unaffected by slip effects if they were close (within ~10% of) to the corresponding Haaland friction factors, but would become increasingly influenced by slip effects the more they departed from Haaland and went towards Hagen-Poiseuille friction factors. Notably, the experimental friction factors of NF1 at $Re=653$ and NF2 at $Re=542$ considerably surpass even the corresponding rough tube Haaland friction factors—these extreme, or ‘outlying,’ experimental findings were largely attributed to a combination of the following reasons: the Haaland equation does not consider thermal entrance effects and is an approximation equation with margin of error up to 20% in some cases; and the 10% relative roughness of the microchannels had was designed with tolerance of 1%. Although there is a slip predominance region determined for NF2, it is clear from Figure 23 (c) that the effects of slip on the higher- Re NF2 friction factors were relatively weak, hence, the monotonic increase of NF2 pressure drop with flow rate shown on Figure 19. Again referring to Figure 19, the small but sudden rise in the water friction factor from that at 1.13 LPM to that at 1.36 LPM is attributed to the ~0.119 mm slip length (and equally thick presumed nanobubble layer) nearly

catching up in magnitude to the ~ 0.144 mm surface roughness and overcoming almost all interfacial flow resistance, as Davies et al. [31] put it, to somewhat lengthen the hydrodynamic entrance leading to slight, sudden and temporary increase in pressure drop instead of simply following the local trend.

The three abovementioned regions of slip predominance, roughness predominance and balanced conventional laminar flow established in the pressure drop/friction factor analysis was applicable to and had provided invaluable insight throughout the remainder of this chapter, especially to the area of the relatively complicated microchannel heat transfer analysis. In conclusion of this section, it is noteworthy that the present analysis strongly agrees with Sobhan et al. [21] and Rosa et al. [22] that conventional correlations are fairly useful in post-experimentation friction factor analysis, however, they are not *generally* reliable predictors before the fact. Therefore, microchannel researchers are encouraged to execute sophisticated flow simulations for dependable predictions of experimental pressure drop.

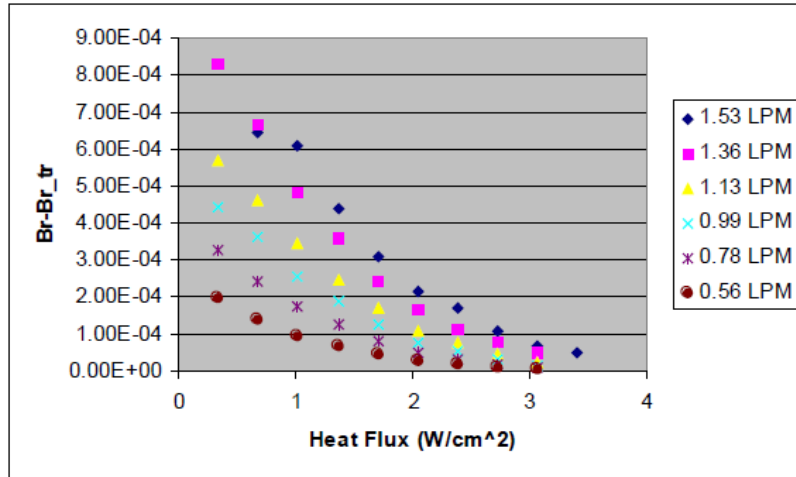
4.2: Brinkman Number-Based Analysis

The Brinkman number (Br)—a non-dimensional parameter pertaining to heat conduction from a wall to a flowing viscous fluid—has become a correlative asset to laminar, single-phase forced convective heat transfer in microchannels with the CWHF boundary condition (see Section 2.3.1). This section will invoke the Brinkman number in order to reaffirm the flow regime in each test run to be fully

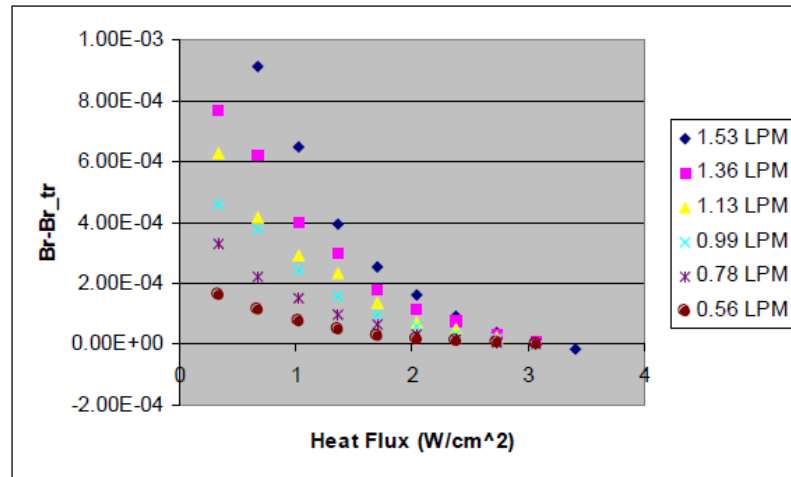
laminar as established in the previous section, and to assess the significance of viscous heating effects throughout the relevant experimentation as well.

4.2.1: Flow Regime Verification

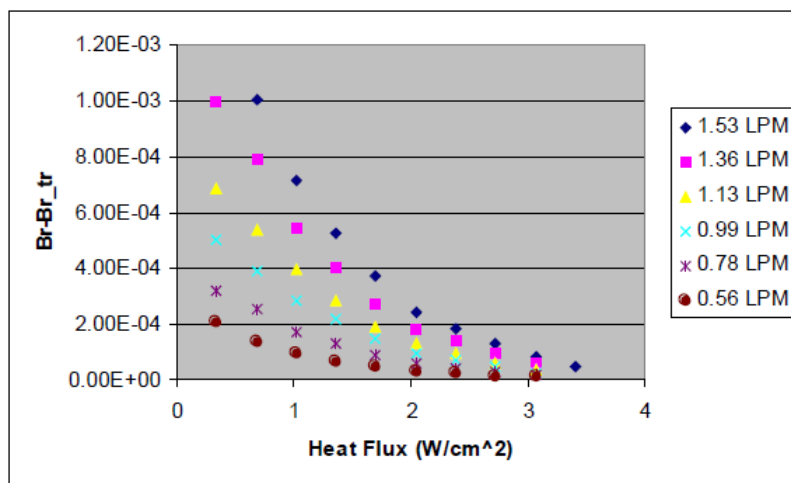
Although the Reynolds number-based pressure drop analysis of Section 4.1 adequately established all relevant flows to be fully laminar (with abovementioned slip and roughness effects), the Brinkman number-based analysis will be presented below simply to serve as a conservative ‘double check’ on the flow regime. The tool used for this analysis was the $\log(\text{Br}_{tr})=2.00\log(\text{Re})-10.34$ locus derived by Tso and Mahulikar [26] (see Section 2.3.1), in which, Br_{tr} is such that: flow is fully laminar if $\text{Br}-\text{Br}_{tr}>0$, else, it is in transition towards turbulence. Notably, Br values pertaining to each test run were calculated using experimentally known velocities, viscosities, thermal conductivities and bulk temperatures of the coolant, and microchannel wall temperatures (averaged over the heated length of 80 mm); and Br_{tr} was determined using the above Tso-Mahulikar locus and experimental Re values shown in Table 3. Figure 24 graphically presents $\text{Br}-\text{Br}_{tr}$ values of each test run.



(a)



(b)



(c)

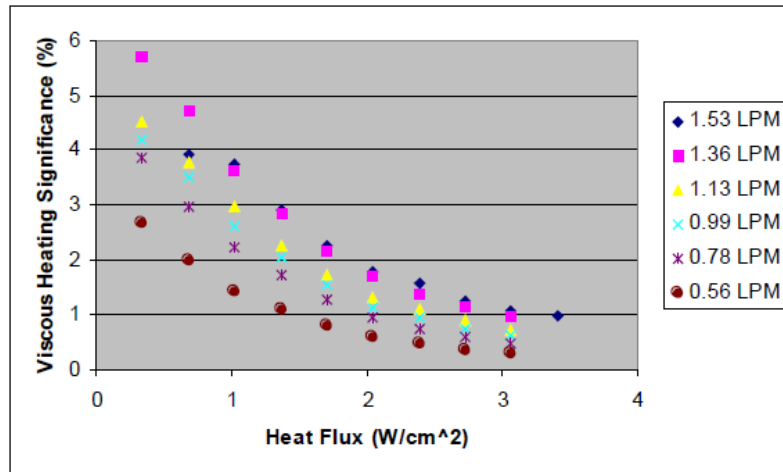
Figure 24: Experimental Br-Br_{tr} values of (a) water, (b) NF1 and (c) NF2.

It is immediately evident from Figure 24 that essentially all $Br-Br_{tr}$ values were positive, thus, reinforcing the prior establishment of the flow regime in each test run to be fully laminar. Although the Tso-Mahulikar locus was a relatively straightforward flow regime-checking tool, a brief commentary will be given on the general trends seen in Figure 24. On all coolant graphs, for any fixed heat flux (heater setting), the $Br-Br_{tr}$ values were found to decrease towards zero, or the transitional flow regime, with decreasing flow rate. The reason for this trend is that in going from higher to lower flow rates/Reynolds numbers, coolant velocity decreased proportionately, which lowered Br much more than Br_{tr} as Br was directly proportional to the square of velocity and Br_{tr} had a much weaker dependence on velocity. Also on all coolant graphs, for any fixed flow rate, the $Br-Br_{tr}$ values were found to decrease towards zero, or the transitional flow regime, with increasing heat flux. The reason for this trend is that in going from lower to higher heat flux, the gap between the microchannel wall temperature and coolant bulk temperature widened, which proportionately reduced Br while Br_{tr} remained unchanged as it did not depend on the heat flux/temperature difference. Though 4 of the NF2 $Br-Br_{tr}$ values presented in Figure 24 were very slightly negative, it was not so because their corresponding flows were in the transitional flow regime, rather, it was due to the abovementioned laminar-flow surface roughness effects, which were said (following Figures 19 and 20) to somewhat mimic typical transitional flow behavior. It is concluded in this thesis section that Tso and Mahulikar's [26] Brinkman number-based locus is an instrumental flow

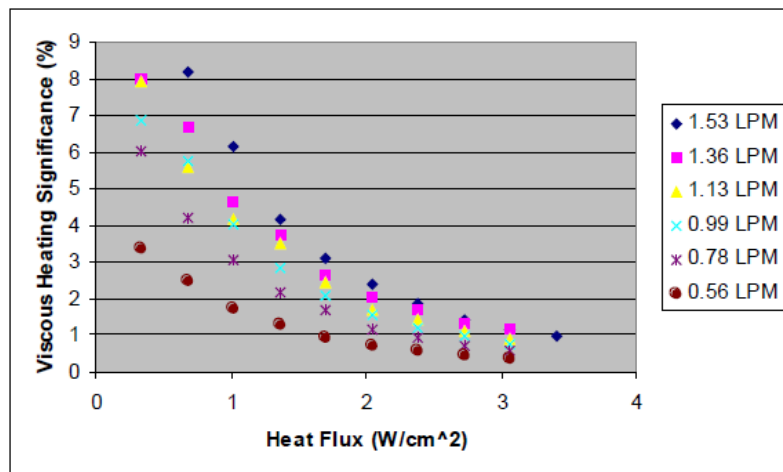
regime assessment tool and should be incorporated into the overall flow regime analysis in all microchannel applications.

4.2.2: Viscous Heating Assessment

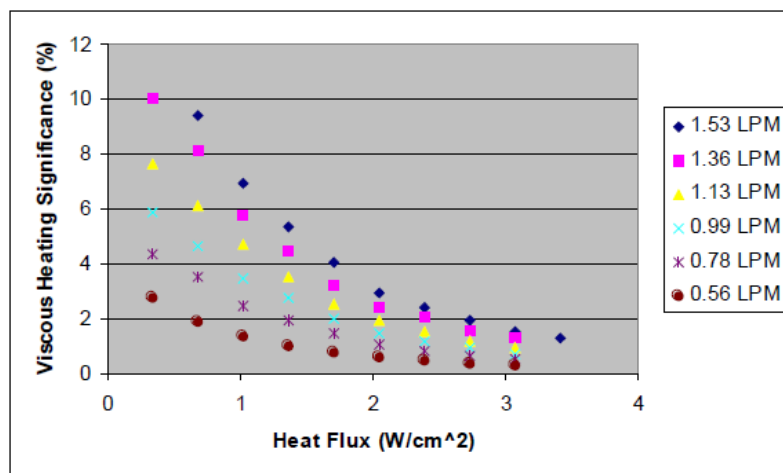
This section is dedicated to verifying Assumption 7 of Section 3.4 that viscous heating effects were insignificant throughout all experimentation of this project. It is prudent to begin by noting that all experimental Brinkman numbers were in the range of $1.87 \cdot 10^{-5}$ to $1.11 \cdot 10^{-3}$. Since all experimental $Br \ll 1$, the direct effect, or ‘primary effect’ as Tso and Mahulikar [26] put it (see Section 2.3.1 for summary of [26]), of viscous heating on (the reduction of) Nusselt numbers was truly insignificant. However, the ‘secondary effect’ mentioned by Tso and Mahulikar could not immediately be ruled out because experimental Brinkman numbers were all well-above 10^{-8} . Therefore, the remainder of this section will focus on evaluating the significance of the secondary viscous heating effect on the relevant experimental heat transfer. Morini’s 2D steady, laminar, fully developed flow model with constant thermophysical properties (Equation 14 in Rosa et al. [22]) was used to gain theoretical insight into the degree of the relevant viscous heating significance. Figure 25 graphically presents the viscous heating significance, that is, the ratio between the temperature rise due to viscosity and the temperature rise due to supplied heat flux at the microchannel wall, estimated by the Morini model for each test run.



(a)



(b)



(c)

Figure 25: Viscous heating significance in all (a) water, (b) NF1 and (c) NF2 test runs.

As can be seen from Figure 25, the viscous heating significance in all test runs was estimated by the Morini model to be less than or equal to 10%, thus, adequately verifying Assumption 7 of Section 3.4. Furthermore, it must be made clear that the Morini model was hypothesized to at least slightly over-predict viscous heating significance in experimentation due to the fact that this model does not consider slip flow effects. As Davies et al. [31] and Chakraborty et al. [32] had found (see Section 2.3.1 for summary), the slip-associated nanobubble layer and resulting reduction in interfacial resistance to flow greatly reduced the significance of viscous heating effects such that most existing flow models often vastly over-predicted the actual viscous heating significance. In fact, for zero applied heat flux, at each of the 6 relevant flow rates (0.56-1.53 LPM) each coolant was pumped through the microchannel at an inlet temperature of 12.0 °C and was found each time to yield an outlet temperature of 12.0 °C. Since no inlet-to-outlet coolant temperature-rise was observed for any flow rate, it is clear from this practical verification that actual viscous heating significance throughout the 162 test runs must have been quite negligible (less than or equal to ~3%), thus, agreeing with the findings of El-Genk et al. [30], Davies et al. [31] and Chakraborty et al. [32] and finalizing the validity of Assumption 7 in Section 3.4. Finally, although the Morini model often overestimates viscous heating significance in experiments with slip flow conditions; this model is still a reasonable tool for assistance in *conservatively* designing microchannels for minimized viscous heating effects.

4.3: Microchannel Heat Transfer Results and Analysis

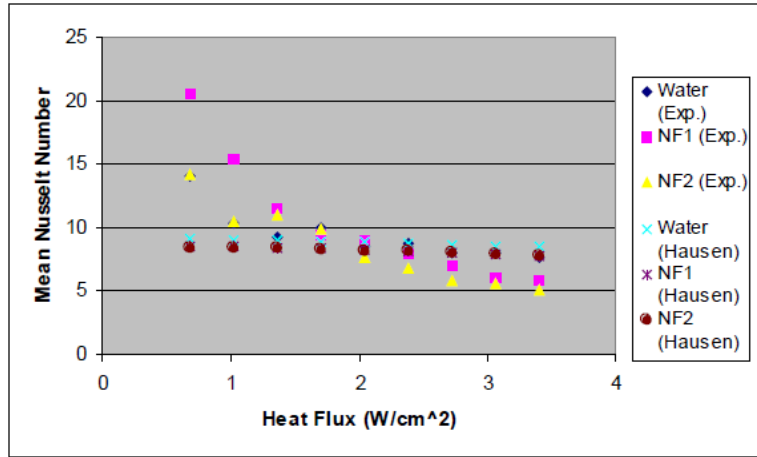
This section will present a detailed analysis of the main focus of this thesis—the evaluation of the heat transfer behavior, or cooling performance, of water, NF1 and NF2 in the relevant microchannel heat exchanger. To reiterate, Figures 4 and 22 have shown specialized microchannel flow and heat transfer equations to have not been generally reliable predictors due to the various previously unconsidered scaling effects that become significant at the micro-scale (see Sections 2.3 and 4.1). Therefore, the present thesis will not present any microchannel Nusselt number correlation comparisons and will only compare experimental Nusselt numbers with those predicted by the Hausen correlation, while accounting for significant scaling effects so as to explain the disagreements observed between theory and experiment—an effective approach as seen in Chapter 2 [22, 27]. As for the pertinent scaling effects, temperature-dependent properties and viscous heating were found to be insignificant, regions of predominance of slip and surface roughness effects were established and explained above, and Sections 4.3.1 and 4.3.2 will proceed to explain the effects of conjugate heat transfer and thermal entrance, along with slip and roughness, on the overall cooling performance being discussed. Then, Section 4.3.3 will sum up how the heat transfer coefficients of water, NF1 and NF2 ‘stacked up’ against one another under the abovementioned varying conditions of flow rate and heat flux/heater setting. Notably, all heat transfer coefficients and Nusselt numbers discussed in this thesis will be *mean* values as opposed to local values. The heat transfer coefficient (h) was computed for each test run as follows: $q = \dot{m}' * c_p * (T_{out} - T_{in}) \rightarrow$

$h=q/(A*(T_{surf.}-T_{bulk}))$, where q is the total heat convectively dissipated by the coolant in the microchannel, m' is the coolant mass flow rate, c_p is the specific heat of the coolant as shown in Table 2, T_{out} and T_{in} are the coolant temperatures at the microchannel outlet and inlet, respectively, A is the total wetted channel surface area of the microchannel heat exchanger, $T_{surf.}$ is the average surface temperature of the heated 3200-mm² area of the microchannel, and T_{bulk} is the coolant bulk temperature (average of T_{out} and T_{in}). Nusselt numbers (Nu) were simply computed as follows: $Nu=h*d/k$, where h is heat transfer coefficient, d is channel diameter (1.44 mm), and k is the thermal conductivity of the coolant as shown in Table 2.

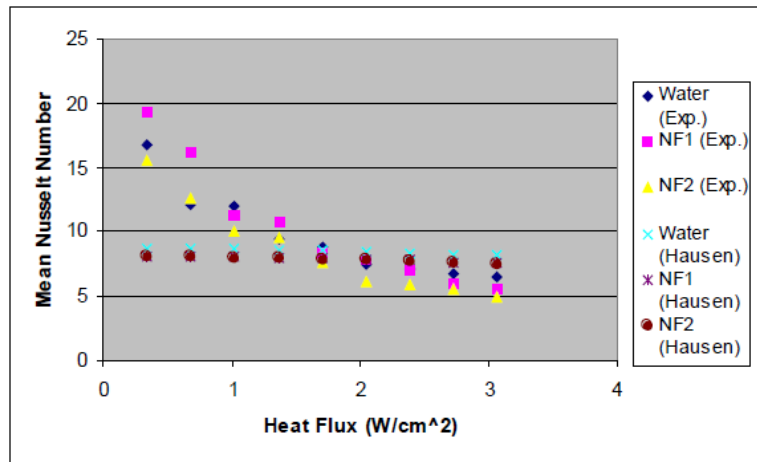
4.3.1: Nusselt Number vs. Heat Flux

Just as Section 4.1 established Reynolds number ranges of slip and roughness predominance, this section will attempt to establish heat flux ranges of 3D conjugate heat transfer predominance and slip/surface roughness effects predominance for each coolant at each flow rate. Before beginning the discussion it is worthy to note that Graetz numbers (Gz) pertaining to all test runs were in the range of 66 to 270 ($Gz>10$), making thermal entrance effects significant throughout the entire relevant experimentation [22, 27]. Since all Graetz numbers were considerably greater than 10 and most experimental Nusselt numbers were greater than the fully developed laminar value of 4.36, it was quite reasonable to invoke the Hausen correlation for prediction and comparative analysis. Figure 26

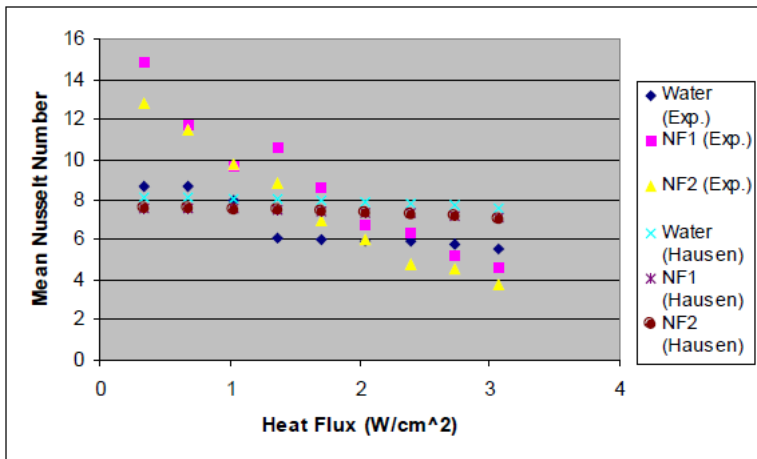
graphically presents the experimental Nusselt numbers with those of the Hausen correlation against applied heat flux for all coolants at each flow rate.



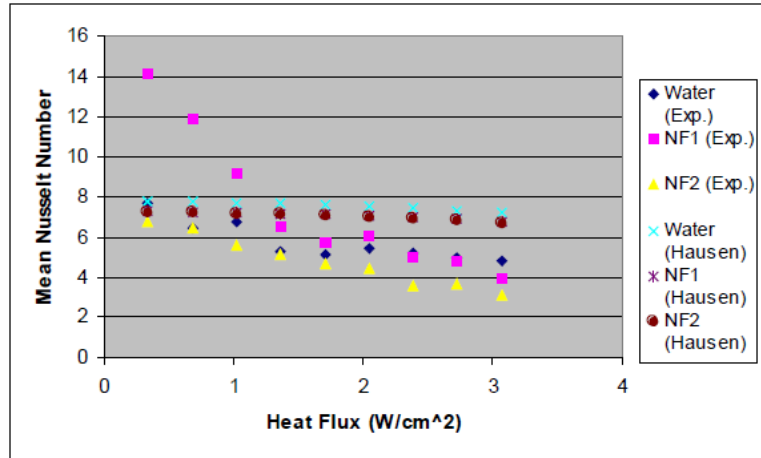
1.53 LPM



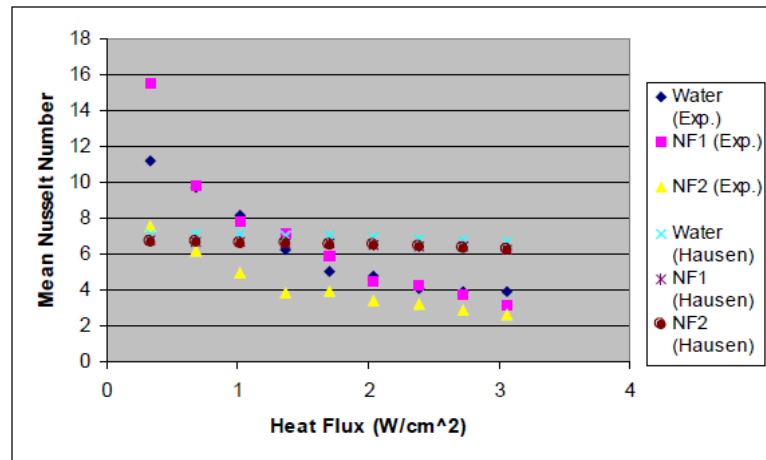
1.36 LPM



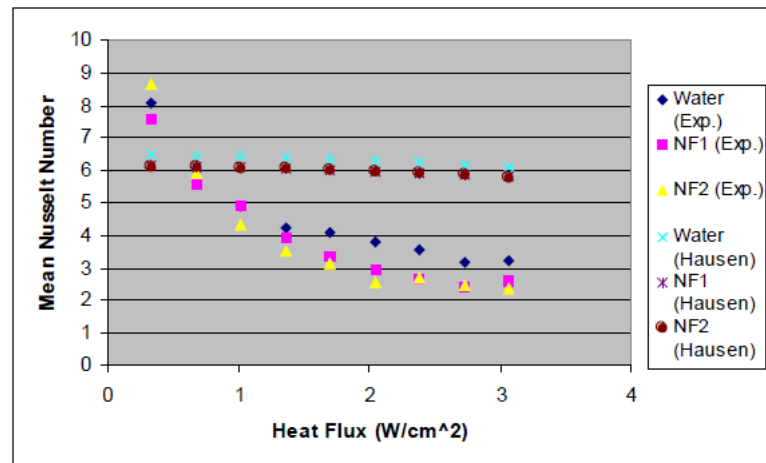
1.13 LPM



0.99 LPM



0.78 LPM



0.56 LPM

Figure 26: Experimental and Hausen Nusselt numbers against applied heat flux at all 6 relevant flow rates.

It is immediately clear from Figure 26 that the Hausen correlation alone could not adequately predict the varying trends of experimental Nusselt numbers as it did not account for slip, surface roughness or conjugate heat transfer effects. At this point, it is necessary to recall that a fair understanding, in terms of flow rate/Reynolds number ranges, of slip and roughness effects was achieved in Section 4.1, and the Hausen correlation accurately accounts for thermal entrance effects, leaving only conjugate heat transfer to be analyzed. Originally, the Maranzana parameter mentioned in Chapter 2 was considered for checking axial conduction significance, however, this criterion was discarded because it is known to be only a rough estimator when dealing with single microchannels and is even less worthwhile when applied to several parallel channels as in the present case [22]. Notably, the following well-established notion by Rosa et al. was accepted and applied to the present analysis: surface roughness effects, though they can markedly raise friction factors, usually only somewhat raise Nusselt numbers [22]. Another notion accepted from the work of the same researchers was that slip flow also must have at least somewhat enhanced convective heat transfer (raised Nusselt numbers) due to the slip length-associated wall velocity rise and the considerable thermal entrance effects present throughout the relevant experimentation [22]. Hence, 3D conjugate heat transfer effects, including axial conduction, were understood by careful inspection of the graphs in Figure 26, by which heat flux ranges of thermal entrance predominance and conjugate heat transfer predominance were established. For each coolant on each flow rate graph in Figure 26, at a given heat flux, when the experimental Nusselt numbers were

observed to be significantly lower (by at least ~10%) than their Hausen counterparts it was reasonably accepted that conjugate heat transfer effects were overtaking the effects of thermal entrance and slip/roughness—conjugate heat transfer predominance; however, when the experimental Nusselt numbers were observed to be within ~10% of their Hausen counterparts it was reasonably accepted that slip/roughness heat transfer enhancement was being cancelled out by Nu-deteriorating conjugate heat transfer effects, leaving the net effect equivalent to only that of thermal entrance on the overall microchannel heat transfer—balanced as per Hausen; on the other hand, when the experimental Nusselt numbers were observed to be significantly higher (by at least ~10%) than their Hausen counterparts it was reasonably accepted that the effects of slip/roughness were overtaking conjugate heat transfer effects—slip/roughness predominance. In a similar fashion to the analysis of Section 4.1, regions of conjugate heat transfer predominance, slip/roughness predominance, and balance between these competing effects (Hausen accuracy region) were divided by the heat flux (HF) values HF_C and $HF_{S/R}$. Specifically, the conjugate heat transfer predominance region is comprised of all $HF > HF_C$, the slip/roughness predominance region is comprised of all $HF < HF_{S/R}$, and the balanced region is comprised of all $HF_C > HF > HF_{S/R}$. HF_C and $HF_{S/R}$ values for each of the 18 coolant-flow rate sets are provided in Table 5 below.

Table 5: HF_C and $HF_{S/R}$ values for Water, NF1 and NF2 at the 6 flow rates.

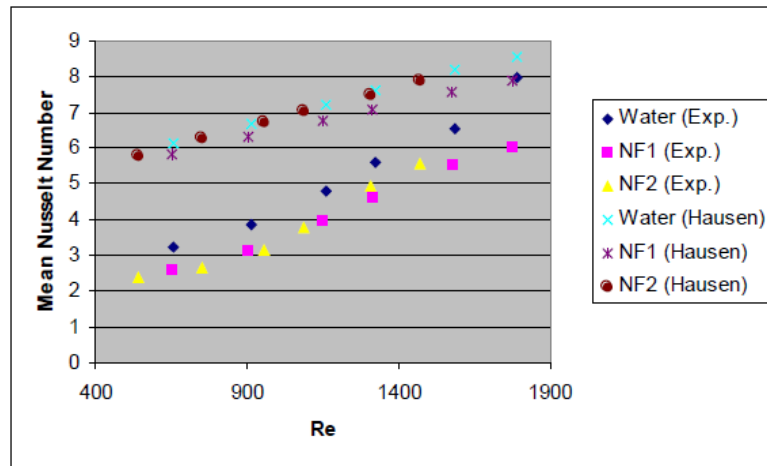
Parameter Flow Rate (LPM)	Water HF_C (W/cm^2)	Water $HF_{S/R}$ (W/cm^2)	NF1 HF_C (W/cm^2)	NF1 $HF_{S/R}$ (W/cm^2)	NF2 HF_C (W/cm^2)	NF2 $HF_{S/R}$ (W/cm^2)
1.53	3.45	0.70	2.65	1.70	2.25	1.85
1.36	1.95	1.30	2.35	1.85	1.80	1.55
1.13	1.15	0.30	2.05	1.75	1.75	1.45
0.99	0.50	0.25	1.35	1.10	0.50	0.25
0.78	1.30	1.05	1.75	1.25	0.35	0.65
0.56	0.70	0.40	0.70	0.45	0.75	0.55

It is evident in Table 5 that there is no easily definable trend of either HF_C or $HF_{S/R}$ variation with flow rate or coolant—strongly supporting the very recent collective conclusion of Rosa et al. [22] and numerous preceding researchers that simultaneously modeling such phenomena as slip, roughness, thermal entrance, conjugate heat transfer is, as yet, extremely difficult. Therefore, Rosa et al. has recommended launching dedicated, highly accurate experimental campaigns in order to collect and graph/tabularize microchannel heat transfer data in terms of significant scaling effects for particular cases of interest—as has been done thus far in the present work in the forms of Figure 26 and Table 5.

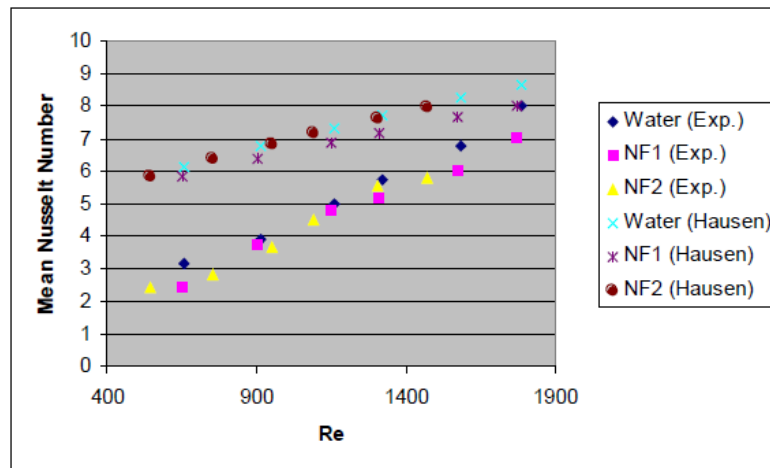
4.3.2: Nusselt Number vs. Reynolds Number

Once again, the Hausen correlation will be invoked to compare with experimental Nusselt numbers in order to establish regions of predominance of conjugate heat transfer and slip/roughness. However, this section will serve to ascertain similar predominance regions in terms of Reynolds numbers instead of heat flux values. Hence, Figure 27 graphically presents the experimental Nusselt numbers with

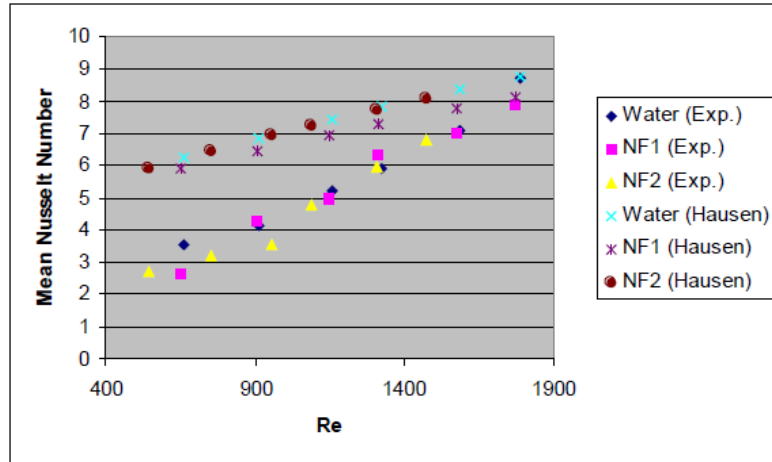
those of the Hausen correlation against Reynolds number for all coolants at each heater setting/heat flux.



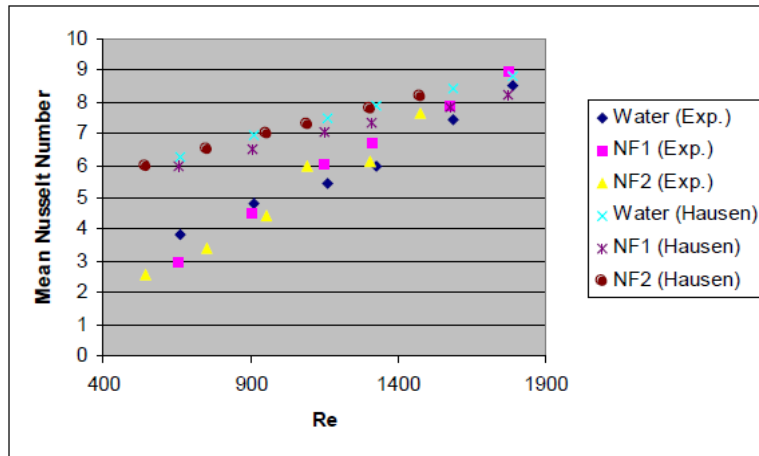
3.069 W/cm^2



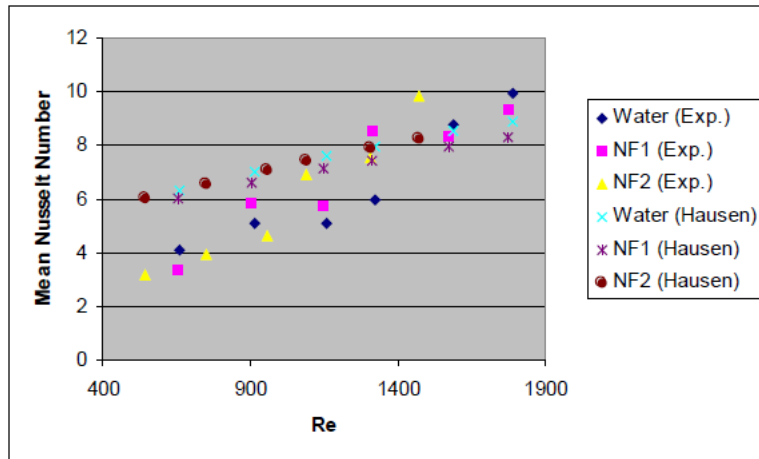
2.728 W/cm^2



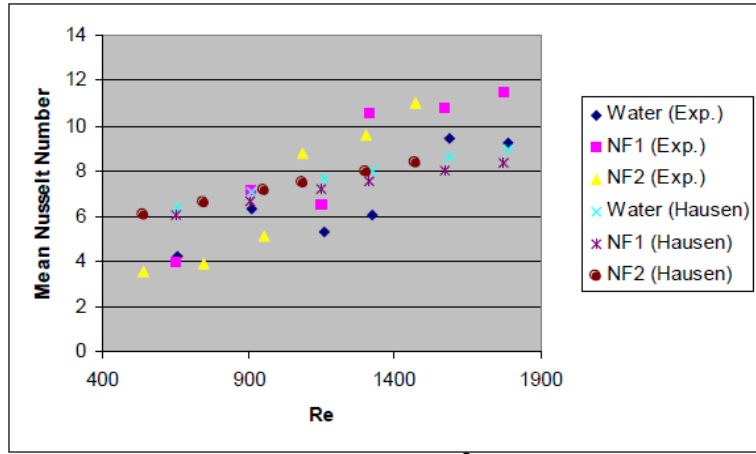
2.387 W/cm²



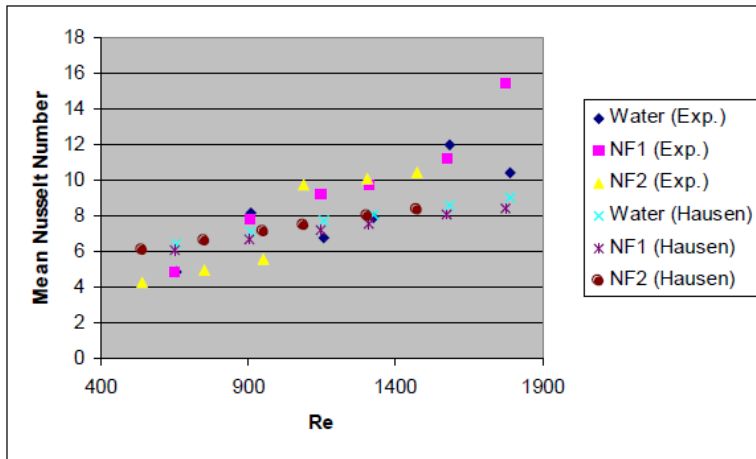
2.046 W/cm²



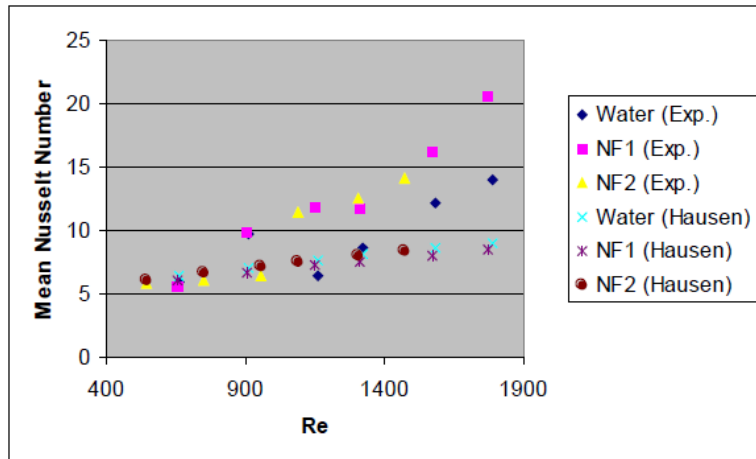
1.705 W/cm²



1.364 W/cm²



1.023 W/cm²



0.682 W/cm²

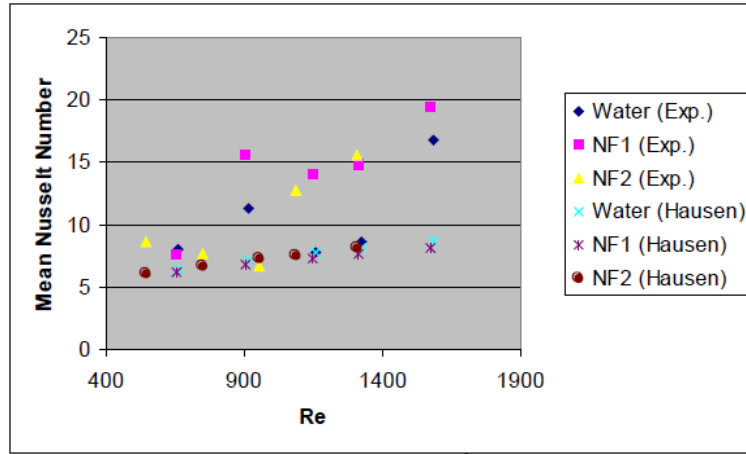


Figure 27: Experimental and Hausen Nusselt numbers against Reynolds numbers at all 9 relevant applied heat flux values.

As with Figure 26, it is similarly clear from Figure 27 that the Hausen correlation did not sufficiently predict the varying trends of experimental Nusselt numbers. Recalling the arguments made in Section 4.3.1, the analysis of this section will proceed in a similar fashion. For each coolant on each heat flux graph in Figure 27, at a given flow rate, when the experimental Nusselt numbers were observed to be significantly lower (by at least ~10%) than their Hausen counterparts it was reasonably accepted that conjugate heat transfer effects were overtaking the effects of thermal entrance and slip/roughness—conjugate heat transfer predominance; however, when the experimental Nusselt numbers were observed to be within ~10% of their Hausen counterparts it was reasonably accepted that slip or roughness heat transfer enhancement was being cancelled out by Nu-deteriorating conjugate heat transfer effects, leaving the net effect equivalent to only that of thermal entrance on the overall microchannel heat transfer—balanced as per Hausen; on the other hand, when the experimental Nusselt numbers were observed to be significantly higher (by at least ~10%) than their Hausen

counterparts it was reasonably accepted that the effects of slip/roughness were overtaking conjugate heat transfer effects—slip/roughness predominance. In a similar fashion to the analysis of Section 4.3.1, regions of conjugate heat transfer predominance, slip/roughness predominance, and balance between these competing effects (Hausen accuracy region) were divided this time by the Reynolds number values Re_C and $Re_{S/R}$. Specifically, the conjugate heat transfer predominance region is comprised of all $Re < Re_C$, the slip/roughness predominance region is comprised of all $Re > Re_{S/R}$, and the balanced region is comprised of all $Re_{S/R} > Re > Re_C$. Re_C and $Re_{S/R}$ values for each of the 27 coolant-heat flux sets are provided in Table 6 below.

Table 6: Re_C and $Re_{S/R}$ values for Water, NF1 and NF2 at the 9 heat fluxes.

Parameter Heat Flux (W/cm ²)	Water Re_C (W/cm ²)	Water $Re_{S/R}$ (W/cm ²)	NF1 Re_C (W/cm ²)	NF1 $Re_{S/R}$ (W/cm ²)	NF2 Re_C (W/cm ²)	NF2 $Re_{S/R}$ (W/cm ²)
3.069	1760	-	1790	-	1500	-
2.728	1750	-	1780	-	1500	-
2.387	1600	-	1590	-	1490	-
2.046	1590	-	1210	-	1450	-
1.705	1500	1800	1200	1790	1050	1390
1.364	1390	1800	840	1240	980	1070
1.023	740	1370	740	880	1000	1030
0.682	620	1370	610	780	-	1020
0.341	-	630	-	630	-	-

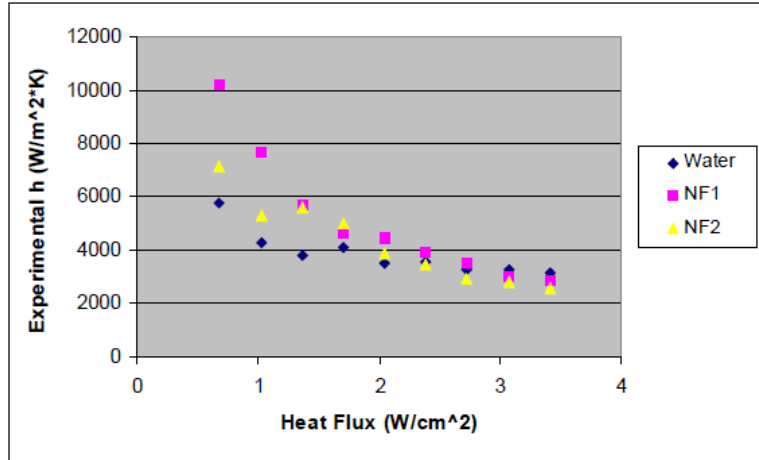
Note: Re values that could not be reasonably extrapolated were left blank (-).

As per Rosa et al.’s concluding recommendation mentioned at the end of Section 4.3.1, the relevant data and interpretations have been graphed and tabularized in Figure 27 and Table 6, respectively, for later reference. Referring to Figure 27, it must be noted that some of experimental Nusselt numbers categorized in Table 6 to be in the balanced (Hausen accuracy) regions were over 10% lower than corresponding Hausen values. The reason for this was deduced to be the

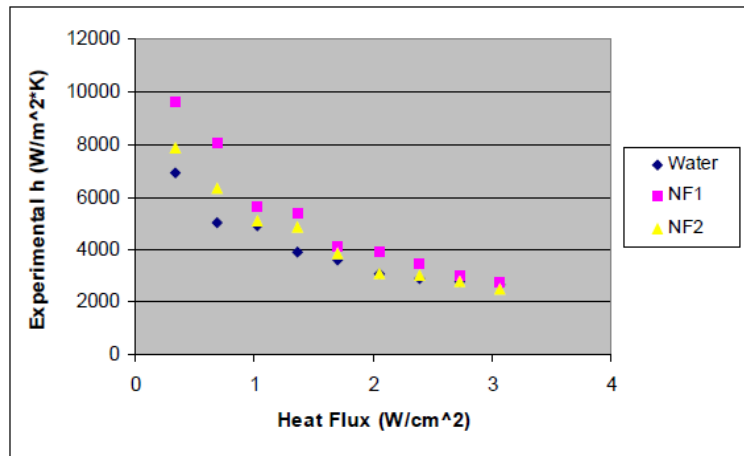
following: even though in the balanced region ($Re_{S/R} > Re > Re_C$) either slip or roughness effects almost always served to counteract the conjugate heat transfer effects, sometimes, as seen in the cases of water and NF1 for applied heat flux values $\geq 1.705 \text{ W/cm}^2$, slip and roughness cancel each other out, as shown in Section 4.1, leaving conjugate heat transfer effects to more significantly reduce experimental Nusselt numbers. Notably, Section 4.5 will be dedicated to better understanding conjugate heat transfer in particular. Finally, the parties of interest, namely, UMCP and NSWC, and other researchers of the engineering community may also proceed to interpolate and/or extrapolate data from Figures 26 and 27, and Tables 5 and 6 as per their research needs.

4.3.3: Heat Transfer Coefficient Analysis

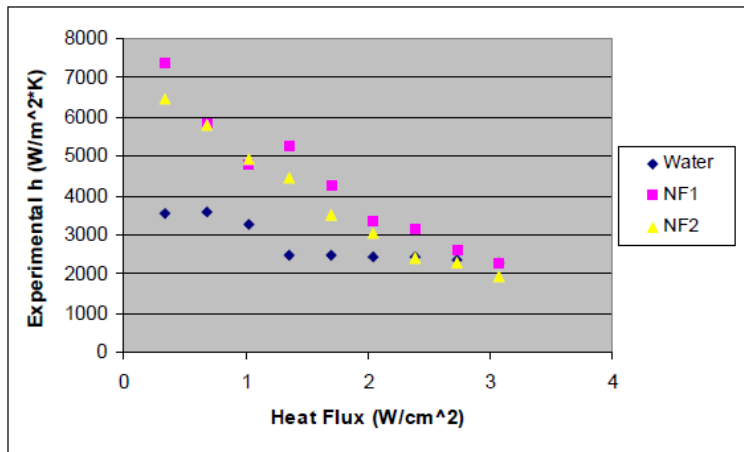
Now that Sections 4.3.1 and 4.3.2 have thoroughly explained the significance of scaling effects on the relevant experimental test runs, this section will rate the actual microchannel cooling performance of water, NF1 and NF2 under all relevant thermal and flow conditions in terms of the heat transfer coefficient. Nusselt numbers are typically useful correlative parameters as seen above, however, they represent the ratios of heat transfer coefficient to thermal conductivity of the coolant, whereas heat transfer coefficients provide the most direct and accurate measure of cooling performance via forced convection. Thus, Figure 28 graphically presents the experimental heat transfer coefficients against applied heat flux for all coolants at each flow rate.



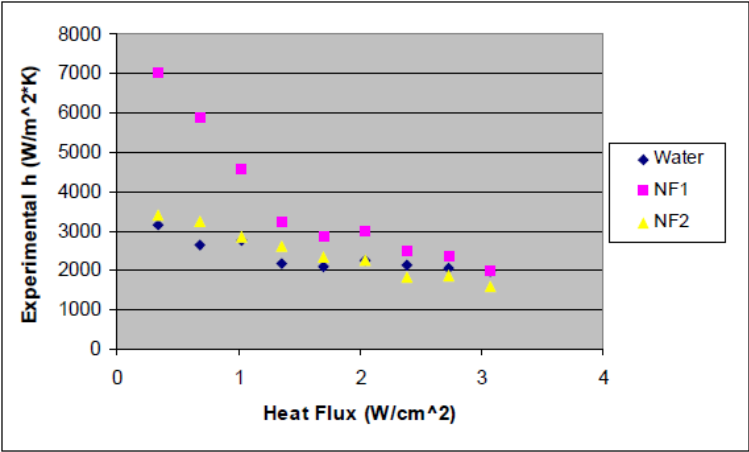
1.53 LPM



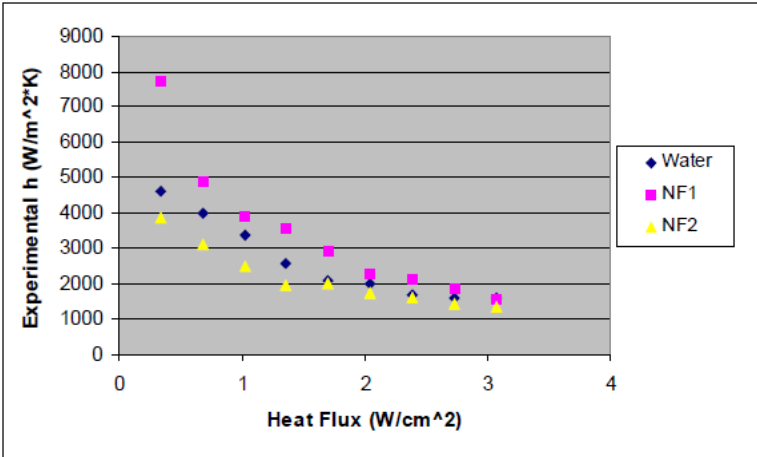
1.36 LPM



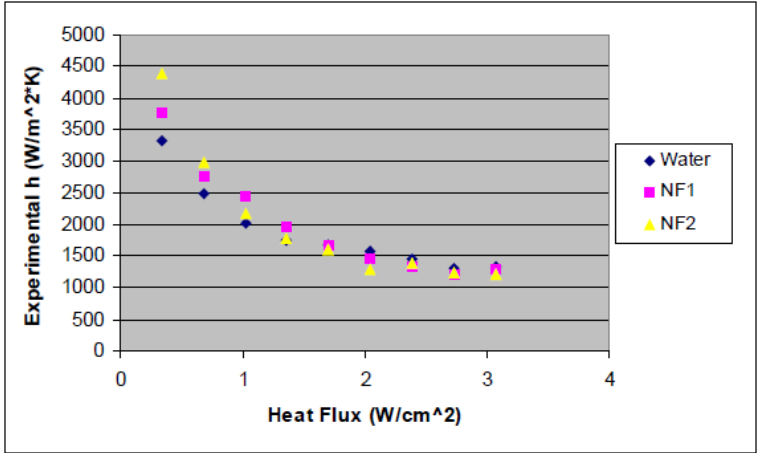
1.13 LPM



0.99 LPM



0.78 LPM

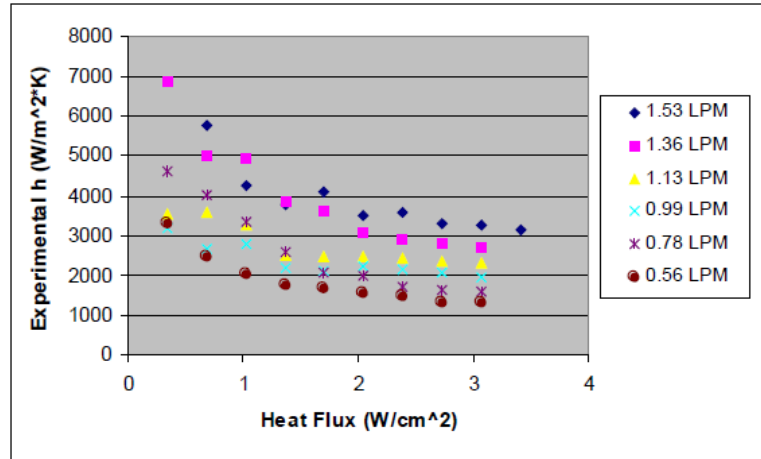


0.56 LPM

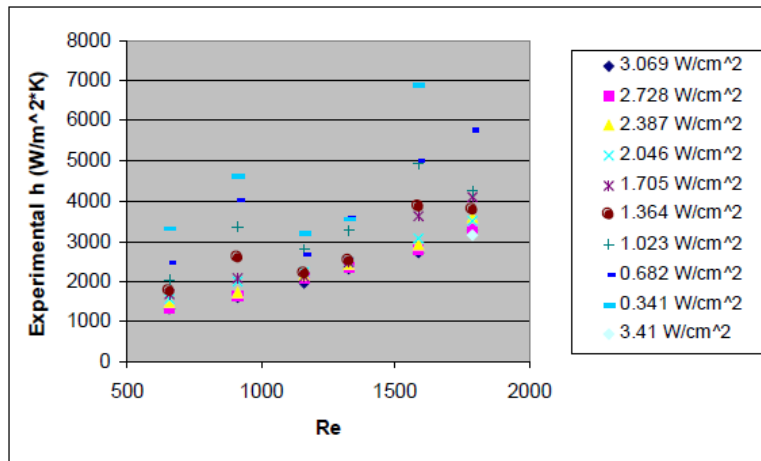
Figure 28: Experimental heat transfer coefficients against applied heat flux at all 6 relevant flow rates.

It is clear from Figure 28 that at each flow rate, the experimental heat transfer coefficient of each coolant nearly monotonically decreased in a nonlinear manner with applied heat flux. The main reason for this trend is that conjugate heat transfer effects became increasingly more significant with applied heat flux. Therefore, the highest heat transfer coefficients were observed at the lowest applied heat flux values. The heat transfer coefficients of most of the test runs fell within the range of 1000-5000 W/m²-K. The absolute highest heat transfer coefficient of 10,200 W/m²-K in the relevant experimentation was obtained in the test run with the following conditions: NF1 coolant; 1.53 LPM flow rate; and 0.682 W/cm² heat flux. In fact, NF1 appears to have outperformed water and NF2 in cooling at almost every heat flux value for each flow rate as shown in Figure 28—this phenomenon is much more prominent at higher flow rates and lower heat fluxes, where conjugate heat transfer was least significant. NF2 typically performed intermediately and water was seen to cool almost as effectively at most flow rates. It is also worthy to note that coolant performance was strongly positively associated with the magnitude of surface roughness effects, or the Re_R values discussed in Section 4.1 following Figure 23; conversely, since water had generally experienced the most slip effects it was observed to be the weakest performing coolant at most flow rates—indicating that surface roughness enhanced heat transfer considerably more than slip in the present experimentation. This association supports the surface roughness notion of Rosa et al. [22] mentioned in Section 4.3.1. Next, Figure 29 provides further graphical

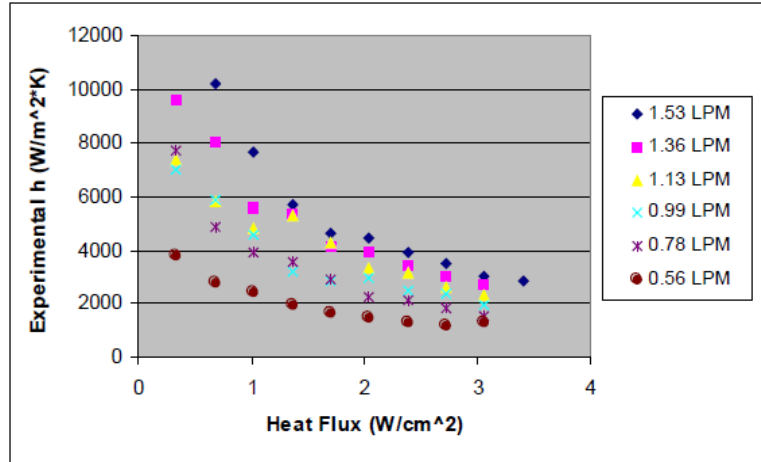
comparison of the experimental heat transfer coefficients of each coolant against applied heat flux and Reynolds number in the form of flow rate curves.



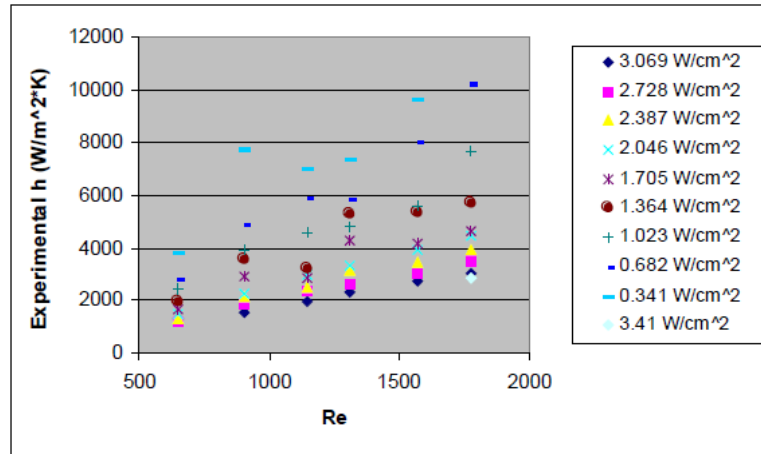
Water (h vs. HF)



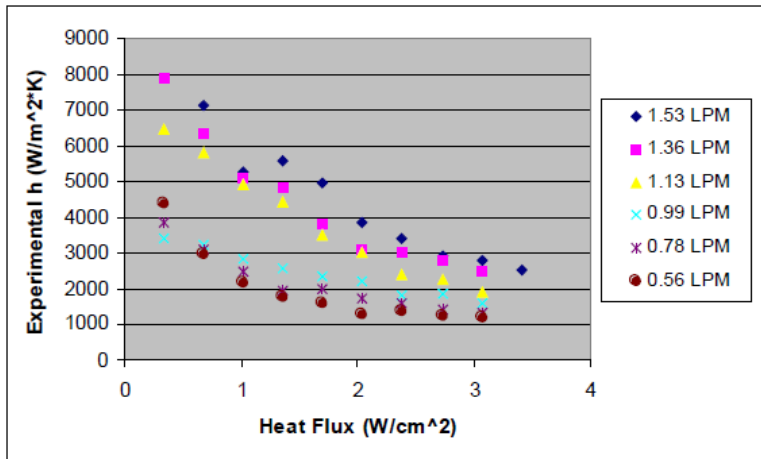
Water (h vs. Re)



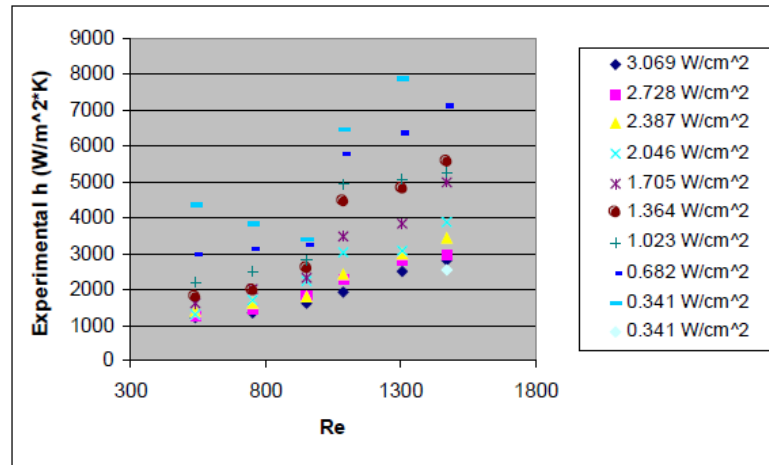
NF1 (h vs. HF)



NF1 (h vs. Re)



NF2 (h vs. HF)



NF2 (h vs. Re)

Figure 29: Heat transfer coefficients against heat flux and Reynolds number.

It can be seen in Figure 29 that in the case of each coolant, the highest shown flow rates intuitively yielded the highest experimental heat transfer coefficients.

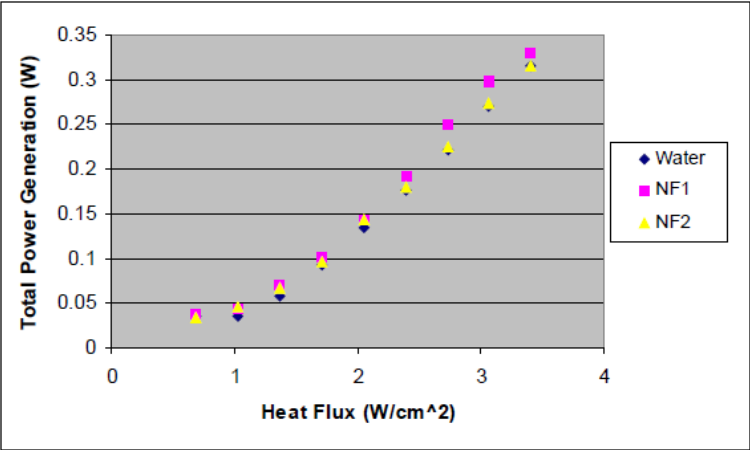
Furthermore, the h vs. Re graphs in Figure 29 show noteworthy non-monotonic trends that are related and somewhat similar to those of Figure 19, namely, the local minima/maxima at the above seen Reynolds numbers. The local minima occurring at intermediate Reynolds numbers were, as mentioned in Section 4.3.2, due to slip and roughness effects canceling each other and leaving conjugate heat transfer unchecked to reduce cooling performance, as opposed to higher and lower Reynolds numbers, where either slip or surface roughness, respectively, enhanced heat transfer. Therefore, the present microchannel heat transfer discussion is concluded as follows (with emphasis on Figures 28 and 29): high-Reynolds-number flows demonstrated the best cooling performance (highest heat transfer coefficients) especially when NF1 was used as the coolant; low-Reynolds-number flows provided the same fair cooling performance using each coolant due to the boost given by surface roughness effects against the

abovementioned conjugate heat transfer effects; intermediate-Reynolds-number flows generally showed poorer cooling performance due in large part to conjugate heat transfer, which was exacerbated by the relatively high thickness (10.72 mm) of the microchannel. Additionally, the benefit of excess pumping power reduction due to slip (see Figures 20 and 23) at higher Reynolds numbers further encouraged the pumping of coolants at higher flow rates for the sake of optimal cooling output with minimal parasitic power losses. Although optimal *cooling performance* occurred at higher flow rates/Reynolds numbers, the *net power generating performance* of the microchannel-thermoelectric power generator—the utmost priority for device feasibility—was contrarily optimal at lower flows as will be seen in Section 4.4.

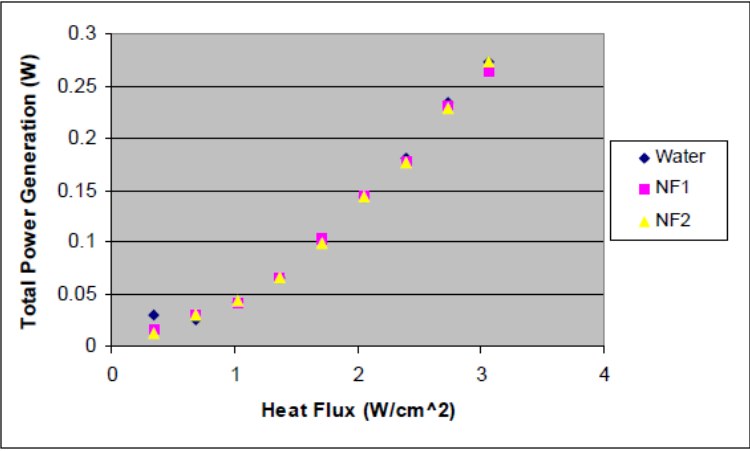
4.4: Thermoelectric Power Generation Analysis

The objective of this section is to present an evaluation of the overall performance of the thematic microchannel-thermoelectric power generator (MC-TEPG) in terms of maximum potential and net power generation under the abovementioned varying experimental conditions of coolant type, flow rate and applied heat flux. As described in Chapter 2, the thermoelectric modules generate power via the Seebeck effect (see Section 2.1)—a voltage is induced by an imposed temperature difference across the thermoelectric modules. In this particular case, the cooling of the thermoelectric cold side was done by the forced convection of /alumina-in-water nanofluid coolants in the microchannel, and the heating of the thermoelectric hot side was done by the thin film heater, thus, achieving the

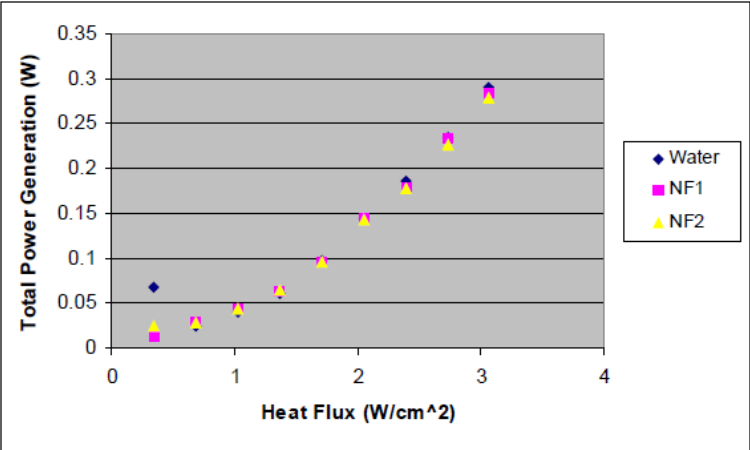
imposition of temperature difference and resulting in voltage readings that were recorded in each test run. From these voltage data, the maximum possible power generation values were computed using the thermoelectric power generation equation given by Da Rosa [9] as: $P_L = I * V_{TE} = [\alpha * (T_H - T_C) / (R + R_L)] * V_{TE}$, where I is the current through the load, V_{TE} is the induced thermoelectric voltage, α is the Seebeck Coefficient, T_H and T_C are thermoelectric hot side and cold side temperatures, respectively, R_L is the electric resistance of the load, and R is the internal electric resistance of the thermoelectric module. It is pertinent to mention that the values of V_{TE} , T_H and T_C were experimentally obtained for each test run, the values of α and R were computed, based on T_H and T_C , using Equations 3 and 4 and Table 1 of Maneewan et al. [12], which were specifically for TEC1-12708 thermoelectric modules. In order to compute the maximum possible, or matched-load, thermoelectric power generation ($P_L = P_{L,max}$), the load resistance R_L was matched with, or set equal to, the thermoelectric resistance R in each test run. The total possible thermoelectric power generation by the relevant MC-TEPG from each test run against heat flux is graphically presented in Figures 30 (flow rate curves) and 31 (coolant curves) below.



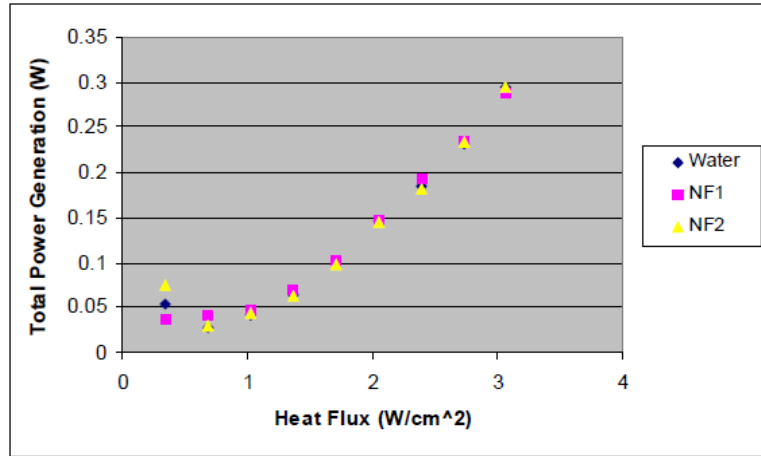
1.53 LPM



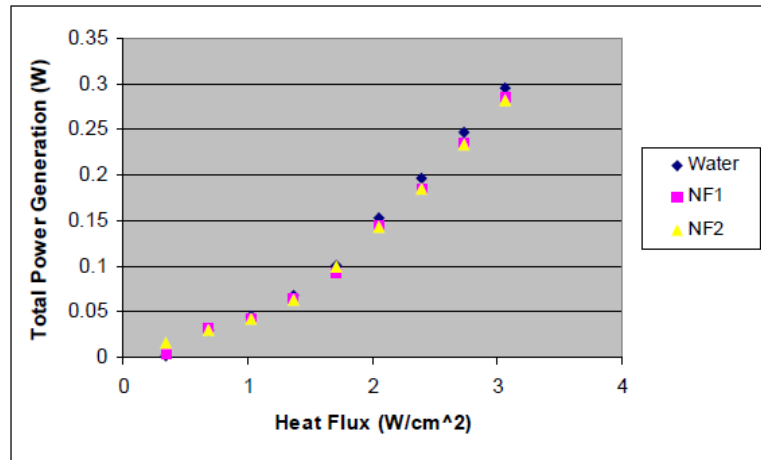
1.36 LPM



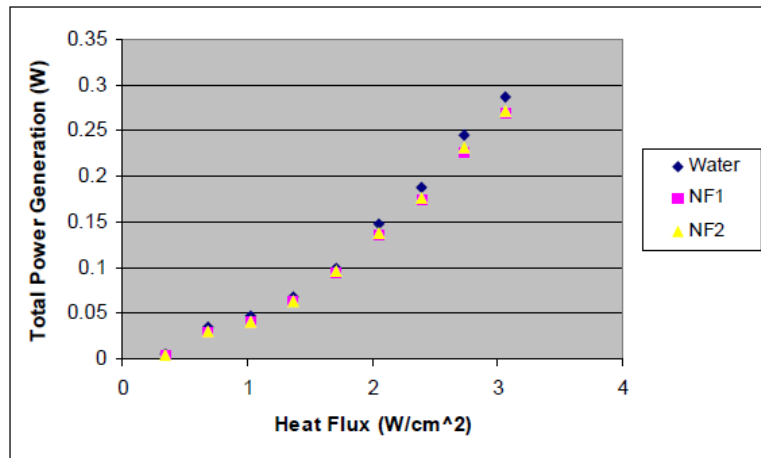
1.13 LPM



0.99 LPM

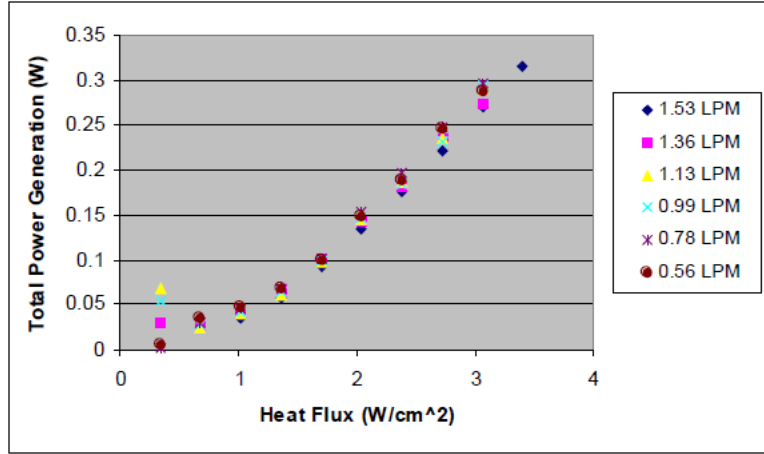


0.78 LPM

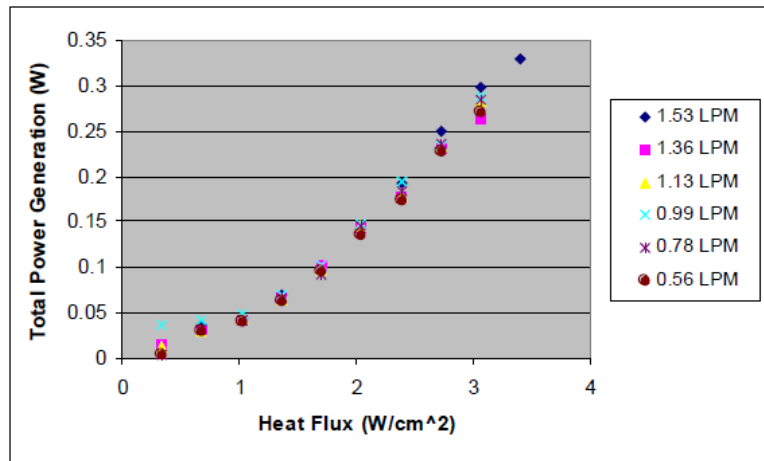


0.56 LPM

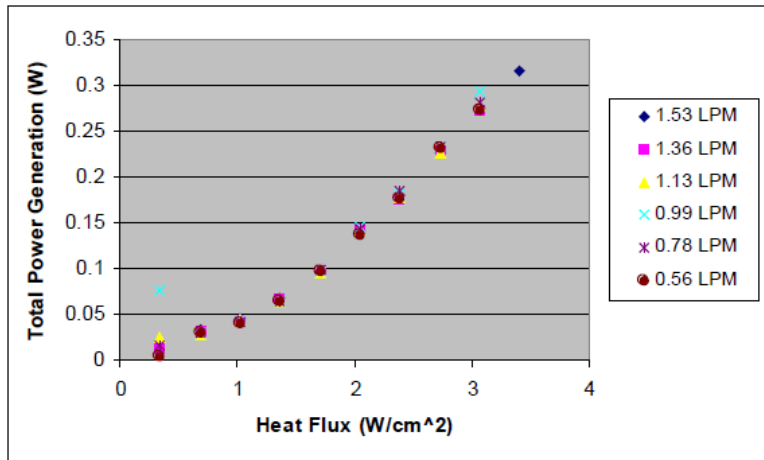
Figure 30: Total thermoelectric power generation against applied heat flux—coolant curve comparison.



Water



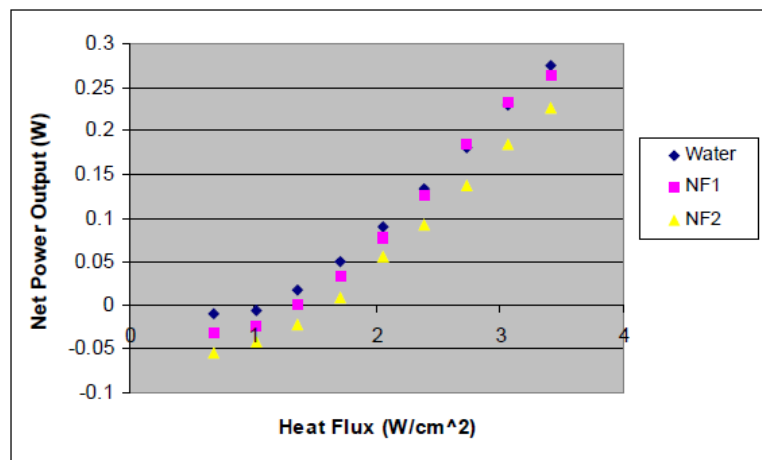
NF1



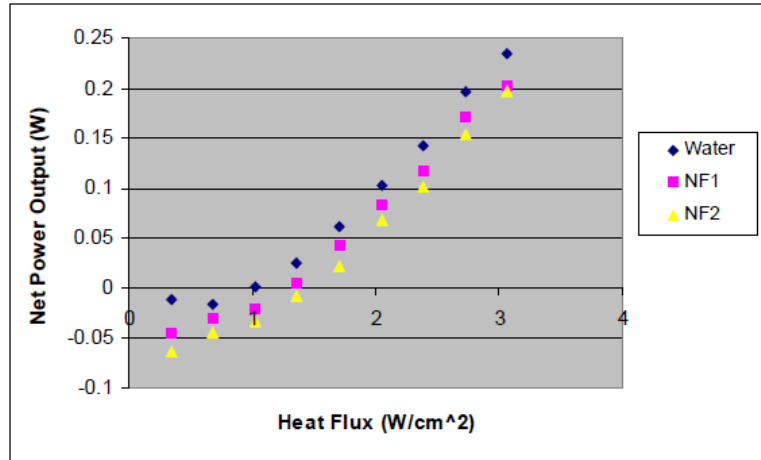
NF2

Figure 31: Total thermoelectric power generation against applied heat flux— flow rate curve comparison.

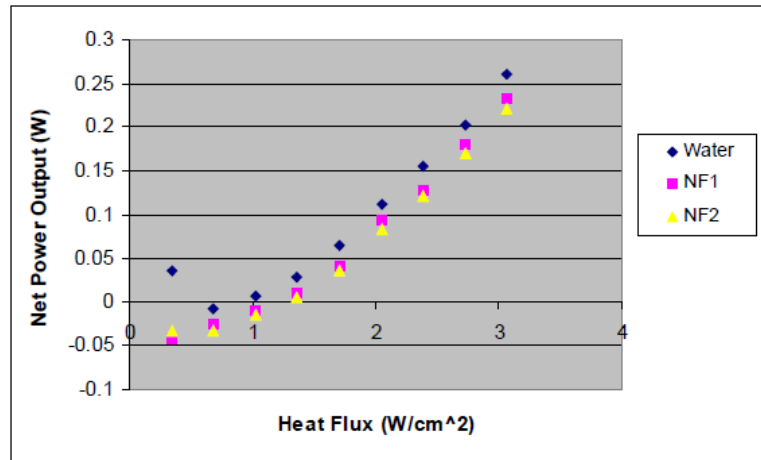
It is evident from Figures 30 and 31 that the total power generation values pertaining to each test run showed a very weak, almost negligible, dependence on coolant type and flow rate. Total power generation varied mostly only with applied heat flux in a positive and nearly linear association. The magnitudes of total power that could have been generated in each test run fell within the range of 0 to 0.35 W. Although total power generation was an important aspect of the present thesis, it was not enough to complete the evaluation of the overall performance of the MC-TEPG as power input—the excess pumping power illustrated in Figure 20—into the device was certainly significant and had to be accounted for. Therefore, the current argument will proceed to analyze the maximum possible net power output, that is, the difference between the total power generation by the TEC1-12708 modules and excess pumping power requirement, of the MC-TEPG in each test run. The maximum possible net power output by the relevant MC-TEPG in each test run against heat flux is graphically presented in Figures 32 (flow rate curves) and 33 (coolant curves) below.



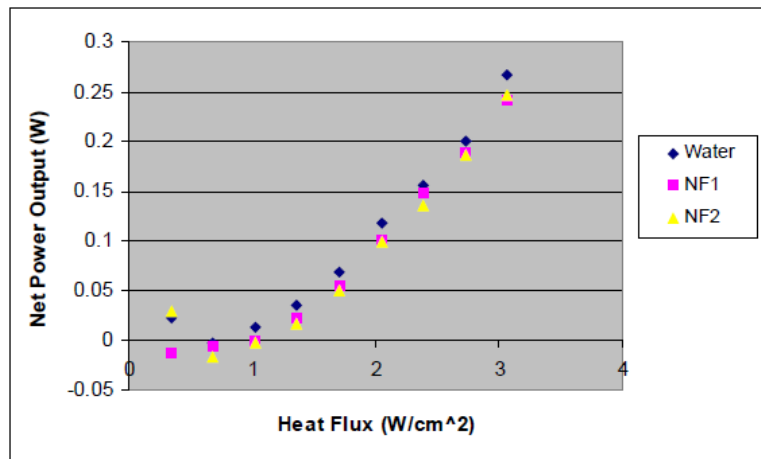
1.53 LPM



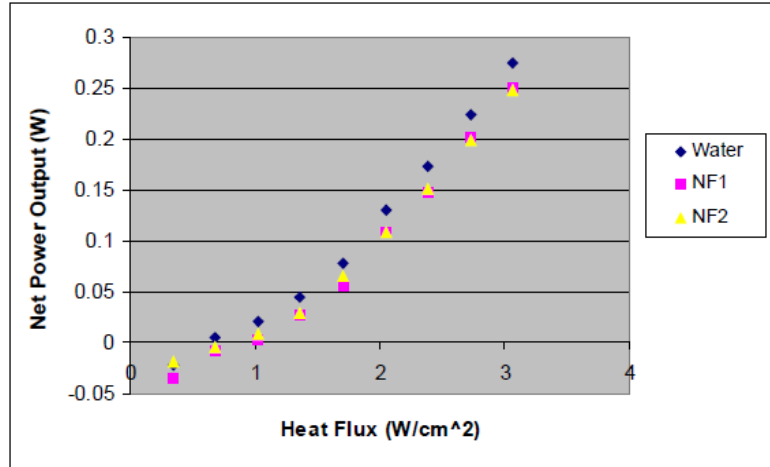
1.36 LPM



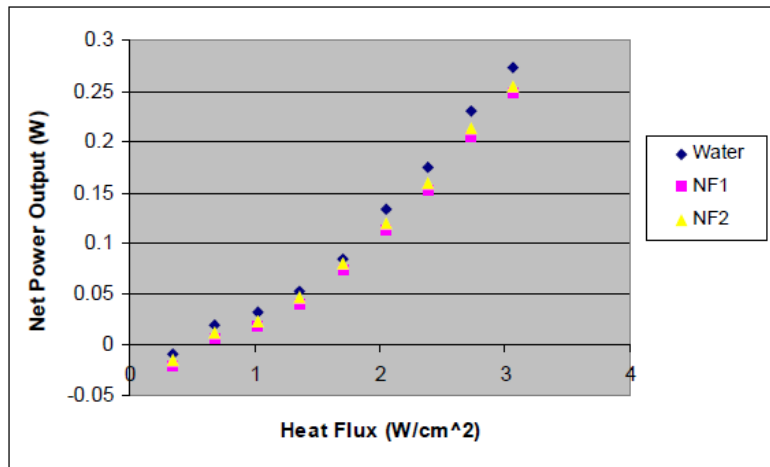
1.13 LPM



0.99 LPM

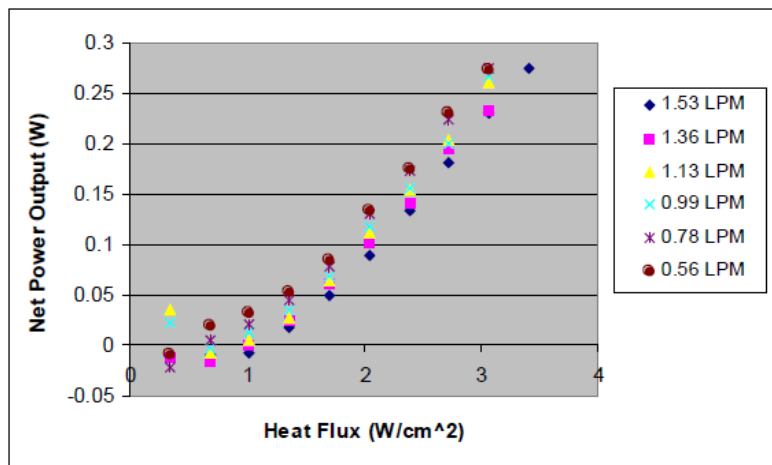


0.78 LPM

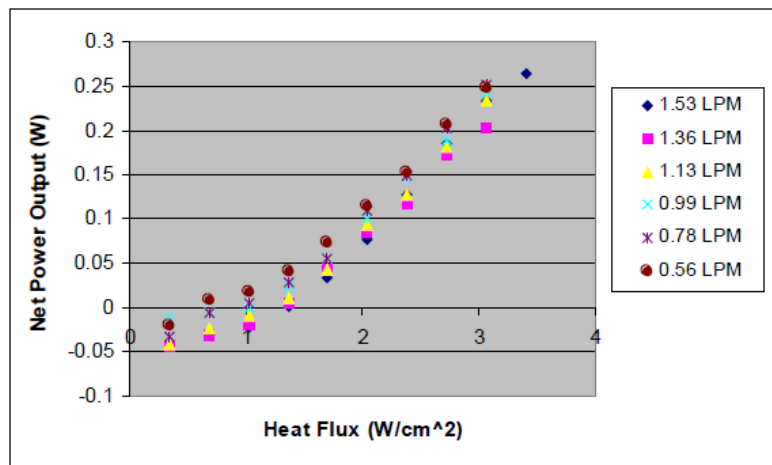


0.56 LPM

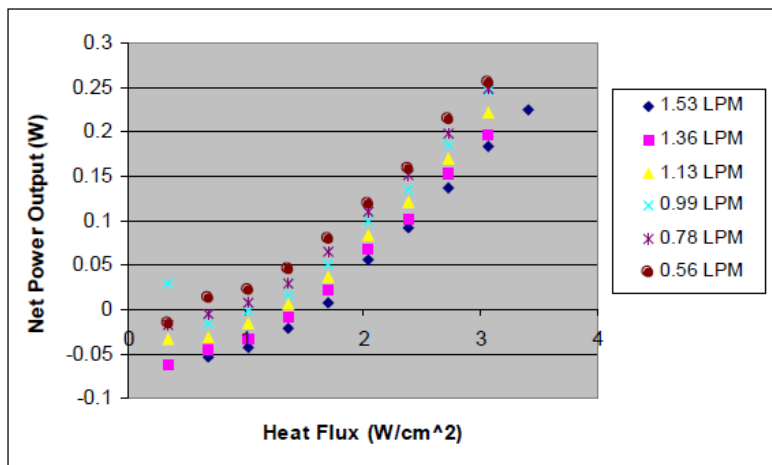
Figure 32: Net power output against applied heat flux—coolant curve comparison.



Water



NF1



NF2

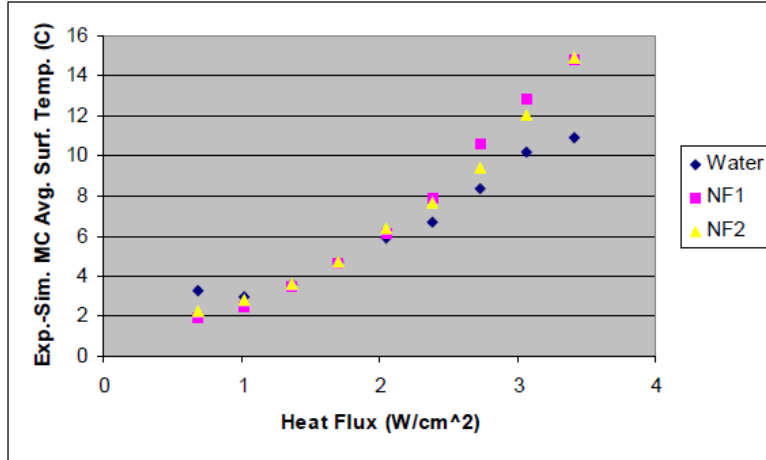
Figure 33: Net power output against applied heat flux—flow rate curve comparison.

Since total power generation was almost invariant with coolant type and flow rate, excess pumping power was basically the sole contributor to variation from test run to test run of net power output, and thus, the overall performance of the MC-TEPG. In short, the lower the excess pumping power requirement for pumping a given coolant at a given flow rate, the higher the net power out. It is evident from Figure 32 that, in strong agreement with the above statement, water had outperformed both nanofluids essentially at each corresponding flow rate and heat flux, while NF1 rendered higher net power output than NF2 at essentially all heat flux values for the 4 higher flow rates but equivalent and lower values than NF2 for the flow rates of 0.78 LPM and 0.56 LPM, respectively. Also in strong agreement with the above observations, Figure 33 shows that for each coolant at essentially each fixed heat flux value, net power output increases monotonically with decreasing flow rate/excess pumping power. The magnitudes of net power output that could have been delivered in each test run were in the range of -0.07 to 0.27 W, with negative values indicating an overall loss of power due to the excess pumping power surpassing the total generated power. Notably from Figures 32 and 33, the MC-TEPG would not be worth running at lower heat fluxes, especially at higher flow rates, because the device would hypothetically consume more power than it would be able to generate. Therefore, it is concluded in this section that the alumina-in-water nanofluids, NF1 and NF2, were inferior working fluids to plain water, when considering MC-TEPG net power output, as they required more power in order to be pumped through the microchannel but did not

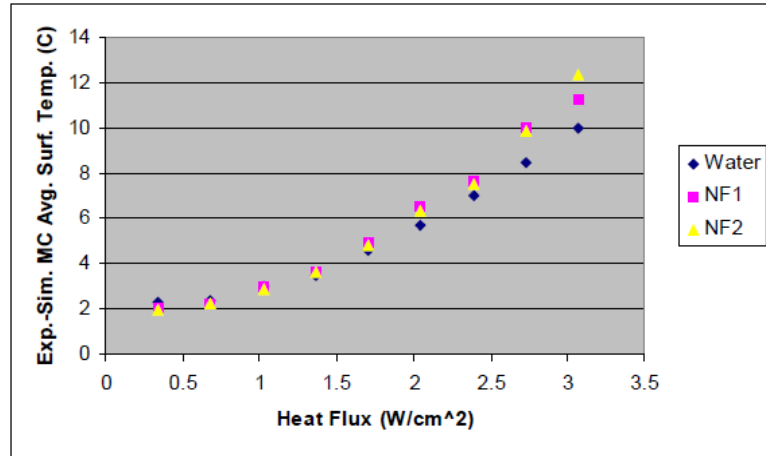
indicate any potential for total power generation augmentation over that rendered by water.

4.5: Simulation Results and Analysis

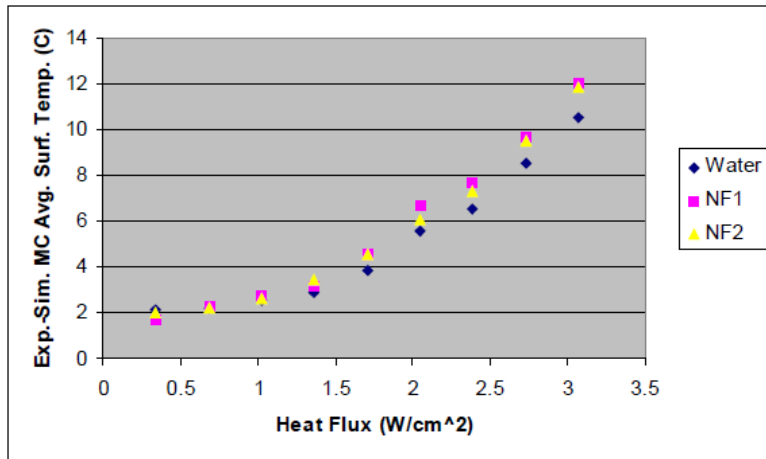
The purpose of this section is to discuss the findings of the ProEngineer-Mechanica computer simulation described in Section 3.5 and compare them with those of experiment in order to gain further insight into the role played by conjugate heat transfer in the relevant experimentation. As mentioned in Section 3.5, average microchannel heated-surface temperatures were recorded in each of the 162 simulation runs. These temperatures were then checked against their thermocouple-measured experimental counterparts. The difference between experimental and respective simulation average microchannel heated-surface temperatures against heat flux is graphically presented in Figures 34 (flow rate curves) and 35 (coolant curves) below.



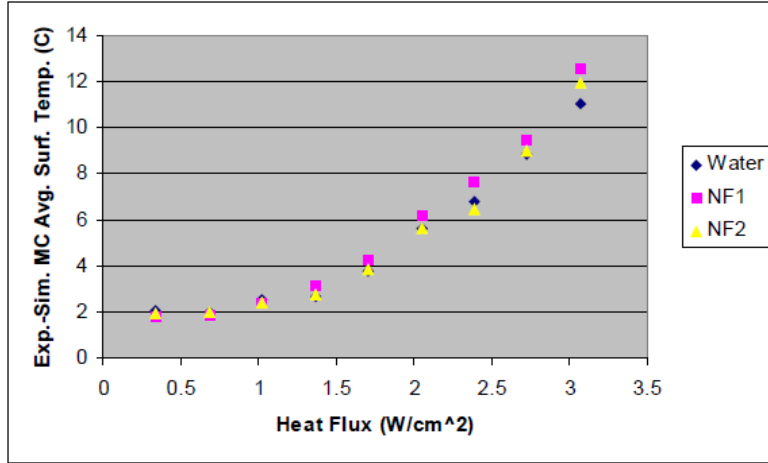
1.53 LPM



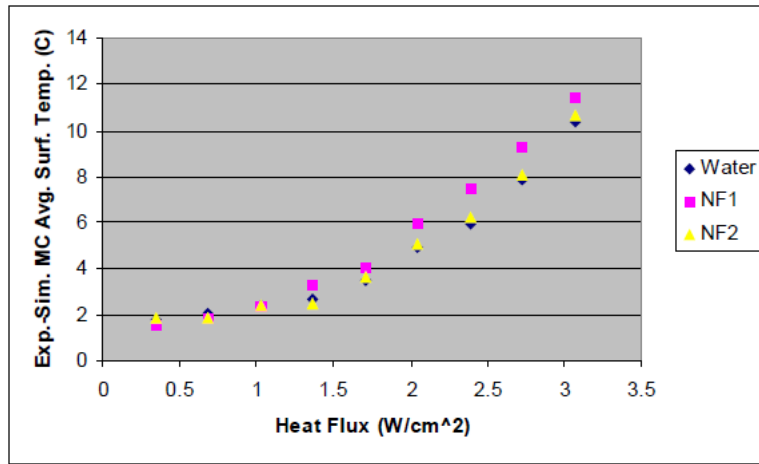
1.36 LPM



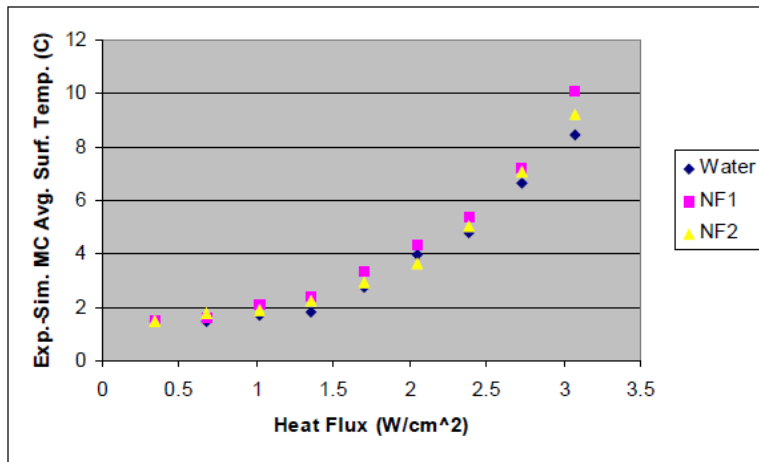
1.13 LPM



0.99 LPM

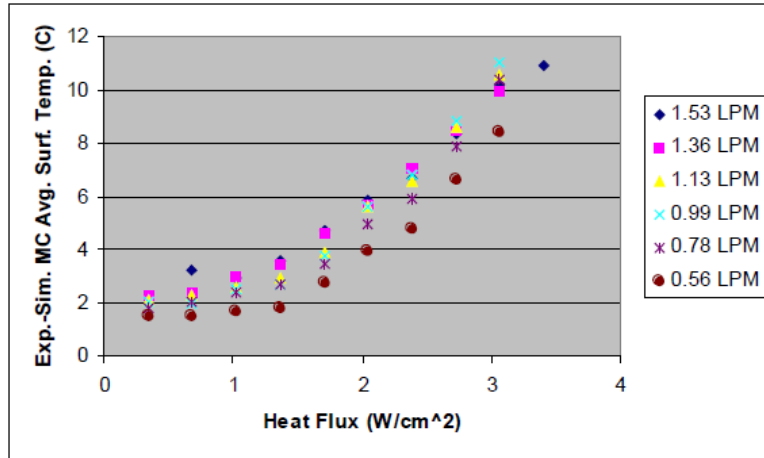


0.78 LPM

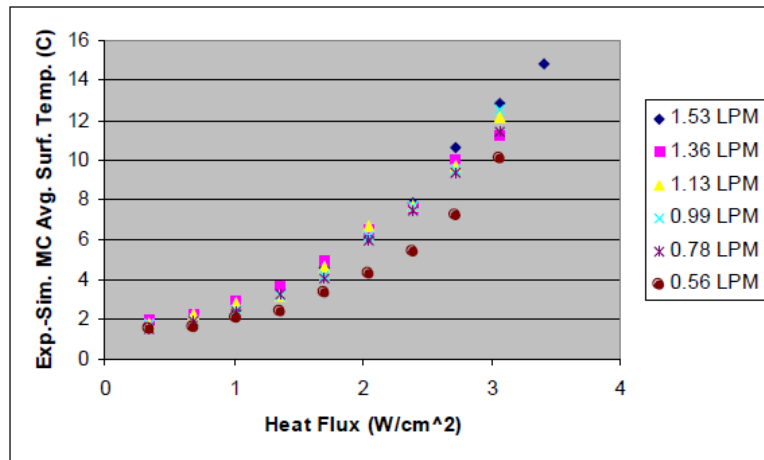


0.56 LPM

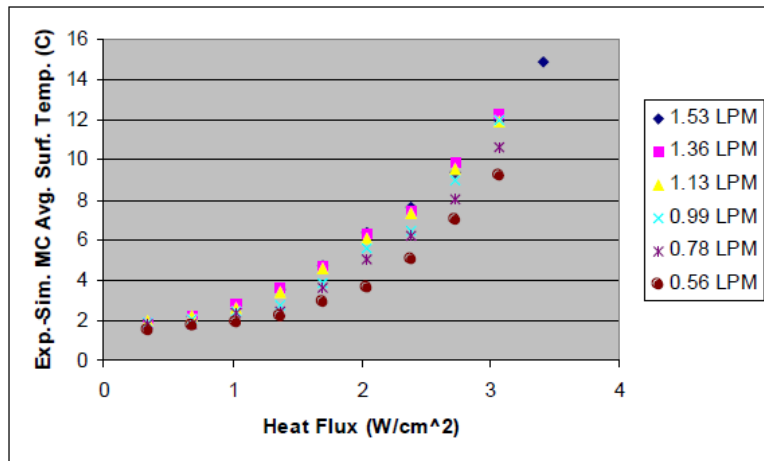
Figure 34: Difference between experimental and simulation microchannel temperatures against applied heat flux—coolant curve comparison.



Water



NF1

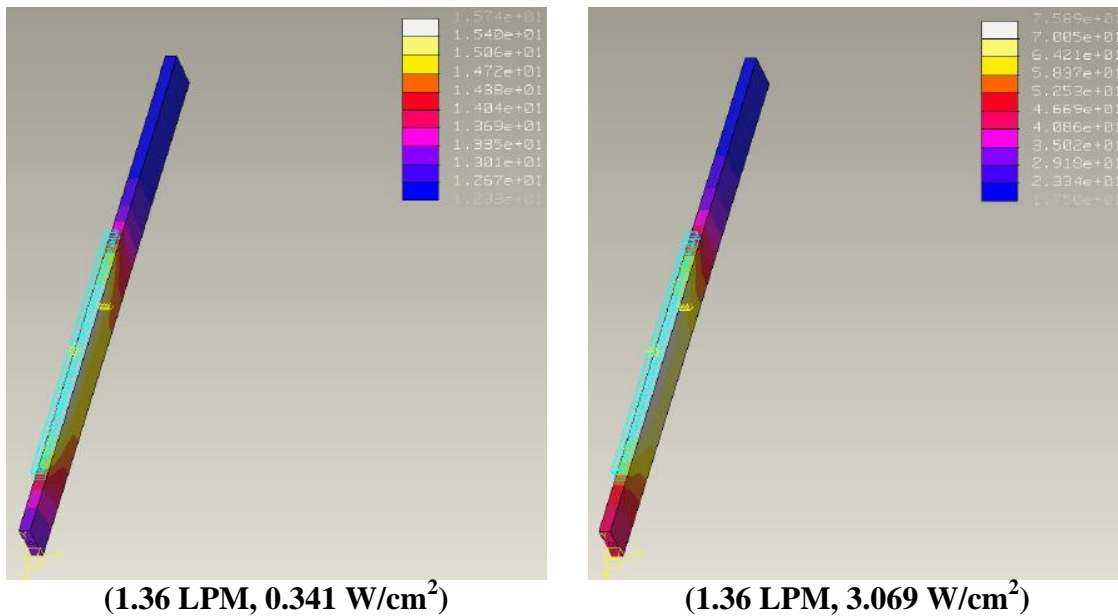


NF2

Figure 35: Difference between experimental and simulation microchannel temperatures against applied heat flux—flow rate curve comparison.

Figure 34 shows that, for each flow rate, the experiment-simulation temperature difference curves of all 3 coolants closely resembled one another in trend and magnitude with NF2 yielding slightly higher temperature differences than water but slightly lower than those of NF1 at higher heat fluxes. As seen in Figure 35 for each coolant, smaller differences between experimental and simulation temperatures, and thus, better agreement between experiment and simulation, were observed for lower flow rates; however, temperature differences along with disparity between experiment and simulation increased significantly with increasing flow rate. Specifically, temperature differences were as low as 2 °C at lower heat fluxes and rose nonlinearly to 8-15 °C at higher heat fluxes. The first reason for this occurrence, as said in Section 4.3, was that conjugate heat transfer effects were intuitively not very significant at lower heat fluxes. Hence at lower heat fluxes, the small differences between experimental and simulation temperatures were attributed to a combination of the following factors: very slight intrinsic errors in experiment such as less-than-ideal thermal interfacing and thermocouple interference to heat flow; errors in simulation such as slight inaccuracy in material property assignment (especially in the case of the thermoelectric semiconductor material, the exact composition of which was unknown) and the fact that the coolant flow of experiment was replaced by a bulk-temperature-based convection condition in simulation due to ProEnigineer's inability to program liquid flow as mentioned in Section 3.5. However, at higher heat fluxes, the relatively large differences between experimental and simulation temperatures were mostly attributed to the significance of conjugate heat transfer

effects, including axial conduction. Before proceeding with this discussion, it is worthy to reiterate that the conjugate heat transfer effects present throughout the relevant experimentation were strongly believed to be 3-dimensional and not simply 2-dimensional (axial conduction only), which is typically the case with such micro-scaled experimentation as per a major conclusion of Rosa et al. [22]. The remainder of this section will provide evidence to this end by further analyzing the simulation results and comparing them with those of experiment. On this note, Figure 36 illustrates the pertinent (steady state) surface temperature variation from 4 of the simulation runs, corresponding to 4 of the experimental test runs that used water as the coolant, of the *simulated portion* of the microchannel heat exchanger (see Figure 17).



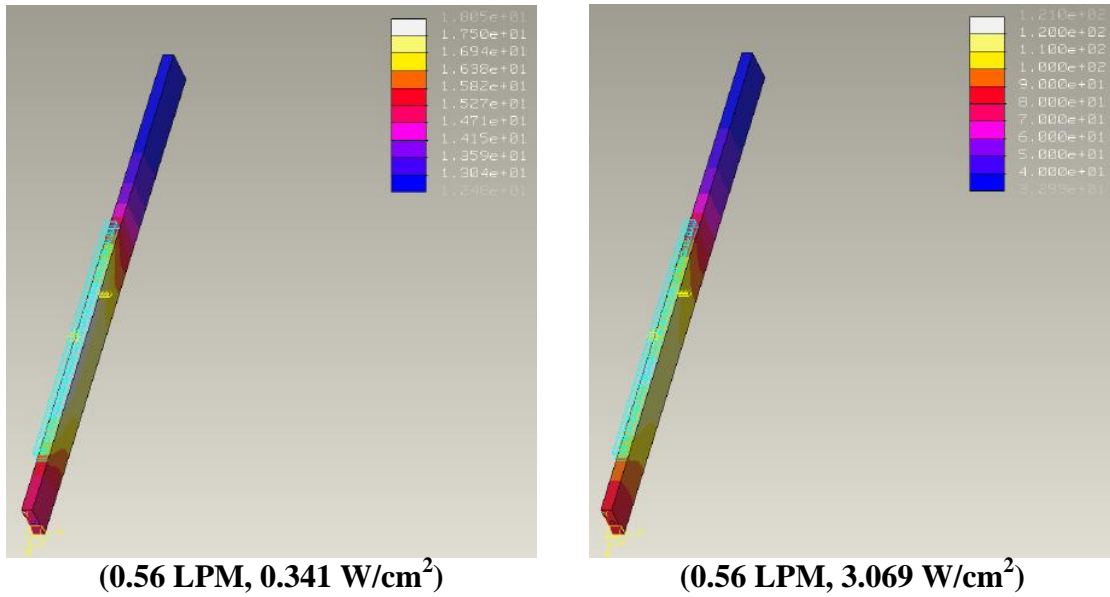


Figure 36: Microchannel surface temperature variation from 4 simulation runs. All temperatures shown at the top right of each image are in °C.

As seen from Figure 36, at the relatively low applied heat flux of 0.341 W/cm^2 , the 1.36 and 0.56 LPM simulation runs showed axial temperature variations, from microchannel inlet to about 60 mm downstream (right before reaching the heated length), of only about $1.4 \text{ }^\circ\text{C}$ ($13.7\text{-}12.3 \text{ }^\circ\text{C}$) and $2.3 \text{ }^\circ\text{C}$ ($14.7\text{-}12.4 \text{ }^\circ\text{C}$), respectively—indicating a low significance of axial conduction at low heat fluxes, and thus, confirming the statements of Section 4.3. On the contrary, at the relatively high heat flux of 3.069 W/cm^2 , the 1.36 and 0.56 LPM simulation runs showed much higher axial temperature variations of about $23.3 \text{ }^\circ\text{C}$ ($40.8\text{-}17.5 \text{ }^\circ\text{C}$) and $37.1 \text{ }^\circ\text{C}$ ($70.0\text{-}32.9 \text{ }^\circ\text{C}$), respectively—indicating an undeniably high significance of axial conduction at high heat fluxes, especially when flow rates were low. It is important to note that these findings from Figure 36 only reasonably estimated the significance of 2D axial conduction and not of the all of the effects of 3D conjugate heat transfer present throughout experimentation. This

is so because the microchannel of simulation contained only 1 single micro-sized channel, whereas, the experimental microchannel heat exchanger was much wider since it consisted of 12 channels in parallel—not allowing for *widthwise* conjugate heat transfer effects to be considered in simulation. Hence, it was deduced that the main reason why experimental microchannel surface temperatures always exceeded their simulation counterparts, as shown in Figures 34 and 35, was that simulation yielded temperatures that were affected only by axial and thickness-wise conduction (2D/fractional conjugate heat transfer), whereas, experimental temperatures were affected by widthwise conduction as well (3D/total conjugate heat transfer). In conclusion, the above simulation analysis has proven by deduction the claim made in Section 4.3 that conjugate heat transfer effects were present throughout the relevant experimentation and were indeed 3-dimensional and not simply 1 or 2-dimensional. Detailed conclusions on the performance of the MC-TEPG as per the results and analysis presented in this chapter can be found in Chapter 5 of this thesis.

Chapter 5: Conclusions and Future Work

5.1: Conclusions

This thesis documents the results of research on the performance of a microchannel-thermoelectric power generator (MC-TEPG) that uses alumina-in-water nanofluids as coolants. This section will conclude the present work by discussing the applicability of the relevant MC-TEPG to navy aircraft such as the C-17, B-52 and no-man surveillance drone as per the analysis of Chapter 4. As noted in Chapter 1, the present thesis project was carried out with a general goal and three additional analytical objectives in the ARPA-E spirit of inexpensive or ‘self-funded’ research work. The general goal of this project had been to achieve a positive net power generation and prove the feasibility of the MC-TEPG. The first additional objective was to compare the measured friction factors (nondimensionalized pressure drop), thus also, the parasitic powers for each test run to their theoretical counterparts (obtained via macrochannel correlations, and microchannel correlations proposed in recent microchannel research articles). The second objective was to assess and make certain the coolant flow regime inside the microchannel for each test run was indeed laminar using a Brinkman Number-based analysis. The third objective was to assess the cooling/heat dissipation merit of each coolant conjunct with the microchannel in each test run primarily by computing the experimental mean Nusselt Numbers (nondimensionalized heat transfer coefficient) and comparing them to each other and their respective theoretically computed counterparts.

With the above objectives set forth, the microchannel heat exchanger (central component of study), test section (prototype of the actual MC-TEPG device) and test rig were designed and constructed, and the experimental and simulation procedures were planned with careful consideration of certain ‘scaling effects’ that have been known to typically play up at the micro-scale. Namely, the scaling effects considered in the present thesis were those of thermal entrance, 3-dimensional conjugate heat transfer, viscous heating, temperature-dependent coolant properties, wetted-surface roughness, and hydrophobic/pressurized slip flow. The microchannel used in the relevant experimentation was strategically designed, constructed and prepared to encourage coolant slip flow, even at relatively low shear rates ($<10,000 \text{ s}^{-1}$), so that slip effects may be studied and pressure drop/excess pumping power requirements may be reduced below those of the no-slip boundary condition. Thus, the microchannel was made of AA 2014 (a readily available aluminum alloy) and had wetted channel surfaces of 10% relative roughness, which were passivated to successfully create a thin (less than 1 μm thick) microlayer of *hydrophobic* alumina in order to encourage coolant velocity slip at the walls. The relevant test section, which proved to be quite reliable, was assembled using a previously ‘tried-and-true’ method: thermal interfacing via nut-and-bolt compression and thin graphite sheet material; mechanical interfacing via headers, gaskets, standard tube fittings and nut-and-bolt compression. The relevant experimental apparatus was a closed-loop test rig consisting of a primary and secondary loop to accommodate a wide variety of coolants for not only the present work, but future research plans of the NSWC as

well; notably, the secondary loop remained unused in the present work, as water and the alumina-in-water nanofluids were compatible with the wetted materials of all components of the test rig. In the experimentation, 3 distinct coolants were used—plain water and 0.13 vol% and 0.50 vol% alumina-in-water nanofluids termed NF1 and NF2, respectively—in conjunction with the microchannel, with 6 distinct coolant flow rates (all verified to be within the single-phase laminar flow regime) corresponding to each coolant, and 9 different heater settings for each coolant-flow rate set, making a total of 162 test runs that were analyzed and compared to each other. Finally, 1 computer simulation run using the Mechanical subprogram of ProEngineer was performed parallel to each of the 162 experimental test runs to gain further insight into the nature of the microchannel heat transfer, particularly conjugate heat transfer effects, pertaining to this experiment.

The results and analytical discussions of this thesis covered, as per the abovementioned project objectives, the pertinent performance aspects of pressure drop, cooling performance and maximum possible net power output while accounting for the abovementioned scaling effects. As immediately noticed from experimental results and as originally hypothesized, the coolant temperature rose by only 2.6 °C or less from the microchannel inlet to the outlet in all 162 test runs, clearly rendering the scaling effect of temperature dependent coolant properties negligible. Also, experimental observation combined with Morini flow model-based estimation pertaining to each test run led to the inference that viscous

heating effects were insignificant—less than or equal to about 3% of the total heat dissipated by the coolant in the microchannel—throughout experimentation as previously assumed. After having ruled out the significance of 2 of the 6 major scaling effects, the rest of the experimental results were then analyzed in terms of the remaining scaling effects to determine the overall performance of the MC-TEPG.

First and foremost, it was proven based on experimental thermoelectric voltage readings that the relevant prototype MC-TEPG could ideally provide a net power output of up to 0.27 W—a modest value but enough to accomplish the general goal of this project and encourage future research by the NSWC intended to advance the merit of this device towards marketability. It is worthy to note that, for fixed flow rates and applied heat flux values, water and the alumina-in-water nanofluid coolants yielded essentially equal maximum possible power generation values in each test run; however, water had outperformed both nanofluids essentially at each corresponding flow rate and heat flux, while NF1 mostly rendered equivalent or higher net power output values than NF2. The underlying reason for this was that net power output depended on the excess pumping power requirement and therefore, fluid viscosity, which increased as alumina volume fraction increased, thus, making plain water—the least viscous fluid (0.00105 Pa-s; whereas, NF1: 0.00106 Pa-s, NF2: 0.00128 Pa-s)—the optimal working fluid in the MC-TEPG. Therefore, it is concluded that alumina-in-water nanofluids are not worthwhile working fluids, within the flow rate and heat flux conditions tested in

this experiment, as they provide negligible enhancement (over water) to gross maximum possible power generation, while requiring considerably higher pumping powers than plain water (at corresponding flow rates and heat fluxes) to flow through the microchannel. It is also important to point out that at lower applied heat fluxes, especially when flow rates were high, the parasitic power (excess pumping power requirement) exceeded maximum possible power generation values to yield negative net power output, intuitively proving the MC-TEPG to be ineffective at low heat fluxes. This is yet another expected conclusion as applied heat flux from the heater experimentally represents the waste heat from a military vehicle/machine such as a no-man surveillance drone; and since the relevant MC-TEPG is a waste heat recovery device it naturally would be and indeed is ineffective when there is little or no available waste heat to consume. Hence, it is recommended to operate the MC-TEPG at low flow rates using water as the working fluid for minimized pumping power requirement only when sufficient waste heat is available in order to take most advantage of the renewable energy power generation this device can provide.

Next, concluding remarks will be made on the excess pumping power/pressure drop (across the microchannel) as this was a very important limiting factor to the overall MC-TEPG performance and was, thus, given particular attention from preliminary design to final analyses in this project. As mentioned above, the microchannel wetted surfaces were purposefully designed to be rough with a thin, superficial passivated-alumina layer in order to promote low-shear hydrophobic

slip flow—this was achieved in the cases of all three relevant coolants. In particular, slip effects (friction factor reduction) were found to be predominant at higher flow rates/Reynolds numbers, whereas surface roughness effects (friction factor increase) were predominant at lower flows, and conventional laminar flow theory agreed strongly with the experimental friction factors of intermediate flows at which slip and roughness effects cancelled each other out. Notably, water was observed to experience more slip, and thus higher friction factor reduction below the Hagen-Poiseuille Theory, than the alumina-in-water nanofluids due its relatively lower viscosity. Specifically, experimental water friction factors at flow rates of 0.99-1.53 LPM were seen to be 18-51% below those of Hagen-Poiseuille, whereas those of NF1 and NF2 at flow rates of 1.36-1.53 LPM were 9-22% below and 7-15% below Hagen-Poiseuille, respectively. These reductions in friction factor due to the hydrophobic-slip-promoting microchannel design were a notable academic achievement, especially considering the nearly ‘self-funded’ of this project. However, when considering only the practical performance of the MC-TEPG prototype, the slip-induced friction factor reduction was not very advantageous as it was overtaken by surface roughness effects that raised friction factors 22-87% above Hagen-Poiseuille Theory at lower flow rates (<0.99 LPM) where the MC-TEPG was able to provide the most net power output. Although pressure/pumping power reduction advantage of hydrophobic-slip flow could not be extended to lower flow rates, valuable insight into the scaling effects pertaining to slip and surface roughness has been gained and documented in this thesis for future research plans involving the relevant MC-TEPG.

For the abovementioned pressure drop analysis, it was understood as per the latest microchannel research reviews that since all relevant Reynolds numbers were well below 2000 all experimental flows were fully laminar as in conventional macrochannel theory; however, some researchers still question the nature of the flow regime in microchannel when the flow rate is below 2000. Therefore, a Brinkman number-based analysis was carried out to for verification that all experimental flows were fully laminar—the second objective of this thesis. The tool used for this analysis was the $\log(\text{Br}_{tr})=2.00\log(\text{Re})-10.34$ locus derived by Tso and Mahulikar [26], in which, Br_{tr} is such that: flow is fully laminar if $\text{Br}-\text{Br}_{tr}>0$, else, it is in transition towards turbulence. It was immediately evident that essentially all $\text{Br}-\text{Br}_{tr}$ values were positive, thus, reinforcing the prior establishment of the flow regime in each test run to be fully laminar. It is concluded that Tso and Mahulikar's Brinkman number-based locus is an instrumental flow regime assessment tool and should be incorporated into the overall flow regime analysis in all microchannel applications.

Aside from the MC-TEPG power generation performance, the present thesis focused on the analysis and documentation of the heat transfer behavior/cooling performance of water and the alumina-in-water nanofluids in the relevant microchannel heat exchanger—the third objective of this thesis. The relevant heat transfer analysis compared experimental mean Nusselt numbers with those predicted by the Hausen correlation, while accounting for significant scaling effects so as to explain the disagreements observed between theory and

experiment—an effective approach as seen in recent microchannel research articles. It is worthy to note that Graetz numbers (Gz) pertaining to all test runs were in the range of 66 to 270 ($Gz > 10$), making thermal entrance effects considerable throughout the entire relevant experimentation and the Hausen correlation a most appropriate analytical tool. Along with these heat transfer-enhancing thermal entrance effects, the complex and deteriorating effects of 3-dimensional conjugate heat transfer and the enhancing abovementioned effects of slip and surface roughness were also present. In fact, due to scaling-effect enhancement of heat transfer, most experimental test runs yielded Nusselt numbers well above the fully developed laminar value of 4.36, with the highest being 20.5; on the other hand, under the conditions of relatively high heat fluxes values and low flow rates conjugate heat transfer effects, exacerbated by the inevitably high 10.72-mm microchannel heat exchanger thickness, degraded Nusselt numbers to as low as 2.3. The corresponding heat transfer coefficient range to the Nusselt number range of 2.3-20.5 is 1200-10,200 W/m^2-K —a decent cooling performance considering that this project was tightly budgeted and dealt only with single-phase, as opposed to two-phase, microchannel flow. As for the cooling performance comparison between water, NF1 and NF2: under most heat flux and flow rate conditions, water and NF2 cooled equivalently well due the fact that although NF2 bore a thermal conductivity 23% higher than that of water, its specific heat was about 2% lower; NF1 remarkably outperformed water and NF2 in terms of corresponding heat transfer coefficients by 20-90% at lower and intermediate heat flux values because its thermal conductivity was 21% higher

than that of water with essentially the same specific heat, however this enhancement fell to 0% at higher heat flux values due to conjugate heat transfer predominance. Paradoxically, NF1—the 0.13 vol% alumina-in-water nanofluid—proved to be a *considerably superior coolant* to plain water, although it and NF2 were *not worthwhile overall working fluids* as they provided no noticeable enhancement to MC-TEPG net power output.

In agreement with the current beliefs of the vast majority of microchannel researchers such as Rosa et al. [22], this thesis also concluded that simultaneously modeling such complex phenomena as slip, roughness, thermal entrance, conjugate heat transfer is, as yet, extremely difficult, especially without the help of a detailed computer simulation; thus, it was deemed prudent to analyze experimental heat transfer data and organize it in tabular form, as per Rosa et al.'s recommendation, for later reference and future research. On that note, regions of predominance of slip/roughness, conjugate heat transfer, and neither (balance/Hausen accuracy) were established in terms of Reynolds numbers and heat flux values and tabularized in Section 4.3.1 and 4.3.2 of this thesis. Although the present work was an experimental study, as opposed to numerical/simulation, a brief thermal simulation using the Mechanics subprogram of ProEngineer was carried out to aid in the understanding of the conjugate heat transfer effects present throughout the relevant experimentation. In short, the simulation analysis had proven by deduction, from the trends of discrepancies between experimentally obtained and simulation obtained microchannel heated-surface

temperatures, the claim made in Section 4.3 that the conjugate heat transfer effects present throughout the relevant experimentation were indeed 3-dimensional and not simply 1 or 2-dimensional (axial conduction).

To reiterate, the prototype MC-TEPG could ideally provide a net power output of up to 0.27 W—a modest value, which was enough to accomplish the general goal of this project. However at this early stage of its development, the relevant MC-TEPG cannot provide significant enough power to be applicable to actual military aircraft. For example, long-range bomber aircraft such as the B-52 require a minimum steady power supply on the order of 3 MW—an astronomically large amount relative to the 0.27-W capability of the MC-TEPG. Although the MC-TEPG cannot yet make any significant contribution to the main power supply of large military aircraft, it could find some secondary applicability, in that, it may be able to generate (and store in a small battery) a small amount of back-up power for emergency systems such as pilot seat ejection and flare launch. It is reasonable to believe that with the replacement of the convenient, inexpensive TEC1-12708 cooling thermoelectric modules with more appropriate and sophisticated thermoelectric power generation modules, reworking the microchannel heat exchanger design, and putting forth several more years of preferable well-funded research on the pertinent waste heat recovery concept, the MC-TEPG can become a renewable-energy alternative, or at least supplement, to battery packs of smaller military machines such as the Astroflight Inc.'s 450-W Sunrise no-man surveillance drone [45]. In the case of the Sunrise—a no-man drone powered

entirely by solar cells—a more advanced version of the present MC-TEPG prototype may be worth installing in order to generate enough emergency power to quickly and safely land the drone in hazardous situations such as prolonged lack of sunlight or sudden solar cell damage/failure during flight. Additionally, as the MC-TEPG would consume the waste heat from the motors inside the Sunrise, it would offer the continuous benefit of greatly lowering the heat signature of the drone, thus, contributing to stealth and ultimately mission accomplishment.

5.2: Recommendations for Future Work

Although the experimentation and results presented in this thesis have demonstrated a minimal feasibility of the relevant microchannel-thermoelectric power generator, this technology remains to be brought up to a standard of applicability to actual military machines. At present, there are multiple directions in which future research could advance. First, it is of the utmost importance to invest more time and resources to the separate research areas aimed at advancing one or more of the major components of the MC-TEPG, namely, thermoelectric modules (for power generation), microchannel heat exchanger, and nanofluids. Second, it is equally important for the engineering community to focus on the research of technologies that are required to support the basic functionality of the MC-TEPG such as micropumps. Third, it is pertinent to explore microchannel heat transfer via thorough and precise numerical simulations as they are typically far more convenient to conduct than painstaking experimental campaigns.

Since the overall MC-TEPG performance evaluated in this thesis was most severely limited by the inefficient TEC1-12708 thermoelectric material, it is very strongly recommended to develop new thermoelectric materials and geometries so as to achieve thermoelectric figure of merit ZT values above the current maximum of about 1. Some research in this respect is already underway. The use of nanostructures for thermoelectric applications was triggered by the conceptual studies in the early 1990s that identified the potential benefits of quantum confinement of electrons and phonons and phonon interface scattering [7]. $\text{Bi}_2\text{Te}_3/\text{Sb}_2\text{Te}_3$ superlattices were reported to have a ZT of about 2.5 around room temperature, the highest ZT to date, and $\text{PbSeTe}/\text{PbTe}$ quantum-dot superlattices exhibited a ZT of about 2.0 at elevated temperature (about 500K). Research is also being carried out to find a way to cost-effectively mass produce such nanostructure thermoelectric materials.

For optimal performance, microchannel heat exchanger design and construction must be carefully studied and improved upon so as to maximize heat transfer and minimize coolant pressure drop across the microchannel. As stated in Chapter 2, novel research to achieve the above was presented in the works of Davies et al. [31] and Chakraborty et al. [32]. These authors invoked very precise microfabrication technologies to manufacture microchannels that had superhydrophobic, ‘uniquely roughened’ wetted surfaces in order to encourage low-shear slip flow and greatly reduce pressure drop. Although, the experimentation pertaining to this thesis improvised to create a similar

microchannel; however, since microfabrication technology was not an available resource, the final product (microchannel) could not be designed very differently due to an inevitably low degree of manufacture control. Therefore, it is recommended to all microchannel researchers to invest in and apply sophisticated microfabrication technology to design and study microchannels along the same lines as the 2 above authors to further study the least understood scaling effects of slip combined with surface roughness.

After significant advancements in thermoelectric and microchannel research have been made, it may also be worthwhile to develop and study more advanced nanofluids such as the water-in-FC-72 nanofluid originally considered for the present work. The water-in-FC-72 nanofluid was experimentally shown to increase the thermal conductivity and heat capacity of base fluid FC-72 by up to 52% and 126%, respectively [5]. Argumentatively, the greatest technical challenge with nanofluid design remains to be the following: how to design for maximized thermal conductivity while minimizing the drop in specific heat and rise in viscosity as compared to respective base fluids. Therefore, the recommendation is, of course, to continue to work towards overcoming this technical challenge.

Since the practicality of the relevant MC-TEPG relies on it being compact and lightweight, components that must be installed along side of it, such as a pump, have to also be compact and lightweight while sufficiently supporting the MC-

TEPG function. Singhal et al. [46] have recently microfabricated and tested a micropump utilizing induction electrohydrodynamics (EHD) to be able to remove 1.44 W/cm^2 of heat at a pumping power input of 0.32 mW. This is a reasonable advancement in micropumping devices but further research on induction EHD and other similar pumping methods should remain a priority as demand for such high-performance, small-size technology is ever increasing.

In the present case as well as most others reviewed in this thesis, no single correlation or set thereof was able to provide accurate universal prediction of experimental Nusselt numbers. As per the present data analysis and collective information provided in Chapter 2, a major reason of correlation inaccuracy was that the basic boundary conditions (CWHF and CWT) that govern the applicability of these correlations were at least somewhat oversimplified as compare to the actual boundary conditions pertaining to the present experimentation. Therefore, in strong agreement with Rosa et al. [22], this thesis had concluded that to accurately understand heat transfer behavior in a microchannel heat exchanger with several parallel channels and multiple scaling effects in play, suitable numerical simulations are most likely the only alternatives to carefully designed experiments. In particular, it is recommended that precise numerical simulations with *suitable boundary conditions* be executed, instead of correlations, to predict microchannel heat exchanger performance.

The novel concept of waste heat recovery via a microchannel-thermoelectric power generator that uses nanofluids (or base fluids) as coolants is indeed an interesting one and shows much prospective promise to military as well as commercial sectors. While it is believed that the present work makes a reasonable initial contribution to the development and demonstration of feasibility of this technology, much future research is indubitably necessary for this new technology to rise to marketability and become a viable renewable energy alternative to non-renewable fuel-burning power suppliers. When pertinent research, especially in the area of thermoelectricity, advances far enough, it is believed that the microchannel-thermoelectric power generator will become instrumental to future power supply needs.

5.3: Professional Contributions Made by the Author

The author of this thesis has made a number of noteworthy professional contributions to NSWC-Carderock, UMCP and the global community of scientists and engineers. First, the author designed and constructed the abovementioned microchannel test rig to be a most reliable and precise apparatus on a very constrained budget as called for by ARPA-E's initiative of 'self-funded' research. This test rig bore a special double-loop flow cycle design in order to be able to accommodate a wide variety of fluids including nanofluids.

The second major contribution made by the author lies in the design of the microchannel heat exchanger used in the present experimentation. Specifically,

dissimilar to most microchannel researchers who design for smooth channels to minimize pressure drop, the present microchannel wetted surfaces were purposefully made rough (10%, relative to diameter) and hydrophobic to successfully reduce pressure drop up to 51% below the values predicted by conventional laminar theory—a sizable advancement in overcoming the major technical challenge of microchannel pressure drop reduction. Moreover, the present rough-and-hydrophobic microchannel design was manufactured *without requiring microfabrication technology* unlike the similar designs of Davies et al. [31] and Chakraborty et al. [32], which inspired it.

The final notable contribution made by this author can be found in the results and analyses this thesis offers to its audience. Specifically, the author has discussed the variation of the trends and magnitudes of the relevant pressure drop, heat transfer coefficient and MC-TEPG net power output parameters under varying test conditions in terms of the key scaling effects that come into play at the micro-scale. In fact, the well-organized tabular description of predominance regions of pertinent scaling effects of conjugate heat transfer, thermal entrance, roughness and slip flow is intended by the author to mitigate the ambiguity due to data scattering existing in the engineering community since the dawn of microchannel research. Finally, the decision of the author to supplement this experimental study with a basic computer simulation aided in deductively proving that the conjugate heat transfer effects present in this project, and likely in most previously documented studies, were *3-dimensional* and had to be accounted for as such.

References

- [1] Borowitz, S. *Farewell Fossil Fuels: Reviewing America's Energy Policy*. New York: Plenum Press, 1999.
- [2] Rodgers, D. Energy efficient and renewable energy technologies for a low carbon future. Lecture. Van Munching Hall. University of Maryland, College Park, Maryland. 25 Mar. 2010.
- [3] Umstattd, R. J. Future energy efficiency improvements within the US department of defense: Incentives and barriers. *Energy Policy*. 37 (2009) 2870-2880.
- [4] Tran, T. Request for B&P Funds: Thermoelectric energy conversion (TEC) technology for naval applications. Memo to NSWC Carderock Division, West Bethesda, MD. Jan. 2006.
- [5] Yang, B., Professor of Mechanical Engineering, University of Maryland-College Park, Tran, T., Mechanical Engineer, NSWC Carderock Division. Personal Interview. 22 Jun. 2007.
- [6] Yang, B. Collaborative research: characterization of thermal transport in nanofluids. Memo to Dr. Thanh Tran, Systems & Materials For Power & Protection Systems Branch, Memo to NSWC Carderock Division, West Bethesda, MD. Mar. 2007.
- [7] Yang, B., Ahuja, H., Tran, T. N. Thermoelectric technology assessment: application to air conditioning and refrigeration. *HVAC&R Research*. 14 (2008) 635-653.
- [8] McCluskey, F. P. Cooling methods in electronic packaging. Lecture. Glenn L. Martin Hall. University of Maryland, College Park, Maryland. 10 Nov. 2007.
- [9] Da Rosa, A. V. *Fundamentals of Renewable Energy Processes*. Burlington: Elsevier Academic Press, 2005.
- [10] Bulusu, A., Walker, D. G. Review of electronic transport models for thermoelectric materials. *Superlattices and Microstructures*. 44 (2008) 1-36.
- [11] Chen, M., Lund, H., Rosendahl, L. A., Condra, T. J. Energy efficiency analysis and impact evaluation of the application of thermoelectric power cycle to today's CHP systems. *Applied Energy*. 87 (2010) 1231-1238.
- [12] Maneewan, S., Hirunlabh, J., Khedari, J., Zeghamati, B., Teekasap, S. Heat gain reduction by means of thermoelectric roof solar collector. *Solar Energy*. 78 (2005) 495-503.
- [13] Das, S. K., Choi, S. U. S., Patel, H. E. Heat transfer in nanofluids—a review. *Heat Transfer Engineering*. 27 (2006) 3-19.
- [14] Eastman, J. A., Phillpot, S. R., Choi, S. U. S., Keblinski, P. Thermal transport in nanofluids. *Annu. Rev. Mater. Res.* 34 (2004) 219-246.
- [15] Yoo, D., Hong, K. S., Yang, H. Study of thermal conductivity of nanofluids for the application of heat transfer fluids. *Thermochimica Acta*. 455 (2007) 66-69.
- [16] Wen, D., Ding, Y. Experimental investigation into convective heat transfer of nanofluids at the entrance region under laminar flow conditions. *International Journal of Heat and Mass Transfer*. 47 (2004) 5181-5188.

- [17] Maiga, S. B., Palm, S. J., Nguyen, C. T., Roy, G., Galanis, N. Heat Transfer enhancement by using nanofluids in forced convection flows. *International Journal of Heat and Fluid Flow*. 26 (2005) 530-546.
- [18] Yang, Y., Zhang, Z. G., Grulke, E. A., Anderson, W. B., Wu, G. Heat transfer properties of nanoparticle-in-fluid dispersions (nanofluids) in laminar flow. *International Journal of Heat and Mass Transfer*. 48 (2005) 1107-1116.
- [19] Heris, S. Z., Esfahany, M. N., Etemad, S. G. Experimental investigation of convective heat transfer of Al_2O_3 /water nanofluid in circular tube. *International Journal of Heat and Fluid Flow*. 28 (2007) 203-210.
- [20] Tuckerman, D. B., Pease, R. F. W. High-performance heat sinking for VLSI. *IEEE Electron Device Letters*. 2 (1981) 126-129.
- [21] Sobhan, C. B., Garimella, S. V. A comparative analysis of studies on heat transfer and fluid flow in microchannels. *Microscale Thermophysical Engineering*. 5 (2001) 293-311.
- [22] Rosa, P., Karayiannis, T. G., Collins, M. W. Single-phase heat transfer in microchannels: The importance of scaling effects. *Applied Thermal Engineering*. 29 (2009) 3447-3468.
- [23] Gamrat, G., Favre-Marinet, M., Asendrych, D. Conduction and entrance effects on laminar liquid flow and heat transfer in rectangular microchannels. *International Journal of Heat and Mass Transfer*. 48 (2005) 2943-2954.
- [24] Tso, C. P., Mahulikar, S. P. The use of the Brinkman number for single phase forced convective heat transfer in microchannels. *International Journal of Heat and Mass Transfer*. 41 (1998) 1759-1769.
- [25] Tso, C. P., Mahulikar, S. P. The role of the Brinkman number in analysing flow transitions in microchannels. *International Journal of Heat and Mass Transfer*. 42 (1999) 1813-1833.
- [26] Tso, C. P., Mahulikar, S. P. Experimental verification of the role of Brinkman number in microchannels using local parameters. *International Journal of Heat and Mass Transfer*. 43 (2000) 1837-1849.
- [27] Celata, G. P. Single- and two-phase flow heat transfer in micropipes. 5th *European Thermal-Sciences Conference*, 2008, The Netherlands. Rome, Italy: ENEA, Energy Department, Institute of Thermal-Fluid Dynamics.
- [28] Baviere, R., Favre-Marinet, M., Le Person, S. Bias effects on heat transfer measurements in microchannel flows. *International Journal of Heat and Mass Transfer*. 49 (2006) 3325-3337.
- [29] Celata, G. P., Cumo, M., Marconi, V., McPhail, S. J., Zummo, G. Microtube liquid single-phase heat transfer in laminar flow. *International Journal of Heat and Mass Transfer*. 49 (2006) 3538-3546.
- [30] El-Genk, M. S., Yang, I. Friction numbers and viscous dissipation heating for laminar flows of water in microtubes. *Journal of Heat Transfer*. 130 (2008) 082405 (13pp).
- [31] Davies, J., Maynes, D., Webb, B. W., Woolford, B. Laminar flow in a microchannel with superhydrophobic walls exhibiting transverse ribs. *Physics of Fluids*. 18 (2006) 087110 (12pp).

- [32] Chakraborty, S., Anand, K. D. Implications of hydrophobic interactions and consequent apparent slip phenomenon on the entrance region transport of liquids through microchannels. *Physics of Fluids*. 20 (2008) 043602 (9pp).
- [33] Lee, J., Mudawar, I. Assessment of the effectiveness of nanofluids for single-phase and two-phase heat transfer in micro-channels. *International Journal of Heat and Mass Transfer*. 50 (2007) 452-463.
- [34] Wu, X., Wu, H., Cheng, P. Pressure drop and heat transfer of Al₂O₃-H₂O nanofluids through silicon microchannels. *Journal of Micromechanics and Microengineering*. 19 (2009) 105020 (11pp).
- [35] Bergman, T. L. Analysis of heat transfer enhancement in minichannel heat sinks with turbulent flow using H₂O-Al₂O₃ nanofluids. *Journal of Electronic Packaging*. 131 (2009) 021008 (5pp).
- [36] Jung, J., Oh, H., Kwak, H. Forced convective heat transfer of nanofluids in microchannels. *International Journal of Heat and Mass Transfer*. 52 (2009) 466-472.
- [37] http://www.epa.gov/nrmrl/wswrd/cr/corr_res_copper.html
- [38] <http://www.keymetals.com/Article14.htm>
- [39] Moores, K. A., Joshi, Y. K., Schiroky, G. H. Thermal characterization of a liquid cooled AlSiC base plate with integral pin fins. *IEEE Transactions on Components and Packaging Technologies*. 24 (2001) 213-219.
- [40] http://www.hebeiltd.com.cn/peltier_datasheet/TEC1-12708.pdf
- [41] http://mico.com/heater_config/model_03.aspx?PN=HM6800
- [42] <http://customthermoelectric.com/TECmounting.html>
- [43] Tang, G. H., Li, Z., He, Y. L., Tao, W. Q. Experimental study of compressibility, roughness and rarefaction influences on microchannel flow. *International Journal of Heat and Mass Transfer*. 50 (2007) 2282-2295.
- [44] http://en.wikipedia.org/wiki/Haland_equation#Haland_equation
- [45] <http://en.wikipedia.org/wiki/AstroFlight>
- [46] Singhal, V., Garimella, S. V. Induction electrohydrodynamics micropump for high heat flux cooling. *Sensors and Actuators A*. 134 (2007) 650-659.

